12-2011

Influence of Aging and Severe Plastic Deformation on the Shape Memory Behavior of Ti-50.6at%Ni

William Shirley
Clemson University, willias@clemson.edu

INFLUENCE OF AGING AND SEVERE PLASTIC DEFRORMATION ON THE SHAPE MEMORY BEHAVIOR OF Ti-50.6at%Ni

---

A Thesis
Presented to
the Graduate School of
Clemson University

In Partial Fulfillment
of the Requirements for the Degree
Master of Science
Materials Science and Engineering

---

by
William R. Shirley Jr.
December 2011

Accepted by:
Dr. Henry J. Rack, Committee Chair
Dr. Eric C. Skaar
Dr. Jian Luo

ABSTRACT

Martensitic phase transformations were investigated for Ti -50.6 at % Ni processed via severe plastic deformation (SPD) and subsequent aging for temperatures between 400 and 550C and times ranging from 1hr to 100hrs. Phase transformations of the SPD material were compared to material processed via solution treated at 800C and 850C for 1hr. Transformations were investigated with differential scanning calorimetry (DSC) and confirmed by X-ray diffraction (XRD) with optical microscopy being used to determine grain size. Solution treated samples displayed a single (1-1) B2↔B19' transformation prior to and upon initial aging, i.e. 400C/1h, 450C/1/10h. Intermediate aging conditions, 450C/100h; 500C/1/10/100h; and 550C/1h, resulted in multiple B2↔B19' transformations (2-2). Aging at 400C/10/100h, induced the R phase and 3-2 transformation behavior. Intensive aging caused the solution treated material and the SPD material to revert to a single (1-1) B19'↔B2 transformation. A 2-1 transformation was exhibited by the bulk of the SPD samples, i.e. unaged SPD, 400C and 450C at 1/10/100h, 500C 1/10h, 550C 100h. XRD of SPD material indicated the presence of metastable Ni_4Ti_3 precipitates prior to aging, and equilibrium Ni3Ti precipitates after aging for 500C/100h. Multiple peaks in the solution treated samples result from composition heterogeneities. 3-2 behavior is the result critical microstrains inducing the R phase. 2-1 behavior of the SPD material results from a homogenous microstructure and macrostrains which induce the R phase. Aging the SPD material causes recovery, suppressing the R phase transformation and increasing the Ms temperature, eventually resulting in a 1-1 transformation.

ACKNOWLEDGEMENTS

I would like to express thanks to my advisor, Dr. H.J. Rack, for his guidance during the course of this study without which, none of this would be possible.

I am also thankful for the TEM images provided to me by Dr. Valiev.

During the course of this study I also hope that I was not too much of a burden on Herbert Boeckels, as I relied greatly on his guidance, especially early on.

Throughout of this work, David White's expertise proved invaluable in troubleshooting and repairing the lab equipment needed for this study, and for that I am truly grateful.

I would like to express the deepest appreciation to Dr. Jaeil "Jae" Jung for his friendship during my time here at Clemson. Jae's insights into life and faith have helped me to keep this work within the proper context of my life.

Lastly, I would like to thank my family whose love and support has always acted as a haven for me during even the most uncertain times in my life. I carry with me and will always carry with me their influences and love, and for that I am truly blessed.

TABLE OF CONTENTS

Table of Contents (Continued) Page

LIST OF TABLES

LIST OF FIGURES

List of Figures (Continued)

Figure Page

List of Figures (Continued)

Figure Page

List of Figures (Continued)

List of Figures (Continued)

CHAPTER ONE

INTRODUCTION

Nitinol, TiNi, because of its excellent strength, good ductility, and high recoverable strains, which in some cases can be as high as 10%, is a widely used shape memory alloy [1-3]. However, these large recoverable strains require either aging or cold working processes [4, 5]. From a design perspective, control of TiNi's shape memory functionality requires control of the martensitic phase transformations found in the system either through composition or precipitation [6-8]. Recent interest has focused on enhancing the mechanical, corrosion, and shape memory properties of TiNi through grain refinement. Processes involving severe plastic deformation(SPD) coupled with aging have proven fruitful in this regard, although use of these procedures does result in changes in the TiNi martensitic behavior [9-16].

The aim of this research is to examine the martensitic transformation behavior exhibited by Ti-50.6at%Ni when subjected to SPD, namely equal angular extrusion/pressing (ECAE/ECAP). Further effort has also considered the influence of subsequent aging treatments on the ECAP condition, as characterized by their shape memory properties. For comparison, the martensitic behavior of solution treated Ti-50.6% Ni exposed to the same aging conditions were also examined. Notably, SPD has the potential to greatly alter the martensitic transformations seen in TiNi given the high dislocations densities produced and the known tendency for increasing dislocation densities to suppress the B19' martensitic phase while promoting the appearance of the R phase [9,10,16]. Aging alone also has the potential to alter the martensitic transformations again tending to enhance R phase formation for materials not processed through SPD [17-20]. However nothing to date has examined the effects of ECAP and aging combined.

The martensitic transformation behavior resulting from aging in the ECAP Ti-50.6at% Ni and the solution treated case was examined using anisothermal differential scanning calorimetry (DSC). X-ray diffraction (XRD) was performed to confirm the presence phases suggested by the DSC runs. Finally optical and transmission electron microscopy was performed to examine the grain size refinement due to the ECAP process and also the change in grain structure upon aging.

CHAPTER ONE REFERENCES

[1]M.F-X.Wagner, W.Windl, "Elastic Anisotropy of Ni_4Ti_3 from First Principles", Scripta Mater. ,Vol. 60, 2009: 207-210.

[2]K.Gall, H.Sehitoglu, Y.I.Chumlyakov, I.V. Kireeva, "Tension-compression Asymmetry of the Stress-strain Response in Aged Single Crystal and Polycrystalline NiTi", Acta Mater., Vol. 47, 1999: 1203-1217.

[3]F.X.Gil-Mur, D.Rodriguez, J.A.Planell, "Grain Growth of NiTi Alloy and Its Influence on the Martensitic Transformation Temperatures and Thermodynamic Parameters", Titanium '95: Science and Technology, Birminham, UK, eds. P.A. Blenkinsop, W.J. Evans, M. Flower, Institute of Materials, Vol. 3, 1996: 2399-2406.

[4]C.P.Frick, A.M.Ortega, J.Tyber, A.El.M. Maksound, H.J.Maier, Y.Liu, K.Gall, "Thermal Processing of Polycrystalline NiTi Shape Memory Alloys", Mat. Sci. Eng. A ,Vol. 405, 2005: 34-49.

[5]A.M. Ortega, J. Tyber, C.P. Frick, K. Gall, H.J. Maier, "Cast NiTi Shape-Memory Alloys", Adv. Eng. Mater. Vol. 7, 2005: 492-507.

[6]J.Khalil-Allafi, X.Ren, G.Eggeler, "The Mechanism of Multistage Martensitic Transformations in Aged Ni-Rich NiTi Shape Memory Alloys", Acta Mater. ,Vol. 50,2002: 793-803.

[7] A.Dlouhy, J.Kahalil-Allafi, G.Eggeler, "On the Determination of the Volume Fraction of Ni_4Ti_3 Precipitates in Binary Ni-Rich NiTi Shape Memory Alloys", Z. Metallkd., Vol. 95 (6), 2004: 518-524.

[8] C.P.Frick, A.M.Ortega, J.Tyber, K.Gall, H.J.Maier, "Multiscale Structure and Properties of Cast and Deformation Processed Polycrystalline NiTi Shape-memory Alloys", Metall. Mat. Trans. A , Vol. 35A ,2004: 2013-2025.

[9] T.Waitz, V.Kazykhanov, H.P.Karnthaler, "Martensitic Phase Transformations in Nanocrystalline NiTi Studied by TEM", Acta Mater. Vol. 52, 2004: 137-147.

[10] H.Nakayama, K.Tsuchiya, M.Umemoto, "Crystal Refinement and Amorphisation by Cold Rolling in TiNi Shape Memory Alloys", Scripta Mater. Vol. 44 , 2001: 1781-1785.

[11] C.Y.Xie, Z.G.Fan, Z.H.Li, G.Q.Xiang, X.H.Cheng, "Effects of High Temperature ECAE Process on Microstructures and Martensitic Transformation of TiNi Shape Memory Alloy", Mat. Sci. Forum, Vol. 503-504, 2006: 1013-1018.

[12] V.G. Pushin, R.Z. Valiev, Y.T. Zhu, D.V. Gunderov, N.I. Klourov, T.E. Kuntsevich, A.N. Uksusnikov, L.I. Yurchenko, "Effect of Severe Plastic Deformation on the Behavior of Ti-Ni Shape Memory Alloys", Mater. Trans., Vol. 47, 2006: 694-697.

[13]E. Prokofiev, D. Gunderov, A. Lukyanov, V. Pushin, R. Valiev, "Mechanical Behavior and Stress-Induced Martensitic Transformation in Nanocrystalline $Ti_{49.4}Ni_{50.6}$ Alloy", Mater. Sci. Forum, Vol. 584-586 2008: 470-474.

[14]R. Valiev, D. Gunderov, E. Prokofiev, V. Pushin, Y. Zhu, "Nanostructuring of TiNi Alloy by SPD Processing for Advanced Properties", Mater. Trans., Vol. 49, 2008: 97-101.

[15] T.Waitz, H.Karnthaler, T.Antretter, F.D.Fischer, "Martensitic Phase Transformations of Bulk Nanocrystalline NiTi Alloys", Solid-to-Solid Phase Transformations in Inorg. Mat., Vol. 2 ,2005: 885-898.

[16] V.Demers, V.Brailovski, S.Prokoshkin, K.Inaekyan, E.Bastarash, I.Khmelevskaya, S.Dobatkin, "Functional Properties of Nanostructured Ti-50.0 at% Ni Alloys", J. ASTM Int., Vol. 3 (6), 2006: 34-44.

[17] L.Bailaillard, J.E.Bidaux, R.Gotthardt, "Interaction between Microstructure and Multiple-step Transformation in Binary NiTi Alloys Using In-situ Transmission Electron Microscopy Observations", Philos Mag. A, Vol. 78 (2), 1998: 327-344.

[18] G.B.Stachowiak, P.G.McCormick, "Shape Memory Behaviour Associated with the R and Martensitic Transformations in a NiTi Alloy", Acta Metall. Vol.36 (2) 1988: 291-297.

[19] M.C.Carroll, CSomsen, G.Eggeler, "Multiple-step Martensitic Transformations in Ni-rich NiTi Shape Memory Alloys", Scripta Mater., Vol. 50 ,2004: 187-192.

[20] M.Peltonen, T.Lindroos, M.Kallio, "Effect of Ageing on Transformation Kinetics and Internal Friction on Ni-rich Ni-Ti Alloys", J Alloy Comp., Vol. 460, 2008: 237-245.

CHAPTER TWO

BACKGROUND

Ti-Ni Phase Diagram

As pictured in Figure 1, TiNi exists as an intermetallic compound in the TiNi phase system congruently melting at 1310C. At 1090C TiNi also exhibits an order-disorder transformation, with the ordered body centered cubic, B2 phase occurring below 1090C and the disordered body centered cubic phase occurring above. The TiNi phase field is surrounded on both sides by two phase regions. On the Ti-rich side this region consists of TiNi + Ti_2Ni , while the Ni-rich side contains a mixture of TiNi and Ni_3Ti [1].

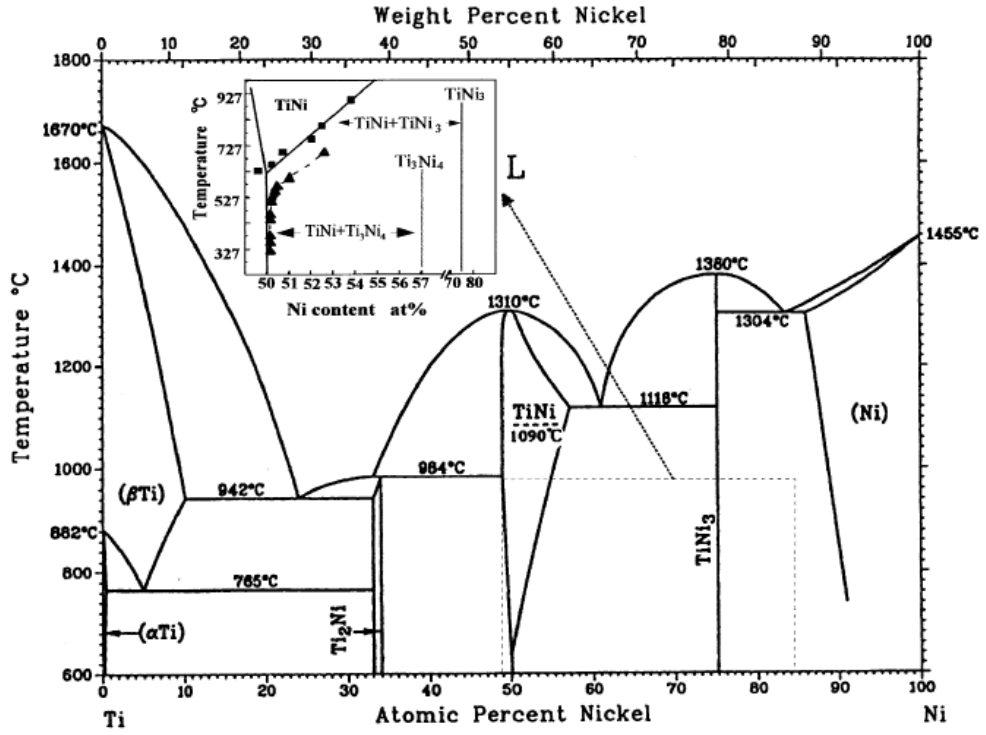

Figure 1: Ti-Ni phase diagram [1].

An important feature of Ni rich TiNi is that the TiNi phase field shows a marked decrease in solubility for nickel at lower temperatures, thereby enabling the creation of a Ni-rich

supersaturated solid solution for compositions greater than 50at% Ni when quenched from elevated temperatures. Subsequent reheating to temperatures below the single phase region results in formation of Ni-rich precipitates will form.

Shape Memory Effect

The shape memory effect (SME) describes a variety of responses all of which relate to the spontaneous recovery of shape or strain. Underlying all these effects are specific characteristics which are unique to a set of alloys exhibiting the SME known as shape memory alloys. The primary shape memory characteristic is that this effect requires the operation of a reversible, diffusionless martensitic transformation. Of the shape memory alloys, TiNi has proven to be the most practical given its high ductility and large recoverable strains with can be on the order of 10% given the proper processing history [2-4]. These prescribed treatments limit the number of twin variants formed during the martensitic transformation [3,5]. Due to the symmetry of the austenitic phase the martensitic variants will convert to only one variant of austenite upon reverse transformation [5].

Furthermore, twinning should be the primary strain relief mechanism associated with the martensitic transformation [5, 6]. Indeed twinning is crystalographically entirely reversible, this reversibility being necessary for high strain recovery. In contrast crystallographic slip is non-reversible and as such TiNi is often put though a variety of thermo-mechanical treatments designed to promote twinning and suppressing slip, e.g., cold working and aging [5-7].

Generally shape memory alloys are ordered and as such they are typically intermetallic compounds [5, 8]. Figure 2 illustrates the crystal structures of ordered and disordered equiatomic TiNi, respectively. Ordering promotes twin formation, ordered alloys having a higher critical resolved shear stress for slip vis a vis twinning since all dislocation movement

must be paired to maintain local order, that is, the first dislocation movement destroys the ordered structure while the second dislocation restores ordering.

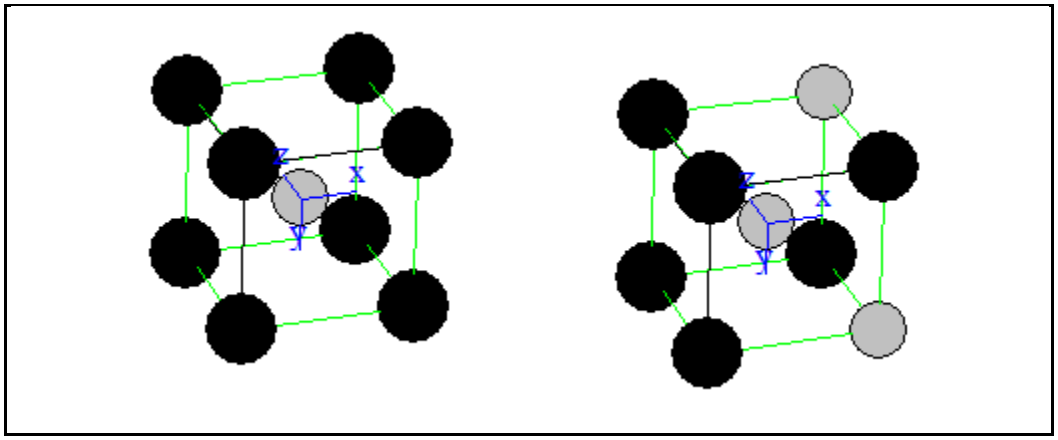

a) b)

Figure 2: Ordered vs. disordered TiNi with Ni atoms represented by gray spheres and black spheres represented Ti atoms: a) Ordered TiNi; b) Disordered TiNi.

Severe Plastic Deformation

Severe plastic deformation (SPD) is intended to result in the formation of a fine grained microstructure having a grain size less than 500nm through a variety of processes which impart large strain to the material. These SPD processes include cold rolling, high pressure torsion, and equal channel angular pressing (ECAP) [9-11]. By their nature, such processes result in a significant increase in subgrain and grain boundary surface area per unit volume as well as an increased intragranular dislocation density [9-12]. As a result of the change in microstructure, a number of properties can be enhanced, including corrosion resistance and high cycle fatigue, although the main impetus for grain refinement is the improvement of strength [9-11].

The mechanism by which grain refinement occurs is largely mechanical as the ECAP process normally takes place at temperatures far below the recrystallization temperatures. Essentially with increasing strain, subgrain boundaries are created, increasing strain leading to

boundary rotation and reorientation until they become indistinguishable from ordinary grain boundaries[12].

ECAP utilizes a die split at some angle (Φ) which usually varies between 90 and 120 degrees. Passage of a material through this die results in intense localized shear deformation, the work piece ultimately emerging from the die with no change in cross sectional area, a distinct advantage of the ECAP process. There are several key processing parameters and considerations involved in the ECAP process. For instance, given the large strains involved, the ECAP process is generally conducted at temperatures selected to have enhanced ductility in order to prevent cracking. The angle between the channels (φ) is also a significant factor in controlling the strain delivered to the material, with higher strains being delivered as the angle approaches 90 degrees. Below 90 degrees, it becomes very difficult to pass the material and there is the tendency for the appearance of what is termed "dead material", which refers to the material that shows no enhancement of properties through each pass [12-14]. The corners where the die is split are also typically rounded to aid in passage of the material with the strain accumulated for each pass being given by [15],

$$\varepsilon_n = \frac{2\,n\cot(\Phi)}{\sqrt{3}} \qquad (1)$$

where ε_n is the strain accumulated, Φ is the angle between the channels of the die and n is the number of passes.

Beyond die geometry and temperature, it is also possible to alter both the texture and the microstructure of the sample based on the processing route, this referring to how the sample is rotated from pass to pass. Variations among processing routes arise due to the fact that the shear plane induced by the die is constant and therefore the only way to alter the location of this plane and the area affected within the material is to change the orientation of the sample. The four

most common processing routes are termed A, B_A, B_C, and C and are represented in Figure 3 [14].

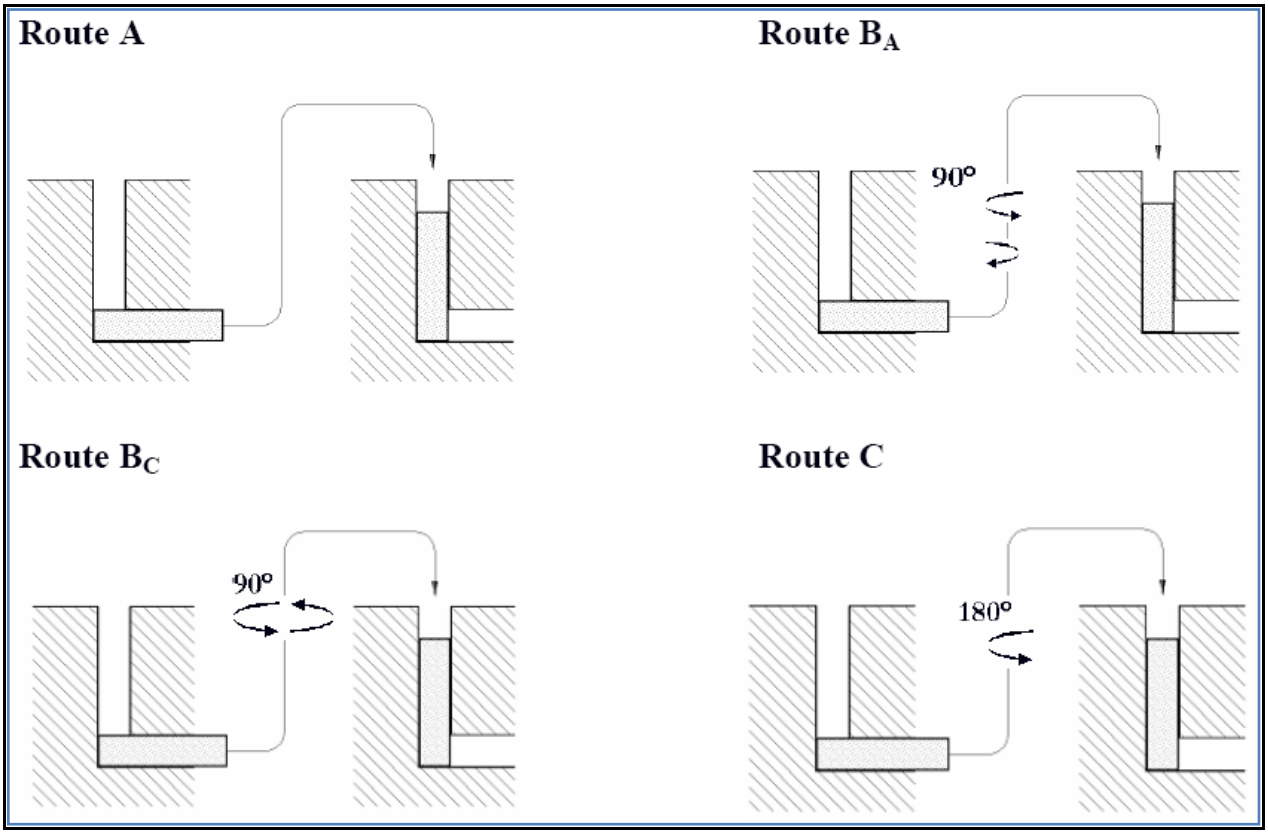

Figure 3: Common processing routes in ECAP [14].

In route A, there is no rotation with each successive pass and the sample is pressed through in the same orientation as in the previous pass. Utilizing route B_C, the sample is rotated by 90 degrees about its cross section after each pass. Route B_A is similar to route B_C, that is, after the first pass the sample is rotated by +90 degrees and repressed. Then the sample is rotated by -90 degrees and pressed again. Route C involves rotating the sample by 180 degrees before repressing [14].

Martensitic Phase Transformations

As alluded to earlier, mechanistically the shape memory effect centers on reversible martensitic transformations and therefore from a design perspective, considerations relating to martensitic transformations are of prime concern. In the simplest terms, a martensitic transformation is a diffusionless shear transformation whereby the atoms of a high temperature parent phase (austenitic phase) are displaced by locations smaller than lattice parameters to yield a phase with a distorted crystal structure of the parent phase [17].

Conversion of the parent phase to the martensitic phase occurs through crystallographic operations involving rotations and dilations, with what is known as an invariant plane existing between the parent phase and the martensitic phase. This invariant plane is fully coherent between the parent and martensitic phases and remains constant through the conversion in that it does not undergo any rotations or distortions. Through the conversion to martensite, there is a build-up of strains, which exist both normal and parallel to the invariant plane and are termed the dilation strain and the shear strain, respectively [16,17]. Regardless of the orientation, both the strains must be accommodated either through the formation of dislocations or twinning (Figure 4).

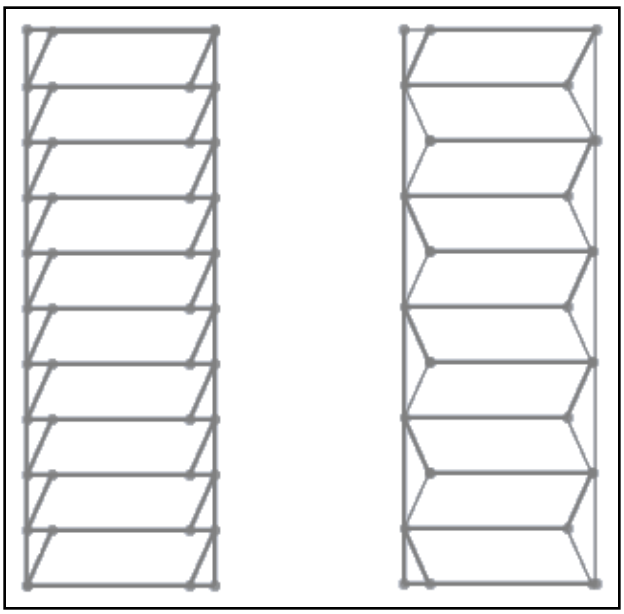

Figure 4: Modes of accommodating martensite: a) slip; b)twinning.

Beyond crystallographic concerns, the overall driving force for the formation of martensite is undercooling and the corresponding reduction in bulk free energy of the system. In considering reductions in free energy of the system, there is a temperature defined as To such that the free energies of the martensitic phase and the austenitic phase are equal and should therefore exist in equilibrium at this temperature. However this is seldom the case as other factors must be considered in addition to bulk free energy which cause a deviation from To. In describing deviations from To, Ms and Mf are defined as the temperature where the martensitic phase transformation begins and ends, respectively. As and Af refer to the respective temperatures where the austenitic phase transformation starts and finishes. As mentioned previously there is a great deal of strain associated with the formation of martensite and this results in a strain energy which influences the temperatures at which the martensitic phase occurs. Additionally the interfacial energy resulting from the formation of a new interface will also cause deviations from To [17].

Although the exact mechanism for martensite nucleation remain controversial most investigators believe that prior to transformation, there exist martensitic embryos in the parent phase which are ellipsoidal in shape and consist of a nest of dislocations. Often these dislocation nests are associated with a tilt boundary and it is the dispersal of the dislocations into the surrounding crystal structure with provides the crystallographic means by which a martensitic transformation can occur. Regardless of the exact mechanism, it is widely held that the nucleation of martensite is heterogeneous in nature as experimental evidence shows that the timescale associated with the martensitic transformation is far too fast to have occurred homogenously. The martensitic phase has also been shown to occur in sparsely separated regions, which again suggests that the transformation is heterogeneous [17-19].

Non-thermoelastic Martensitic Transformations

Non-thermoelastic martensitic transformations are not crystallographically reversible in that the conversion of the martensitic phase back to the parent phase occurs through a nucleation of the parent phase within the martensitic phase and this resulting parent phase possesses a new orientation completely independent to the orientation of the original parent phase seen prior to the very first conversion to martensite [5].

As mentioned previously, deviations from To are common to all martensitic transformations, however for the non-thermoelastic case these deviations are especially significant, to the point that a large hysteresis between the As and Ms temperatures occurs. Essentially these large deviations can be rationalized from the idea that there is a resistance in the forward and reverse transformations due to strain energy and interfacial energy to the point that Ms will lie below To and As will lie above To (Figure 5) [17].

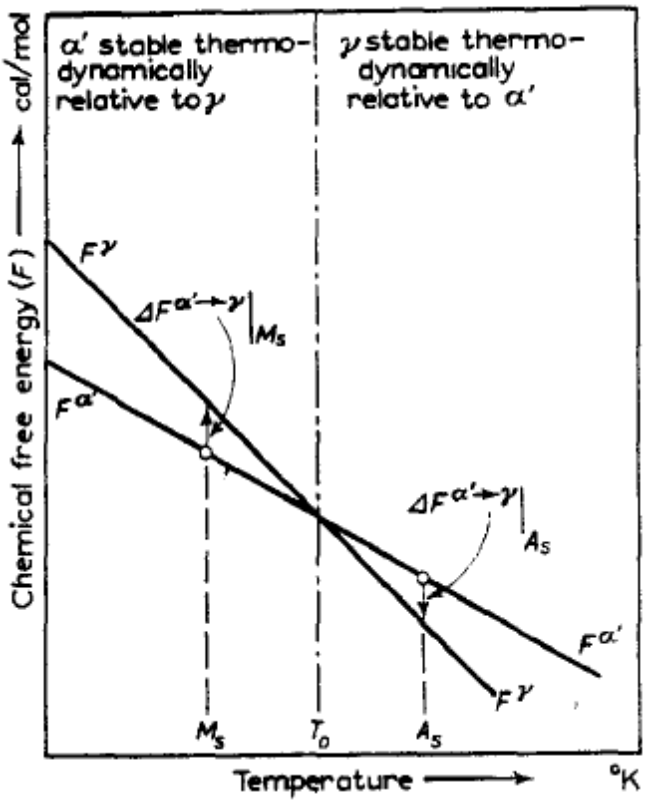

Figure 5: Free energy curves showing Ms, As and To [17].

Thermoelastic Martensitic Transformations

In thermoelastic transformations, in stark contrast to non-thermoelastic transformations, the conversion of the martensitic phase back to the parent phase does not occur by a nucleation mechanism and instead occurs by a mechanism involving interfacial motion, whereby the motion of the interface is balanced by an elastic backstress and further cooling or heating is required in order to move the interface as the crystal structure is converted. As a token of this mechanism, thermoelastic transformations are truly crystalographically reversible that is the martensitic phase will convert back to the original variant of the parent phase on heating [5].

Deviations from To in thermoelastic martensite are also less significant than in non-thermoelastic case, resulting in greatly reduced hysteresis as seen for the Au-Cd (thermoelastic) vs the Fe-Ni (non-thermoelastic) systems of Figure 6. [5] Moreover, the presence of the

backstress in the reversion back to the parent phase can cause the As temperature to occur below the To temperature and possibly even below the Ms temperature [5,17].

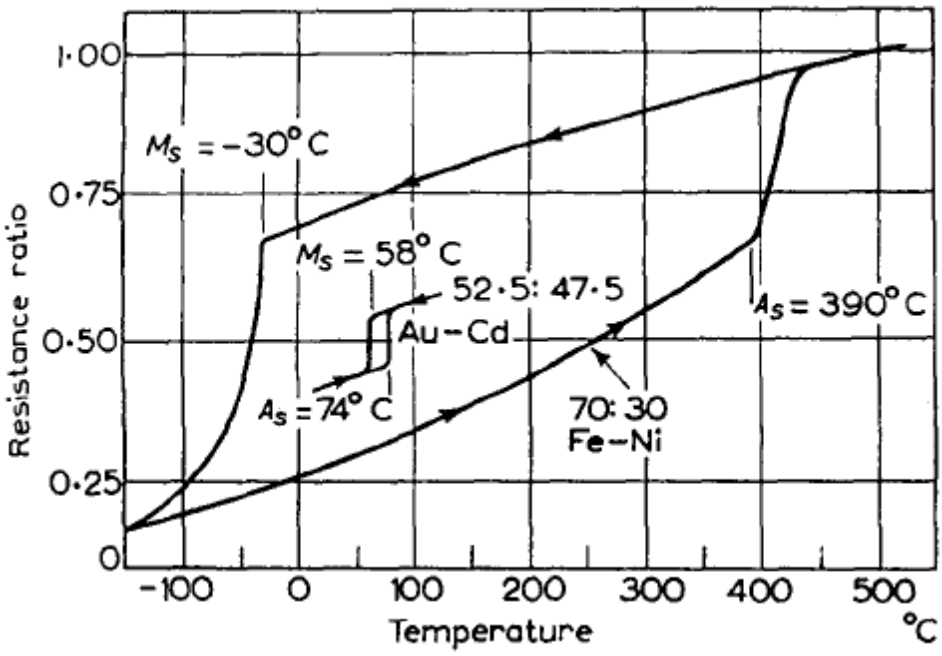

Figure 6: Relative difference in hysteresis displayed by a thermoelastic transformation (Au-Cd) and a non-thermoelastic transformation (Fe-Ni) [5]

TiNi Martensitic and Austenitic Phases

The martensitic transformations exhibited by TiNi tend to be more complex when compared to other systems as there are a variety of martensitic phases which can occur depending on the composition and processing history of the alloy. There is however only one austentic phase (ignoring the disordered case at high temperatures), which has an ordered cubic structure or B2. The lattice parameter of the austentic phase is 3.01 angstroms with the atomic position of the Ti atoms being (0,0,0) and the atomic positions of the Ni atoms (1/2,1/2,1/2) [1], Figure 7. Reductions in Ni content show an decrease in the lattice parameter of the B2 phase owing to the smaller atomic radius of Ti compared to Ni [20].

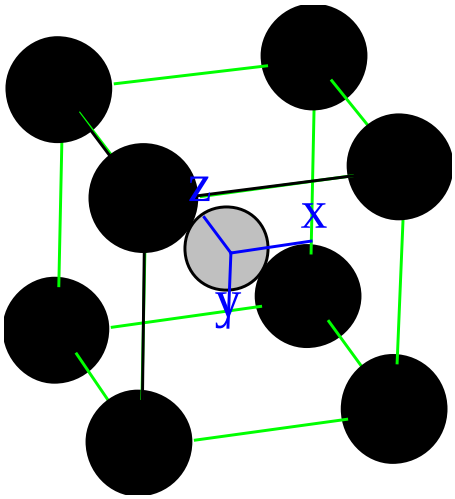

Figure 7: The unit cell of the austentic phase in TiNi shown with an expanded lattice. Gray spheres represent Ni atoms and black spheres represent Ti. Image generated using Carine version 3.1.

In turn the lowest temperature martensitic phase observed in TiNi is denoted as the B19' phase (Figure 8). This phase has a monoclinic structure with the following lattice parameters: a=2.833; b=4.117; c=4.623, the beta angle being 96.8 degrees. Given the monoclinic structure, the atomic positions, though ordered like the austentic phase, are more complex. The atomic position of the Ti atoms in Cartesian coordinates are (0,0,0) and (0.1648,1/2,0.5672), and the atomic position of the Ni atoms are (0.6196,0,0.4588) and (0.5452,1/2,0.1084) [1]. The lattice parameters of the B19' phase are a function of the Ni content with the a and b axies increasing with decreasing Ni content, while the c axis and the beta angle of the monoclinic cell decreasing with reductions in Ni content [20].

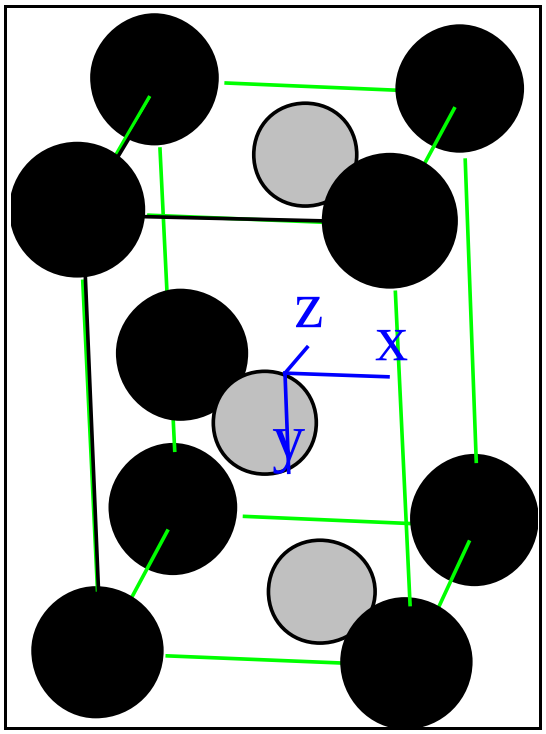

Figure 8: The unit cell of the B19' phase in TiNi with an expanded lattice to show the atomic positions. Ti atoms are black and Ni atoms are gray. Image created using Carine version 3.1.

There is also an intermediate martensitic phase known as the R phase (Figure 9). This phase is rhombohedral in structure with a lattice parameter of 6.02 and an angle of 90.7. Again this phase is ordered with the atomic positions in Cartesian coordinates for the Ti atoms is and Ni atoms being given in Table 1 [1]. To the author's knowledge there has not been any systematic study to address changes to the lattice parameters of the R phase with Ni content.

Table 1: Atomic Positions of Ti and Ni in R phase Given in Cartesian Coordinates [1].

Atom	Position
Ti	(0,0,0)
Ti	(1/3,2/3,0.083)
Ti	(1/3,2/3,1/3)
Ti	(0.335,0.996,0.361)
Ti	(0.677,0.010,0.684)
Ni	(0,0,0.457)
Ni	(2/3,1/3,0.396)
Ni	(0.318,0.978,0.854)
Ni	(0.688,0.021,0.160)

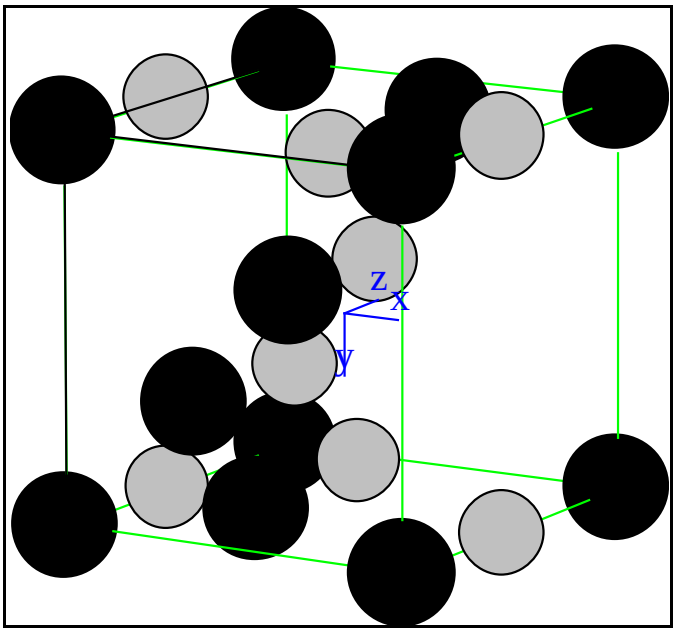

Figure 9: Unit cell of the R phase generated using Carine version 3.1. Ti atoms are black and Ni atoms are gray.

Transformation Paths of TiNi

The normal transformation path taken in TiNi consists of the formation of the B19' phase upon cooling from the B2 phase. However, the appearance of the R phase is possible when cooling is proceeded by a processing route which introduces an internal strain in the alloy. Processes which have been shown to promote R phase include precipitation hardening and any process involving cold working [21-24]. On further cooling, the R phase typically converts to the B19' phase unless the B19' phase is completely suppressed. Previous studies have also shown that the B19' phase may convert to the B2 phase on heating without passing through the R phase even for cases where the R phase is shown to occur [21,22]. Finally the R phase is also shown to have a reduced thermal hysteresis associated with its transformation back to and from the B2 phase in comparison with the B19' phase. This is the result of the significant difference in the transformation strain associated with the R and B19' phase. The B19' phase exhibits 12% strain upon transformation, while the R phase only exhibits 2% [21,23,26].

Influences of the Martensitic Phase Transformations in TiNi

There are a number of factors that can influence the martensitic transformation temperature. One of the most well known for TiNi is the Ni content. It has been shown that a change in Ni content by as little as 0.1at% will cause the Ms temperature to shift by as much as 10C. An equation relating the Ni content to the Ms temperature of TiNi has been developed by Khalil-Allafi, Dlouhy, and Eggeler:

$Ms = (202707761-205968221.1\ C_{Ni}+8370845.646\ C_{Ni}^2 -170093.5974\ C_{Ni}^3 +1728.050544\ C_{Ni}^4- 7.022069029\ C_{Ni}^5)K,$

where Ms is the martensitic start temperature and C_{Ni} is the atomic Ni content [27].
The reason for this shift in Ms temperature is due to the dramatic increase in strength of TiNi with increased Ni content. Because the material is stronger, it is less capable of accommodating the strains associated with the martensitic transformation and thus requires more substantial undercooling to transform [8, 26, 27].

Residual strains and dislocations also impact the martensitic transformation as several authors have shown that increased dislocation densities have a tendency to suppress the formation of the B19' phase though a pinning of the B19' interface as the transformation proceeds [7,23,27,28].

Grain refinement also has the potential to influence the martensitic transformations, but as the majority of the studies have utilized severe plastic deformation to refine the grain size, it is difficult to separate the effects due to the high dislocation density and those due to grain size [9-11,30-34]. Studies conducted on the Ms temperature of various grain sizes of TiNi resulting from growth at temperatures exceeding 900C have shown the Ms temperature to decrease with increasing grain perimeter as given in figure 10 [35]. Classical theories relating to martensitic nucleation suggest that nucleation of martensitic occurs heterogeneously at grain boundaries, suggesting that reductions in grain size should serve to promote the martensitic transformation

by increasing the relative volume of grain boundaries in a material these acting as nucleation sites. [18,19]. Moreover it has been suggested that the accommodation of strains associated with the martensitic phase formation is far easier at smaller grain sizes, thus the transformation temperature increases [31]. Further, TEM studies have suggested that below 100nm the accommodation of the martensitic transformation becomes effortless to the point that the stresses withing a grain are not sufficient to cause multiple twins and therefore only a single variant of nanotwin is observed [30].

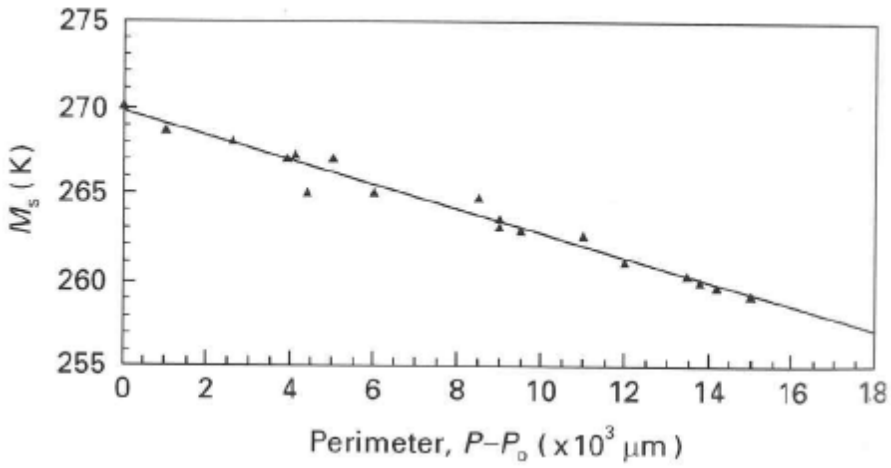

Figure 10: Ms temperature with grain perimeter seen in TiNi after aging for various times at and above 900C. [30]

Precipitation hardening has also been shown to cause the transformation temperatures to shift, however it not widely acknowledged as to whether this result is due to a change in the matrix composition resulting from precipitate formation or if it is due to strain effects associated with the precipitate or some combination of the two [3,10,22,25,27,33,34]. The complex interaction of these variables on the martensitic transformation are reflected by Treppmann and Hornbogen [28] relating the martensitic start temperature with alterations to the Ni content and the yield strength of the material resulting from precipitation,

$$\frac{dMs}{dTA}|t_A = \pm \frac{\partial To}{\partial C_{Ni}} \frac{\partial C_{Ni}}{\partial TA} - \frac{\partial \Delta Tm}{\partial \tau y} \frac{\partial \tau y}{\partial TA},$$

where Ms is the martensitic start temperature, To is the equilibrium temperature between the martensitic and parent phase, C_{Ni} is the ni content of the matrix, T_A is the aging temperature, t_A is the aging time (assumed constant), ΔTm is the undercooling, and τy is the yield strength [30].

It should also be mentioned that the Rs temperature is less effected than the Ms temperature for the previously mentioned cases owing to it smaller transformation strain. As a result, the appearance of the R phase stems from the fact that it is less suppressed compared to the B19' phase, that is the slope of its free energy plotted with temperature changes little while the B19' phase's slope increases in Figure 11 [1,8].

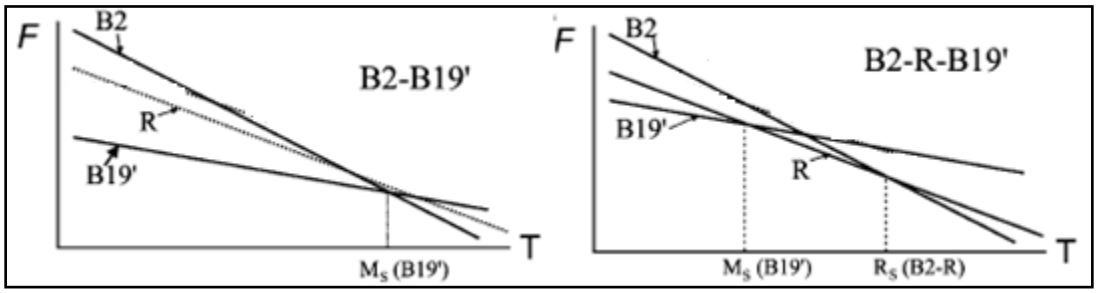

a) b)

Figure 11: Effect of internal strains on the free energy curves of B19', B2, and the R phase: a)unstrained state; b)strained state. [1]

Precipitation

Precipitation is thermodynamically driven by the decomposition of a supersaturated single solid solution phase material into a dual phase material with the precipitate being the second phase formed. To create this supersaturated solid solution a composition must be selected so that at low temperatures the material will exist in a dual phase region of its phase diagram while at high temperatures this material will exist in a single phase region. Therefore upon heating the material will dissolve the second phase and if quenched the single phase will be retained. This single phase will be supersaturated in the second component and also

thermodynamically unstable as the phase diagram predicts two phases instead of a single phase. Heating the material provides enough kinetic energy for the decomposition of this supersaturated single phase into a dual phase material [38].

The heating of the supersaturated material causes the decomposition through diffusion, allowing creation of second phase nuclei and the subsequent growth of these nuclei into precipitates. There are two types of nucleation associated with the formation of a new phase, homogenous and heterogeneous. Regardless of the type of nucleation, the existence of the nuclei is governed by thermodynamics whereby a certain critical size must be attained where the contribution of the bulk free energy associated with the precipitate is larger than the surface energy resulting from its creation. Any nuclei smaller than this critical size are absorbed back into the matrix, while nuclei larger than this will grow. Homogeneous nucleation occurs in materials which lack inclusions, dislocations, and other defects, the location of these initial nuclei being random. During heterogeneous nucleation, there are certain sites such as dislocations or grain boundaries where the critical size is reduced compared to the homogenous case and as a result, nuclei tend to preferentially form at these sites [38].

Precipitation in Ni rich TiNi involves the formation of metastable Ni_4Ti_3 precipitates. Microscopically these precipitates may be described as ellipsoidal in shape, Figure 12 [20,29,40-43], and are formed when heated between 300C and 600C [1,45,46]. Short term aging experiments (aging from 100 to 300C between 10mintues to several hours) indicate that the size of the precipitates first formed is of the order of 2-3nm [44]. The precipitates form on the (111) plane of the B2 matrix and typically thicken in the [111] B2 direction [27, 40, 41, 47]. Up to eight different variants of these precipitates may be formed, although it has been shown that

aging single crystal TiNi under compressive stresses as small as 2MPa oriented in the [111] B2 direction will result in the formation of only one precipitate variant [27,40,48,49].

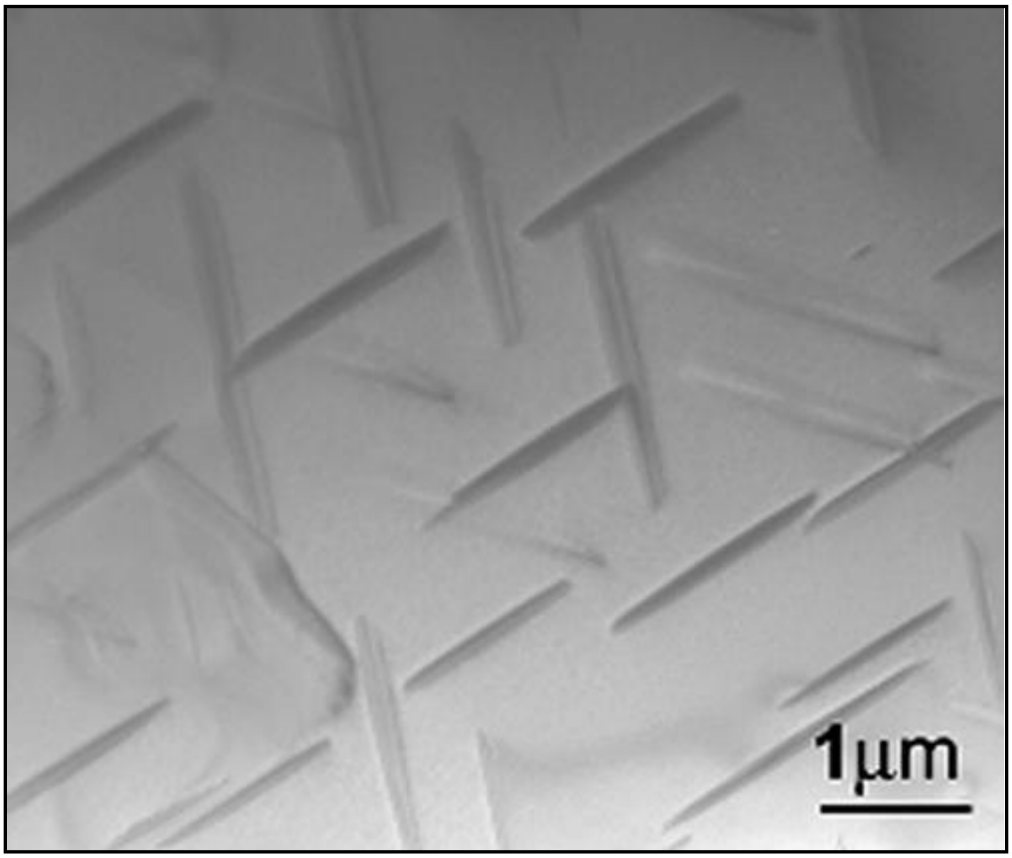

Figure 12: Ni_4Ti_3 precipitates showing lens shaped morphology in a 51%at NiTi alloy aged for 4 hours at 500C after solution treating at 950C for 1 hour. [41]

Ni_4Ti_3 precipitates are initially coherent with the surrounding matrix, this interface becoming incoherent during growth. The critical size at which coherency is lost varies from source to source, as summarized in Table 2 [21, 33, 48-51]. The strain effects associated with the precipitates are also known to be anisotropic in nature, being maximized along the [111] direction [52].

Table 2: Maximum Size for Ni_4Ti_3 Precipitate Coherency

Reference	Size (nm)	Composition
8	500	50.9
22	500	51.14
49	500	51.3
50	400	50.8
51	100	50.9

Crystalographically the precipitate is rhombohedral in structure with a lattice parameter of 6.71 Angstroms and an angle of 113.7 degrees, Figure 13, atomic positions being summarized in Table 3 [53].

Table 3: Atomic Positions of Ti and Ni atoms in Ni_4Ti_3 Precipitates in Cartesian Coordinates [53]

Atom	Position
Ni	(0,0,0)
Ni	(1/2,1/2,1/2)
Ni	(0.0605,0.5931,0.7574)
Ti	(0.4989,0.1125,0.2513)

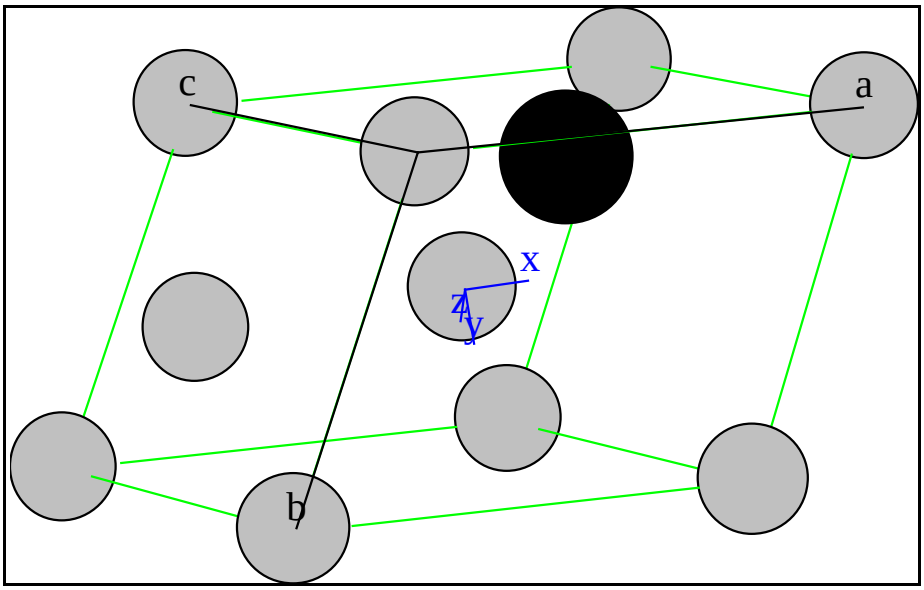

Figure 13: Unit cell of Ni_4Ti_3 precipitate. Gray atoms are Ni atoms and black represents Ti atoms.

Finally for very long aging times or at temperatures between 600C and the TiNi-Ni_3Ti solvus, Ni_4Ti_3 precipitates will transform into the equilibrium Ni_3Ti phase [1].

CHAPTER TWO REFERENCES

[1]K.Otsuka, X.Ren, "Physical Metallurgy of Ti-Ni-based Shape Memory Alloys", Prog. Mater. Sci., Vol. 50, 2005: 511-678.

[2]M.F-X.Wagner, W.Windl, "Elastic Anisotropy of Ni_4Ti_3 from First Principles", Scripta Mater. Vol. 60, 2009: 207-210.

[3]K.Gall, H.Sehitoglu, Y.I.Chumlyakov, I.V. Kireeva, "Tension-compression Asymmetry of the Stress-strain Response in Aged Single Crystal and Polycrystalline NiTi", Acta Mater., Vol. 47, 1999: 1203-1217.

[4]F.X.Gil-Mur, D.Rodriguez, J.A.Planell, "Grain Growth of NiTi Alloy and Its Influcence on the Martensitic Transformation Temperatures and Thermodynamic Parameters", Titanium '95: Science and Technology: 2399-2406.

[5]C.M.Wayman, "Shape Memory and Related Phenomena", Prog. Mat. Sci,Vol. 36 ,1992: 203-224.

[6] C.Efstathiou, H.Sehitoglu, "Local Transformation Strain Measurements in Precipitated NiTi Single Crystals", Scripta Mater. ,Vol. 59, 2008: 1263-1266.

[7]S.K.Wu, H.C.Lin, P.C.Cheng, "Multi-Strengthening Effects on the Martensitic Transformation Temperatures of TiNi Shape Memory Alloys", J. Mat. Sci., Vol. 34 (22) 1999: 5669-5675.

[8]J.Khalil-Allafi, X.Ren, G.Eggeler, "The Mechanism of Multistage Martensitic Transformations in Aged Ni-rich NiTi Shape Memory Alloys", Acta Mater. ,Vol. 50 2002: 793-803.

[9] T.Waitz, V.Kazykhanov, H.P.Karnthaler, "Martensitic Phase Transformations in Nanocrystalline NiTi Studied by TEM", Acta Mater., Vol. 52 2004: 137-147.

[10] H.Nakayama, K.Tsuchiya, M.Umemoto, "Crystal Refinement and Amorphisation by Cold Rolling in TiNi Shape Memory Alloys", Scripta Mater., Vol. 44, 2001: 1781-1785.

[11]E. Prokofiev, D. Gunderov, A. Lukyanov, V. Pushin, R. Valiev, "Mechanical Behavior and Stress-induced Martensitic Transformation in Nanocrystalline $Ti_{49.4}Ni_{50.6}$ Alloy", Mater. Sci. Forum, Vol. 584-586, 2008: 470-474.

[12]M. Vedani, P. Bassani, A. Tuissi, G. Angella, "Ultrafine Grained Alloys Produced by Severe Plastic Deformation; Issues on Microstructural Control and Mechanical Behaviour", Metall. Sci. Tech., 2004: 21-30.

[13]S. Rusz, K. Malanik, "Using Severe Plastic Deformation to Prepare Ultra Fine-grained Materials by ECAP Method", Arch.Mater. Sci. Eng., Vol. 28, 2007:683-686.

[14]S. Rusz, M. Greger, M. Kubicek, M. Pastrnak, “Preparing Nanostructural Materials by ECAP Method of Severe Plastic Deformation”, International Conference on Engineering Education and Research, 2004: 757-762.

[15] V.M. Segal, “Engineering and Commercialization of Equal Channel Angular Extrusion (ECAE)”, Mater. Sci. Eng. A., Vol. 386, 2004: 269-276.

[16]I. Tamura, C.M. Wayman, “Martensitic Transformations and Mechanical Effects”, *Matensite: A Tribute to Morris Cohen*, eds. G.B. Olson and W.S. Owen, ASM International ,1992: 227-242.

[17] L.Kaufman, M. Cohen, “Thermodynamics and Kinetics of Martensitic Transformations”, Prog. Met. Phys. ,Vol. 7,1958: 165-246.

[18]G.Ghosh, G.B. Olson, “Kinetics of F.C.C-B.C.C. Heterogeneous Martensitic Nucleation—I. The Critical Driving Force for Athermal Nucleation”, Acta. Metall. Mater ,Vol. 42, 1994: 3361-3370.

[19]G.Ghosh, G.B. Olson, “Kinetics of F.C.C-B.C.C. Heterogeneous Martensitic Nucleation—II. Thermal Activation”, Acta. Metall. Mater Vol. ,42 ,1994: 3371-3379.

[20]S.D. Prokoshkin, A.V. Korotitskiy, V. Brailovski, S. Turenne, I. Y. Khmelevskaya, I.B. Trubitsyna, “On the Lattice Parameters of Phases in Binary Ti-Ni Shape Memory Alloys”, Acta Mater., Vol. 52, 2004: 4479-4492.

[20]L.Bailaillard, J.E.Bidaux, R.Gotthardt, “Interaction between Microstructure and Multiple-step Transformation in Binary NiTi Alloys Using In-situ Transmission Electron Microscopy Observations”, Philos Mag. A ,Vol. 78. (2), 1998: 327-344.

[21]G.B.Stachowiak, P.G.McCormick, “Shape Memory Behaviour Associated with the R and Martensitic Transformations in a NiTi Alloy”, Acta Metall., Vol.36 (2), 1988: 291-297.

[22]M.C.Carroll, CSomsen, G.Eggeler, “Multiple-Step Martensitic Transformations in Ni-rich NiTi Shape Memory Alloys”, Scripta Mater., Vol. 50, 2004: 187-192.

[23]M.Peltonen, T.Lindroos, M.Kallio, “Effect of Ageing on Transformation Kinetics and Internal Friction on Ni-rich Ni-Ti Alloys”, J Alloy Comp., Vol. 460, 2008: 237-245.

[24]D.Stroz, “Studies of the R-phase Transformation in a Ti-51at.%Ni Alloy by Transmission Electron Microscopy”, Scripta Mater.,Vol. 47, 2002: 363-369.

[25]J.Khalil-Allafi, G.Eggeler, W.W.Schmahl, D.Sheptyakov, “Quantitative Phase Analysis in Microstructures which Display Multiple Step Martensitic Transformations in Ni-rich NiTi Shape Memory Alloys”, Mater Sci Eng. A, Vol. 438-440, 2006: 593-596.

[26]A.Dlouhy, J.Kahalil-Allafi, G.Eggeler, “On the Determination of the Volume Fraction of Ni_4Ti_3 Precipitates in Binary Ni-rich NiTi Shape Memory Alloys”, Z. Metallkd., Vol. 95 (6), 2004: 518-524.

[27] C.P.Frick, A.M.Ortega, J.Tyber, K.Gall, H.J.Maier, “Multiscale Structure and Properties of Cast and Deformation Processed Polycrystalline NiTi Shape-memory Alloys”, Metall. Mat. Trans. A ,Vol. 35A, 2004: 2013-2025.

[28] D.Treppmann, E.Hornbogen, “Effect of Dislocation Substructure and Decomposition on the Course of Diffusionless Transformations”, J.Phys. IV France ,Vol. 5, 1995: 211-216.

[29] C.Y.Xie, Z.G.Fan, Z.H.Li, G.Q.Xiang, X.H.Cheng, “Effects of High Temperature ECAE Process on Microstructures and Martensitic Transformaiton of TiNi Shape Memory Alloy”, Mat. Sci. Forum, Vol. 503-504, 2006: 1013-1018.

[30] V.G. Pushin, R.Z. Valiev, Y.T. Zhu, D.V. Gunderov, N.I. Klourov, T.E. Kuntsevich, A.N. Uksusnikov, L.I. Yurchenko, “Effect of Severe Plastic Deformation on the Behavior of Ti-Ni Shape Memory Alloys”, Mater. Trans., Vol. 47, 2006: 694-697.

[31]R. Valiev, D. Gunderov, E. Prokofiev, V. Pushin, Y. Zhu, “Nanostructuring of TiNi Alloy by SPD Processing for Advanced Properties”, Mater. Trans., Vol. 49,2008: 97-101.

[32] T.Waitz, H.Karnthaler, T.Antretter, F.D.Fischer, “Martensitic Phase Transformations of Bulk Nanocrystalline NiTi Alloys”, Solid-to-Solid Phase Transformations in Inorg. Mat., Vol. 2 ,2005: 885-898.

[33]C.P.Frick, A.M.Ortega, J.Tyber, A.El.M. Maksound, H.J.Maier, Y.Liu, K.Gall, “Thermal Processing of Polycrystalline NiTi Shape Memory Alloys”, Mat. Sci. Eng. A, Vol. 405, 2005: 34-49.

[34]A.M. Ortega, J. Tyber, C.P. Frick, K. Gall, H.J. Maier, “Cast NiTi Shape-Memory Alloys”, Adv. Eng. Mater. Vol. 7, 2005: 492-507.

[35]F.J. Gil, J.M. Manero, J.A. Planell, “Effect of Grain Size on the Martensitic Transformation in NiTi Alloy”, J. Mater. Sci. Vol. 30, 1995: 2526-2530.

[36]E.A. Prokofiev, J.A. Burow, E.J. Payton, R. Zarnetta, J. Frenzel, D.V. Gunderov, R.Z. Valiev, G. Eggeler, “Suppression of Ni_4Ti_3 Precipitation by Grain Size Refinement in Ni-rich NiTi Shape Memory Alloys”, Adv. Eng. Mater. Vol. 12, 2010: 747-753.

[37] V.Demers, V.Brailovski, S.Prokoshkin, K.Inaekyan, E.Bastarash, I.Khmelevskaya, S.Dobatkin, “Functional Properties of Nanostructured Ti-50.0 at% Ni Alloys”, J. ASTM Int., Vol. 3 (6), 2006: 34-44.

[38]H.K. Hardy, T.J. Heal, “Report on Precipitation”, Prog. Met. Phys. ,Vol. 5, 1954: 143-278.

[39]X. Jiang, H. Zhang, Q. Wen, Z. Zhong, Y. Zheng, X. Tang, "Crystallization Kinetics of CoNbZr Amorphous Alloys Thin Films", Mater. Chem. Phys. Vol. 88 2004: 197-201.

[40] J.Michutta, M.C.Carroll, A.Yawny, C.Somsen, K.Neuking, G.Eggeler, "Martensitic Phase Transformation in Ni-rich NiTi Single Crystals with One Family of Ni_4Ti_3 Precipitates", Mat. Sci. Eng. A ,Vol. 378 ,2004: 152-156.

[41] O.Bojda, G.Eggeler, A.Dlouhy, "Precipitation of Ni_4Ti_3-variants in a Polycrystalline Ni-rich NiTi Shape Memory Alloy", Scripta Mater., Vol. 53, 2005: 99-104.

[42]D. Schryvers, W. Tirry, Z.Q. Yang, "Measuring Strain Fields and Concentration Gradients Around Ni_4Ti_3 Precipitates", Mater. Sci. Eng. A, Vol. 438-440, 2006: 485-488.

[43]Z.Yang, W.Tirry, D.Lamoen, S.Kulkova, D.Schryvers, "Electron Energy-loss Spectroscopy and First-principles Calculation Studies on a Ni-Ti Shape Memory Alloy", Acta Mater., Vol. 56, 2008: 395-404.

[44]J.I. Kim, S. Miyazaki, "Effect of Nano-scaled Precipitates on Shape Memory Behavior of Ti-50.9at%Ni Alloy," Acta Mater., Vol. 53, 2005: 4545-4554.

[45] D.Treppmann, E.Hornbogen, "On the Influence of Thermomechanical Treatments on Shape Memory Alloys", J.Phys IV France, Vol. 7, 1997: 211-220.

[46] D.Wurzel, "Marforming and Tempering of Binary Ni-Ti Alloys Including Precipiation Effects", Mat. Sci Eng A, Vol. 273-275, 1999: 634-638.

[47] P.Filip, K.Maznec, "On Precipitation Kinetics in TiNi Shape Memory Alloys", Scripta Mater., Vol. 45, 2001: 701-707.

[48] J.Khalil-Allafi, A.Dlouhy, G.Eggeler, "Ni_4Ti_3-Precipitation during Aging of NiTi Shape Memory Alloys and Its Influence on Martensitic Phase Transformations", Acta Mater., Vol. 50, 2002: 4255-4274.

[49] J.Michutta, C.Somsen, A.Yawny, A.Dlouhy, G.Eggeler, "Elementary Martensitic Transformation Processes in Ni-Rich NiTi Single Crystals with Ni_4Ti_3 Precipitates", Acta Mater., Vol. 54, 2006: 3525-3542.

[50] K.Gall, N.Yang, H.Sehitoglu, Y.I.Chumlyakov, "Fracture of Precipitated NiTi Shape Memory Alloys", Int. J. Fracture, Vol. 109, 2001: 189-207.

[51] K.Gall, H.J.Maier, "Cyclic Deformation Mechanisms in Precipitated NiTi Shape Memory Alloys", Acta Mater., Vol. 50 ,2002: 4643-4657.

[52] W.Tirry, D.Schryvers, "High Resoluition TEM Study of Ni_4Ti_3 Precipitates in Austenitic $Ni_{51}Ti_{49}$" Mat. Sci. Eng. A, Vol. 378, 2004: 157-160.

[53] W. Tirry, D. Schryvers, K. Jorissen, D. Lamoen, “Quantitative Determination of the Crystal Structure of Ni_4Ti_3 Precipitates”, Mater. Sci. Eng. A, Vol. 438-440, 2006: 517-520.

CHAPTER THREE

EXPERIMENTAL PROCEDURES

All materials used in this study were provided by Intrinsic Devices Inc. in the form of a 25.2mm bar, having a nominal composition of Ti-50.6at% Ni. The alloy was initially solution treated at 850C for one hour and water quenched (ST 850). Solution treatment was followed by equal channel angular pressing (ECAP), Figure 14, at 450C for 8 passes (Φ=110 degrees), using route Bc (sample being rotated by 90 degrees after each pass). A portion of the ECAPed material was solution treated at 800C for one hour and water quenched (ST 800). Finally sections of ST 800 and ECAPed Ti-50.6at% were aged at temperatures between 400C and 550C for times between 1 and 100 hours. Solution treatment and aging of all samples were terminated by water quenching. Prior to aging the sections where coated with Yittria powder.

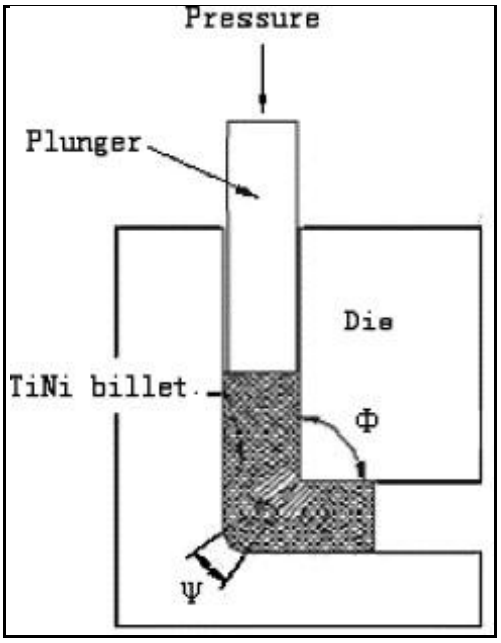

Figure 14: Schematic of the ECAP process.

A TEM image of the ECAP material received courtesy of R. Valiev is provided in Figure 15. The grain size of the ECAP material was reported to fall between 200 and 300nm with an absence of grain growth seen for aging at 400C for up to 100 hours [1].

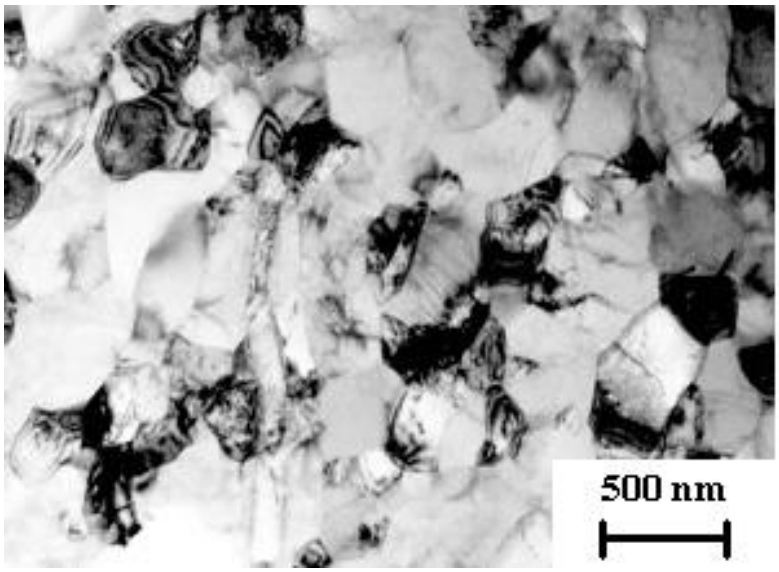

Figure 15: Microstructure of the ECAP material [1].

Optical microscopy was used to determine the grain size of the ST 850 sample, the ST 800 sample, and an aged ST 850 sample. All optical samples were polished starting with 600 grit paper through 1000 girt paper, before being polishing for 4 hours in suspensions of 0.3 μm and 0.05 μm alumina. The samples were finished by polishing in a Vibromet with 50-70 nm colloidal silica overnight. Samples were dipped in pure ethanol and etched for 70 seconds in a solution containing 2% by volume HF and 18% by volume HNO_3 diluted in water. Grain size analysis of the resulting optical images were performed using the linear intercept method given by ASTM standard E 112-96. Details of these analyses can be found in the Appendix A.

The average grain size of the ST 850 was determined to be 39 μm, while ST 850 aged at 550C for 10hrs was shown to have a grain size of 71 μm. Similarly ST 800 had an average grain size of 21μm, the microstructures of these samples being given in Figure 16.

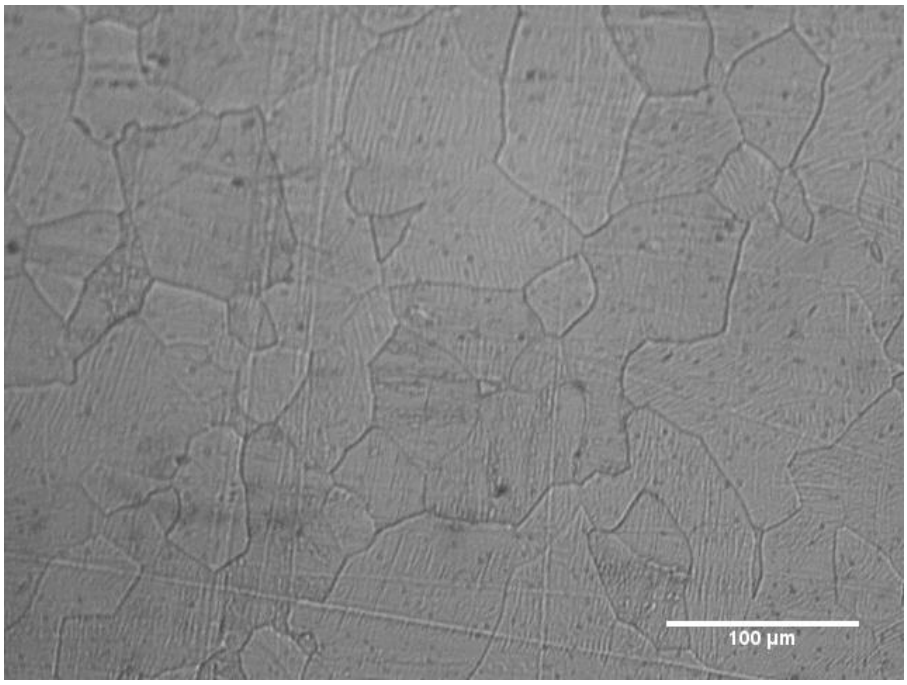

a)

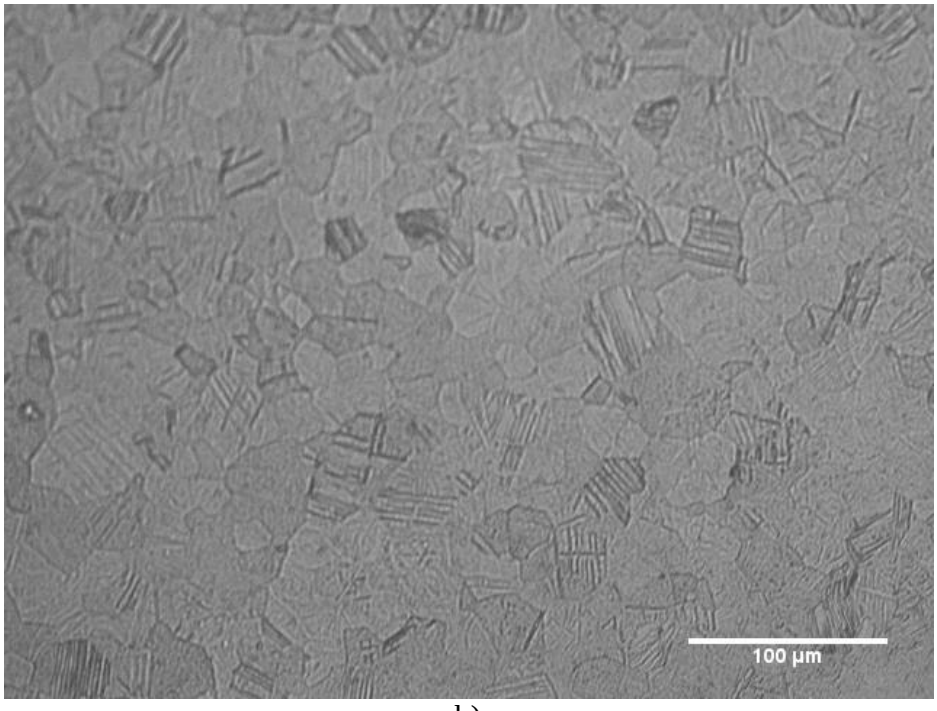

b)

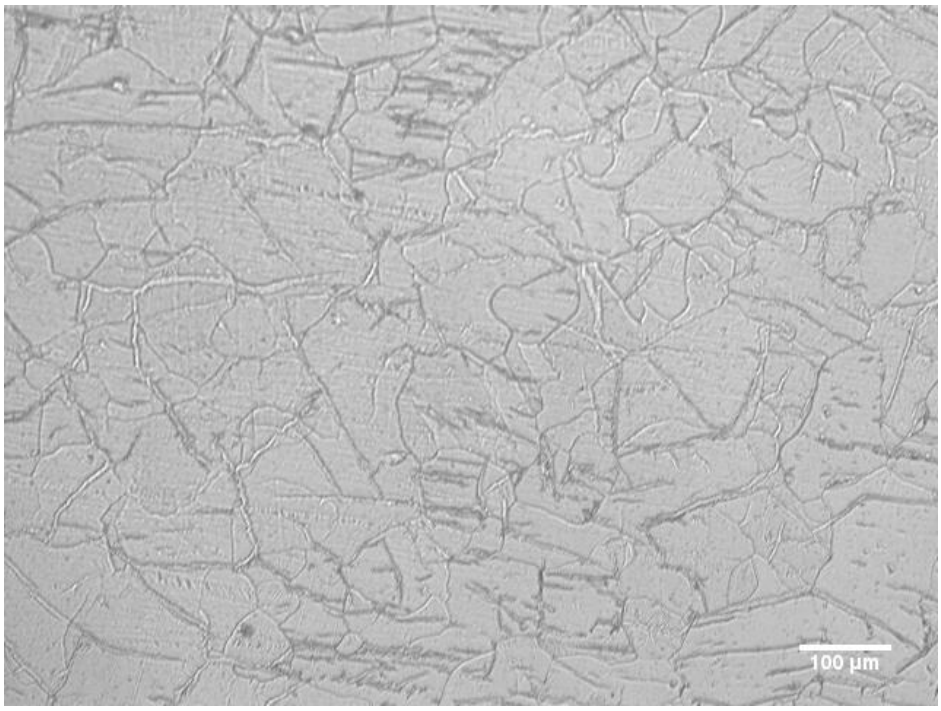

c)

Figure 16: Microstructure of the aged and unaged solution treated samples: a) ST 850 Sample; b) ST 800 Sample; c)ST 850 sample aged at 550C for 10hrs.

Differential scanning calorimetry was used to establish the shape memory transformation of the unaged and aged ECAP, ST 800, and ST 850 conditions. The martensite start (Ms), finish (Mf), the austenite start (As) as well as the austenite finish (Af), the R phase start (Rs), and the R phase finish (Rf) temperatures, the enthalpy of the transformations, and the thermal hysteresis of the transformations (Ms-As) were determined. 50 to 80 mg samples were cut from the processed rods using a 4000 series Buehler Isomet metallographic saw using a Pro-slicer cutting blade. Samples were cleaned with pure ethanol and loaded in alumina crucibles. A Netzsch Pegasus 404C DSC backfilled with prepurified helium containing 1ppb O_2 and equipped with a Netzsch CCL 200 cooling system and a low temperature head allowed temperatures between -110 and 700C to be attained. The backfilling procedure for these experiments consisted of initial evacuation of the DSC chamber below 10 mbar using a KNF fore pump, and followed by a

Pheifer model TMH 064 turbo pump until the chamber was evacuated to 10^{-4} mbar. The pumps were deactivated and the system backfilled with gettered He gas, the previously purging and backfilling procedure was then repeated. The DSC exhaust valve was opened and He gas continuously passed through the DSC.

After loading and evacuation the system was heated to 100C at 10C/min holding for 3 minutes to relieve possible stresses arising from sample preparation and returning the alloy to a complete austenitic state. The sample was automatically cooled to -80C at a cooling rate of 10 C/min using the gaseous nitrogen cooling setting of the CCL 200 cooling system. This cooling step was followed by reheating to 100C at a rate of 10C/min and finally returning to 25C. Data acquisition rates of 100 data points per minute were used for the heating and cooling segments. Partial cooling-heating experiments were also performed to assist in separation and coupling of transformation peaks obtained during cooling and heating. Again the sample was heated prior to 100C prior to cooling to preselected temperatures and returning to room temperature.

Calibration of the temperature and the enthalpy for the DSC experiments were based on the freezing of Hg. 248.9 mg of Hg was placed in an alumina crucible and cooled to a temperature of -70C followed by reheating to 25C. This temperature program was repeated to allow for any possible instabilities arising from the first run, only data from the second run was utilized for calibration purposes. The backfilling procedure was identical to the DSC runs. Heating and cooling rates of 10C/min were used for the calibration run. Knowing the freezing point of mercury, -38.9C [2], the deviation from this value was determined and the subsequent TiNi DSC curves corrected as discussed in the Appendix B. The freezing point given by the run is taken as the point where the exotherm of the cooling segment is first detected.

Analysis of the DSC runs was performed using the integration tool in Origin Pro version 8.1 assuming a straight line for the baseline option, the start and finish temperatures being taken as the limits of the integration (Figure 17) these having been defined by establishing the temperature where initial deviation in DSC response with temperature occurred, $\frac{dQ}{dT}$ = constant, either during heating or cooling. In some instances, it was not possible to integrate single peaks due to peak overlap. In these instances the peaks were fitted manually and the peak temperatures and enthalpy changes were estimated.

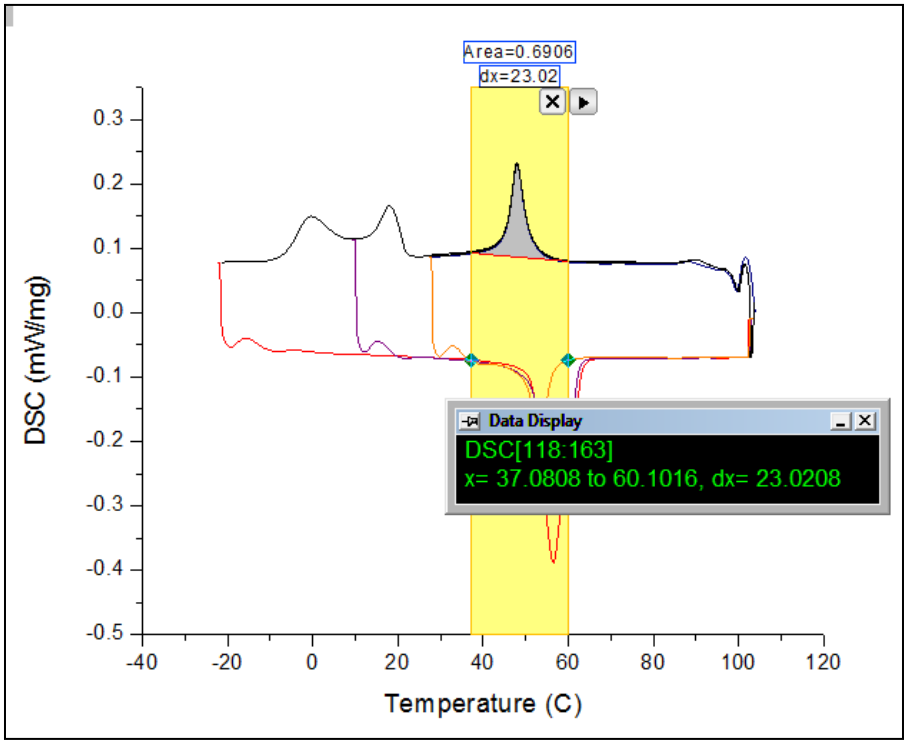

Figure 17: Screenshot showing the integration results as given in Origin Pro.

X-ray diffraction (XRD) was performed on select samples to confirm the phase transformations deduced from the anisothermal DSC runs. Simulations for the XRD patterns were performed using Carine version 3.1 and are given in Appendix C. XRD samples were cut using a Buehler 4000 series metallographic saw equipped with a Pro-slicer blade and polished starting with 400 grit SiC paper and finishing with 1000 grit SiC paper. Samples were polished

on Buehler vibromets filled with 0.3 and 0.05 μm alumina suspensions. Final polishing was performed using a Buehler vibromet filled with 50 to 70 nm colloidal silica. After polishing, the XRD samples were cleaned in an ultrasonic bath of ethanol, wrapped in lens paper and stored in a sample envelope. Some samples were also cooled to -60C in liquid nitrogen and allowed to return to room temperature to allow for the appearance of certain martensitic phases seen in the DSC runs. The conditions examined are listed in Table 4. All XRD tests were performed on a Scintag XDS 2000 fitted with a model R111902 Mostek solid state detector utilizing Cu Kα radiation and a Ni filter combined with No. 4 and No2. slits. Samples were mounted in a polycarbonate specimen holder using a leveling press. The Scintag XDS was ran using a max tube power of 1.21kW and a filament current of 3.24 A. The current and voltage settings for the XRD were 30mA and -40kV, respectively. A step of 0.01 degrees and a count time of 15 seconds were used for the scan settings. Calibration for the XRD was routinely performed with a (510) Si single crystal with an accuracy of +/- 0.001°. Origin Pro version 8.1 was used for analysis whereby the peak positions corresponded to 2theta values where the peaks were at their maximum.

Table 4: List of XRD Samples and Conditions

Sample	Condition
ST Only	Heated to 100C, return to room temperature.
ST 400C 10hrs	Heated to 100C, return to room temperature.
ST 400C 10hrs -60cooled	Cooled to -60C, return to room temperature.
ST 450C 100hrs	Heated to 100C, return to room temperature.
ST 450C 100hrs -60cooled	Cooled to -60C, return to room temperature.
ECAP Only	Heated to 100C, return to room temperature.
ECAP 400C 10hrs	Heated to 100C, return to room temperature.
ECAP 400C 10hrs -60cooled	Cooled to -60C, return to room temperature.
ECAP 500C 100hrs	Heated to 100C, return to room temperature.
ECAP 500C 100hrs -60cooled	Cooled to -60C, return to room temperature.

CHAPTER THREE REFERENCES

[1] R. Valiev, D. Gunderov, E. Prokofiev, V. Pushin, Y. Zhu, “Nanostructuring of TiNi Alloy by SPD Processing for Advanced Properties”, Mater. Trans., Vol. 49, 2008: 97-101.

[2] J.E. Callanan, K.M. McDermott, “Fusion of Mercury a New Certified Standard for Differential Scanning Calorimetry”, J.Chem.Thermodynamics, Vol. 22, 1990: 225-230.

CHAPTER FOUR

RESULTS

Solution Treated Conditions

DSC results for material solution treated for 1 hour at 800C (ST800) exhibited a single peak on both cooling and heating, Figure 18, the martensite start and finish temperatures on cooling being 21C and -32C, respectively, with a corresponding enthalpy change of 28.4 J/g, the start and finish temperatures on heating were 9C and 47C, respectively, with a corresponding enthalpy change of -29.2 J/g.

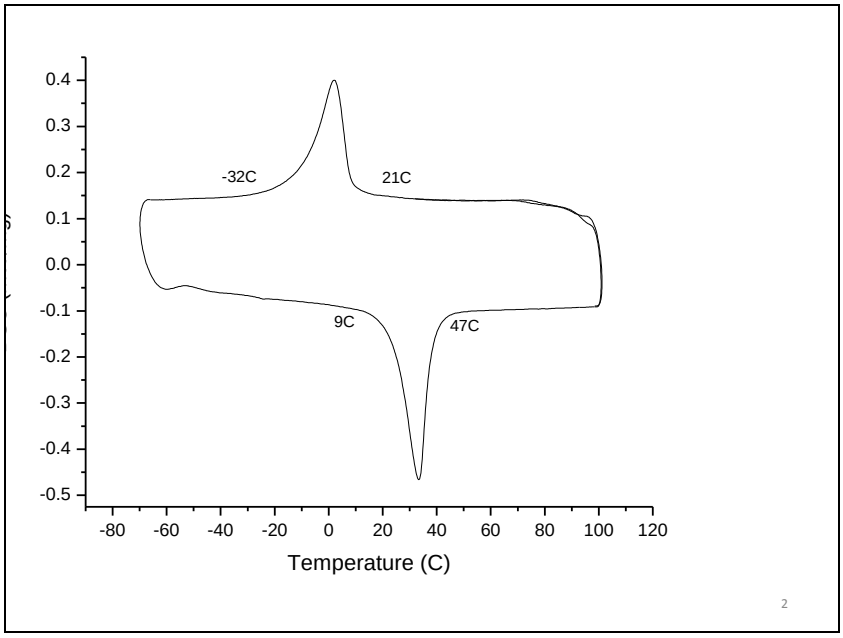

Figure 18: DSC results for material solution treated at 800C for 1 h and water quenched.

X-ray diffraction results for this condition, Figure 19, exhibited a single sharp and intense peak centered at 42.56°, which corresponded to the (110) reflection of the B2 phase. No evidence of the (100) B2 peak was observed, suggesting that prior working of the TiNi alloy examined in this study had resulted in a deformation texture. The x-ray results however confirm that the single reaction observed during cooling involved the B2 → B19' transformation, with

the reverse B19' → B2 transformation occurring on heating. Further support for this interpretation is provided by nearly identical enthalpy changes observed during cooling and heating.

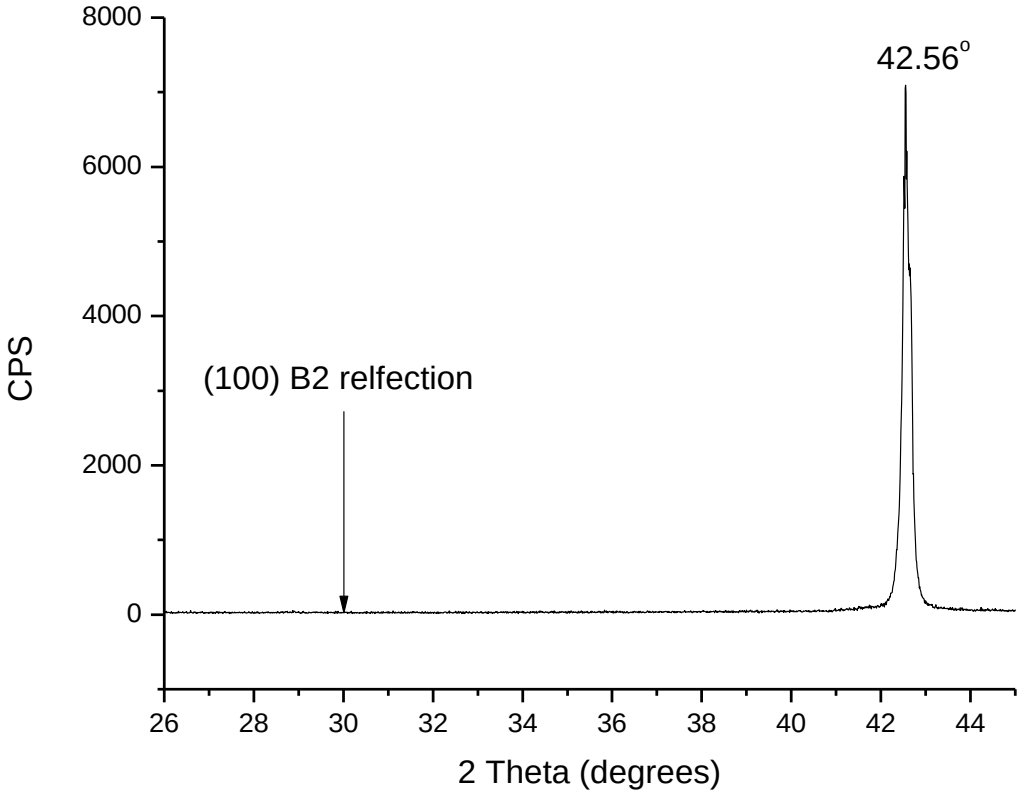

Phase	hkl	Simulated 2theta	Observed 2theta
B2	110	42.55	42.56
B2	100	29.86	NA

Figure 19: X-ray diffraction results for Ti-50.6 at% Ni solution treated at 800C for 1 h and water quenched.

Similarly, material solution treated at 850C for 1h and water quenched displayed single peaks on cooling and heating, Figure 20, these again corresponding to the B2 ↔ B19' transformation. The Ms and Mf temperatures during cooling were 16C and -28C, with a

corresponding enthalpy change of 20.6 J/g , the As and Af temperatures on heating being 0C and 48C, respectively, with a corresponding enthalpy change of -21.9 J/g.

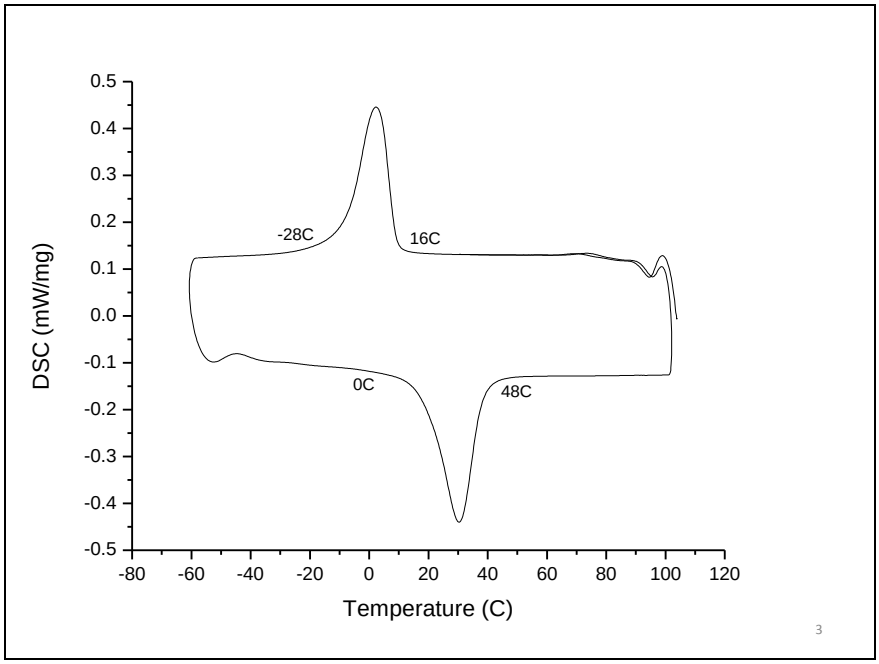

Figure 20: DSC results for material solution treated at 850C for 1 h and water quenched

Solution Treated and Aged

Singular Peaks

DSC observations for material solution treated at 800C for 1 h and aged at 400C for 1 h displayed single peaks on cooling and heating, Figure 21. The M_s and M_f temperatures during cooling were 8C and -19C, respectively, with a corresponding enthalpy change of 27.6 J/g, while the A_s and A_f temperatures on heating were 13C and 55C, with a corresponding enthalpy change of -29.1 J/g. While the 1 h aging treatment considered resulted in a 13C decrease in the M_s temperature compared with the unaged solution treated result, Figure 18, show good agreement between the enthalpy changes associated with the transformations observed, supporting the conclusion that the single peaks observed after the 1 h age correspond to the B2↔B19' reversible reaction.

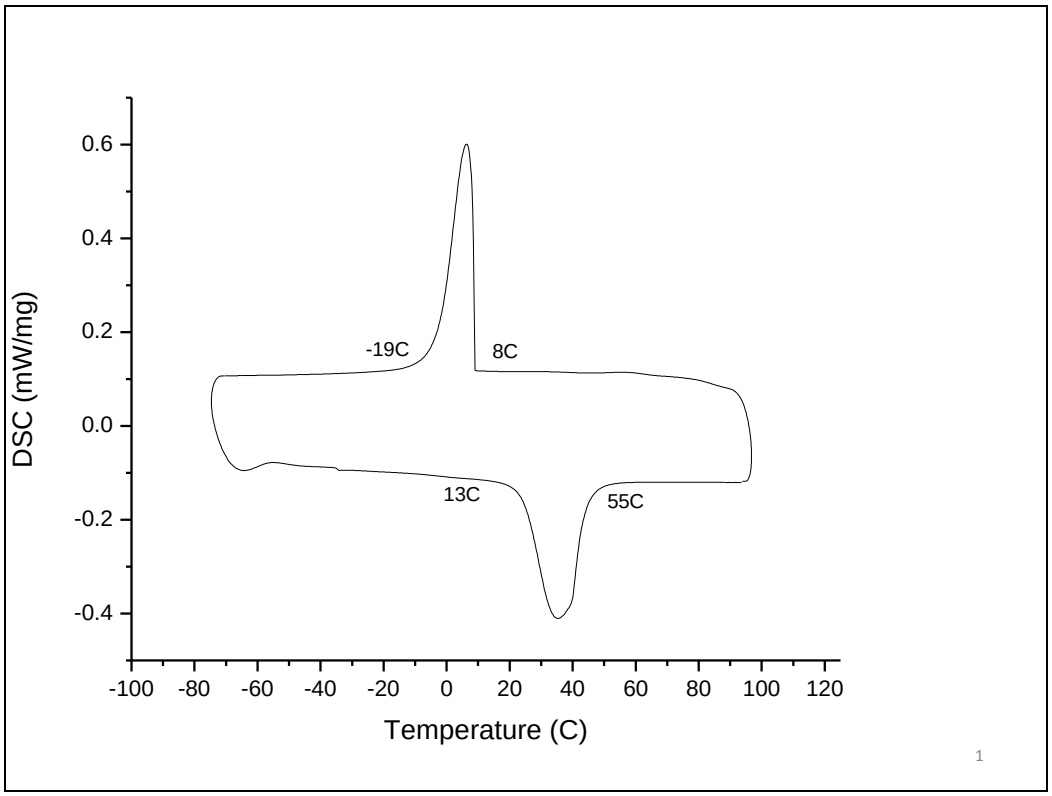

Figure 21: DSC results for material solution treated at 800C for 1 h, aged at 400C for 1h and water quenched.

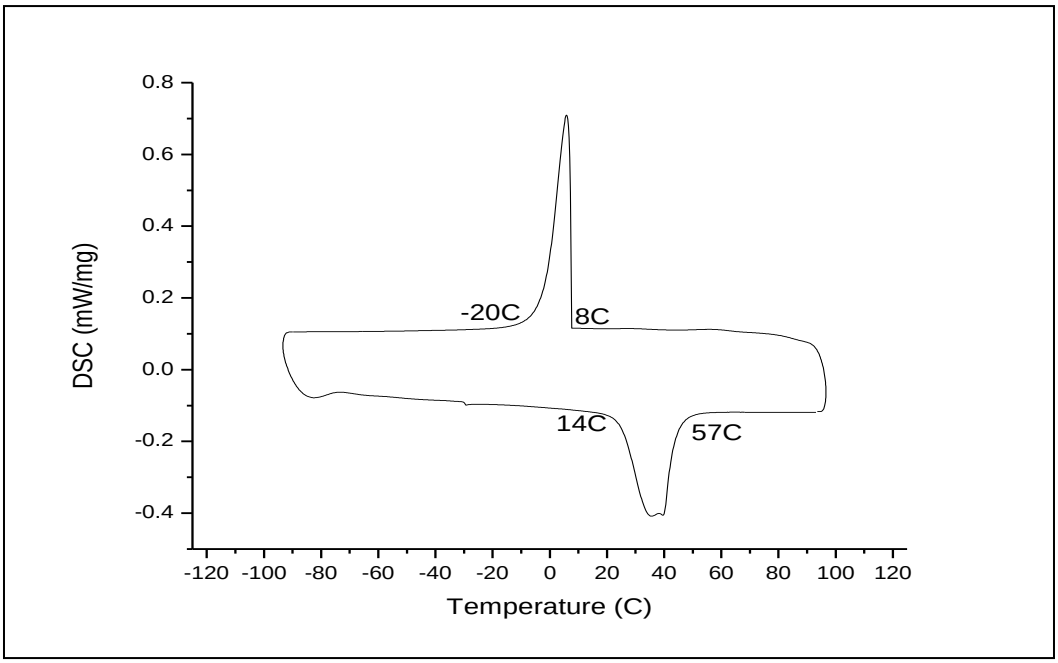

Figure 22: DSC results for material solution treated at 800C for 1h, aged at 450C for 1h and water quenched.

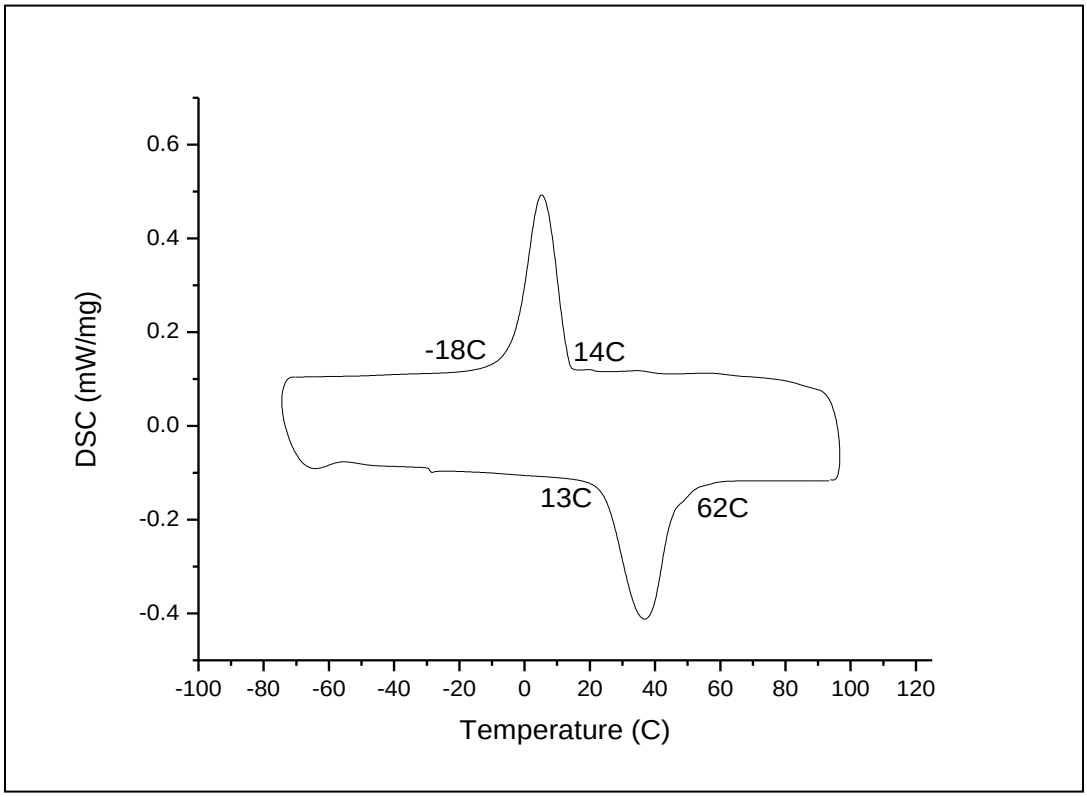

Figure 23: DSC results for material solution treated at 800C for 1h, aged at 450C for 10h and water quenched.

Indeed increasing the aging temperature to 450C at a constant aging time, 1 h, Figure 22, did not materially impact these results, a single peak on cooling and on heating being observed. The M_s and M_f temperatures were 8C and -20C, respectively, with a corresponding enthalpy change of 25.2 J/g, the A_s and A_f temperatures being 14C and 57C, with a corresponding enthalpy change of -26.8.1 J/g. These results are in close agreement with those obtained for material aged for 1 h at 400C, therefore transformation after 450C for 1 h also involved B2↔B19'.

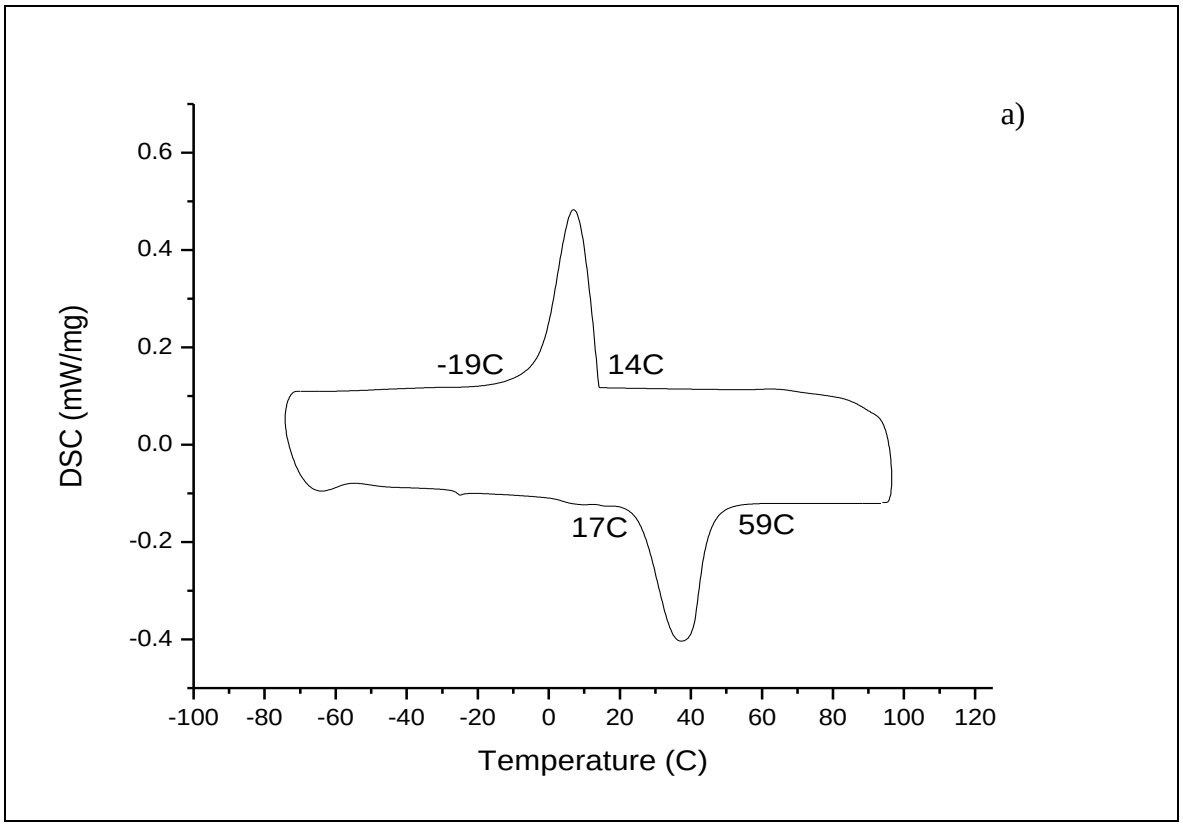
a)
DSC (mW/mg)
0.6
0.4
0.2
0.0
-0.2
-0.4
-19C
14C
17C
59C
-100 -80 -60 -40 -20 0 20 40 60 80 100 120
Temperature (C)

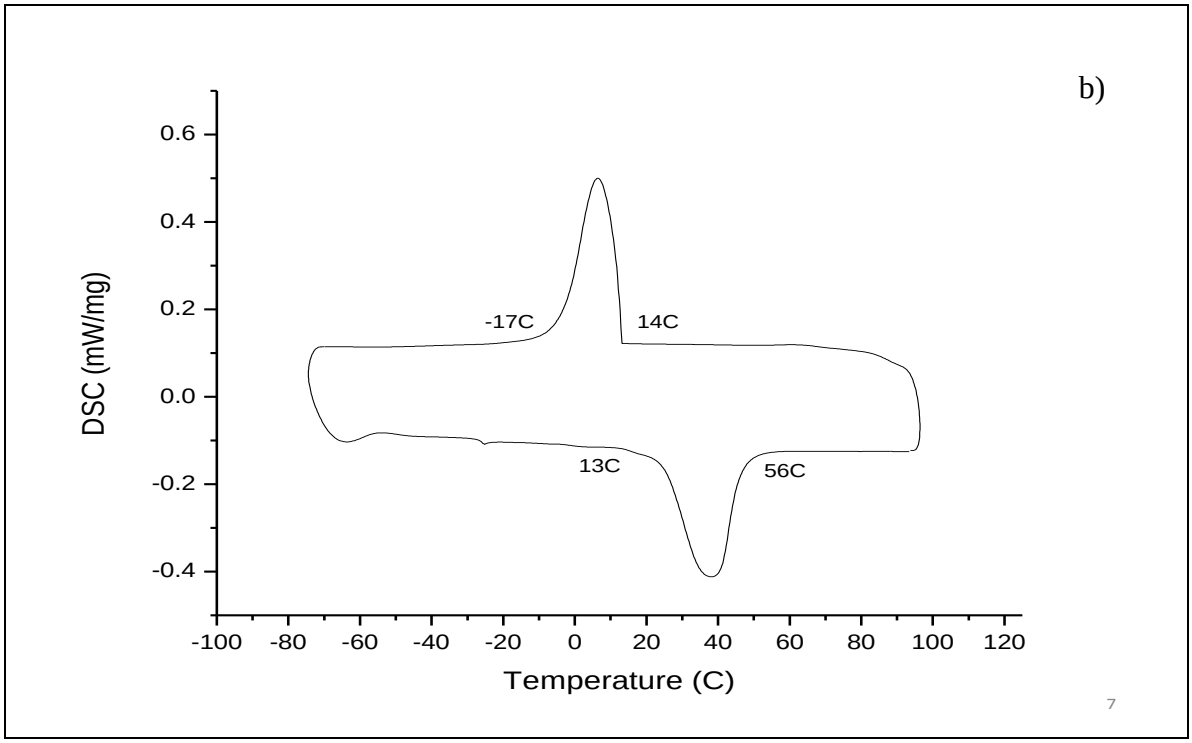
b)
DSC (mW/mg)
0.6
0.4
0.2
0.0
-0.2
-0.4
-17C
14C
13C
56C
-100 -80 -60 -40 -20 0 20 40 60 80 100 120
Temperature (C)
7

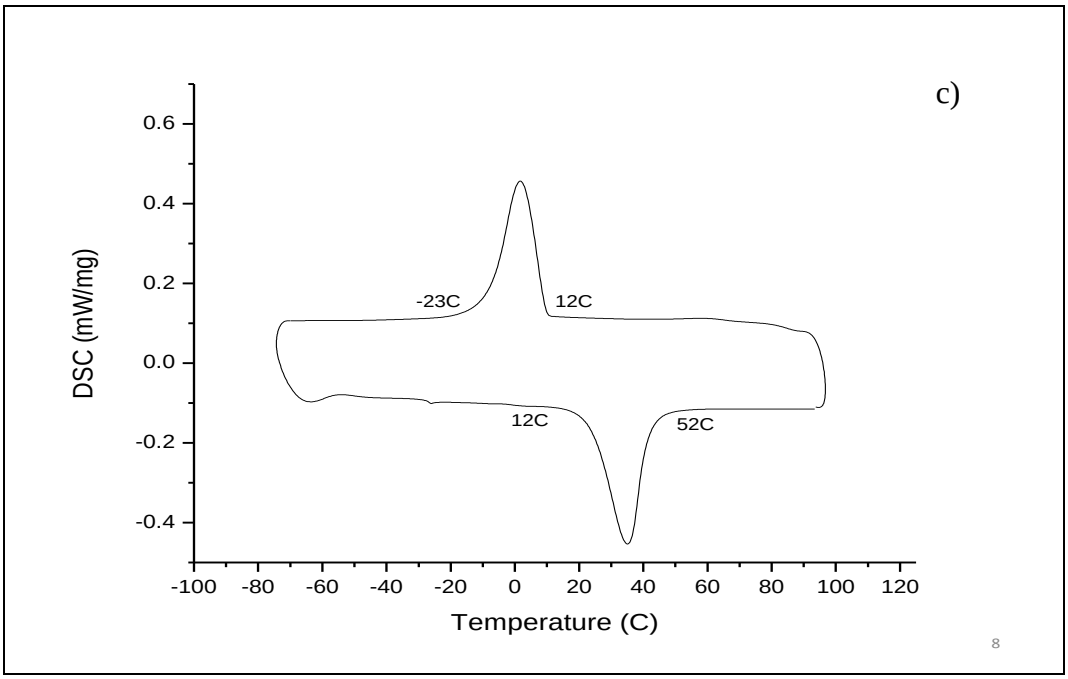

Figure 24: DSC results after solution treatment at 800C for 1h, aging at 550C for (a) 1h, (b) 10 h and (c) 100h and water quenched.

Similar results were also obtained after increasing the aging time to 10 h at 450C, Figure 23, a single peak on heating and cooling being observed. The M_s and M_f temperatures were 14C and -18C, respectively, with a corresponding enthalpy change of 24.8 J/g, the A_s and A_f temperatures being 13C and 62C, with a corresponding enthalpy change of -26.8.1 J/g.

Finally the DSC results following aging 550C for all aging times considered in this investigation showed single cooling and heating peaks, Figure 24, as previously observed after aging at lower temperatures, 400 and 450C. The M_s and M_f temperatures after aging for 1 h were 14C and -19C, respectively, with a corresponding enthalpy change of 26.4 J/g, the A_s and A_f temperatures being 17C and 59C, with a corresponding enthalpy change of -25.7 J/g. The M_s and M_f temperatures after aging for 10 h were 14C and -17C, with a corresponding enthalpy change of 30.6 J/g, the A_s and A_f were 13C and 56C respectively, with a corresponding enthalpy change of -31.1 J/g. After a 100 h age the M_s and M_f temperatures were 12C and -23C,

respectively, with corresponding enthalpy change of 23.7 J/g, the A_s and A_f were 12C and 52C, respectively with corresponding enthalpy change of -24.0 J/g.

Multiple Peaks

Multiple peaks were typically observed after aging for longer times at 400 and 450C as well as for all aging times at 500C. The complexity of these reactions required additional partial cycle DSC and x-ray studies. For example, DSC results after aging for 10 h at 400C displayed three peaks on cooling, all of which partially overlapped, as well as two overlapping peaks upon heating, Figure 25. A partial cycle which was designed to separate the this first two peaks observed on cooling, Figure 25b, involved heating to 100C, holding for 3 min, cooling to 25C, reheating to 100C and returning to 25C. Results of this cycle indicate the presence of a corresponding heating peak not found in the other cycles depicted in Figures 25a and 25c.

X-ray diffraction after solution treatment, aging for 10 h at 400C, heating to 100C and cooling to room temperature was thereafter designed to define the transformation observed during this partial cycle. Figure 26 displayed peaks centered at 42.34°, 42.77° and 42.86°. Comparison with expected peak positions associated with B19', R, and B2 indicate that the peak located at 42.34° was associated with the (2-12) R reflection, while that at 42.86° was associated with the (12-1) Ni_4Ti_3 and that at 42.77° with the (110) B2 reflection, the latter having a d spacing slightly different that ST 800, Figure 19. No evidence for B19' was observed. These results indicate that the large peak centered at 43C involved the B2 → R transformation.

a)

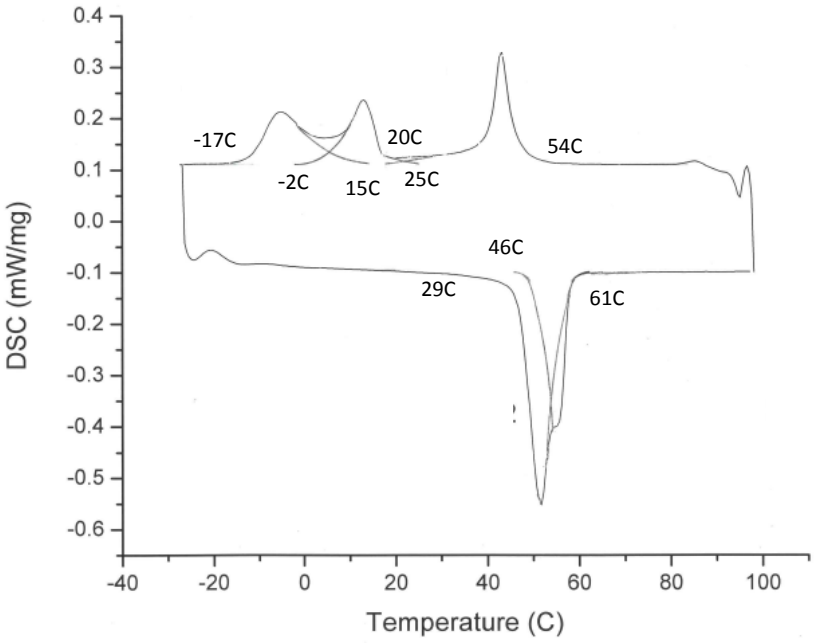
DSC (mW/mg)
Temperature (C)
-17C
-2C
15C
20C
25C
54C
46C
29C
61C
20

b)

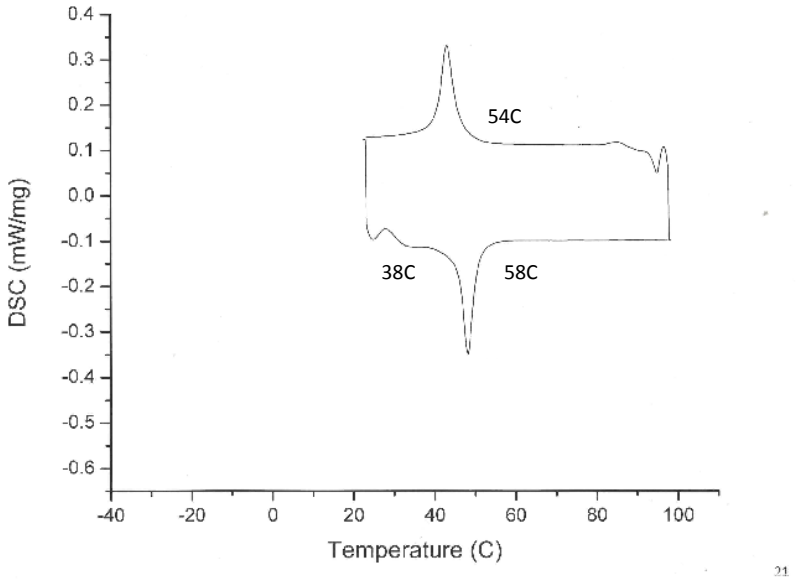
DSC (mW/mg)
Temperature (C)
54C
38C
58C
21

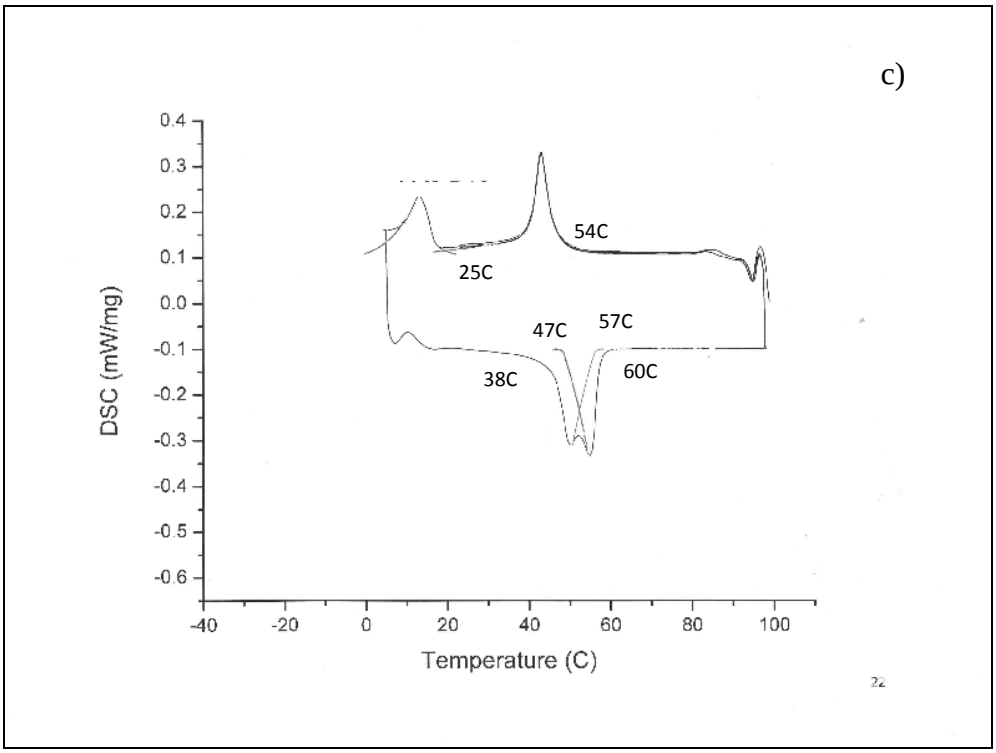

Figure 25: DSC results after solution treatment at 800C for 1 h, ageing at 400C for 10h and water quenching. (a) 25C→100C→-20C→100C→25C cycle; (b) 25C→100C→25C→100C→25C cycle; and (c) 25C→100C→10C→100C→25C cycle

Given the lack of any observable reflections corresponding to the B19' phase for the XRD pattern obtained from the material aged at 400C for 10h and cooled from 100C to 25C, the first peak seen on cooling is indicative of a B2→R transformation with a Rs of 54C, an estimated Rf of 20C and an enthalpy estimated to be 9.3 J/g. The corresponding heating peak seen in Figure 25b is therefore associated with the R→B2 transformation given the lack of any other peak seen in the cycle. Estimated starting and finish temperatures of this heating peak are 38C and 58C, respectively, with a change in enthalpy of -9.1 J/g which nearly matches the enthalpy change seen for the cooling peak.

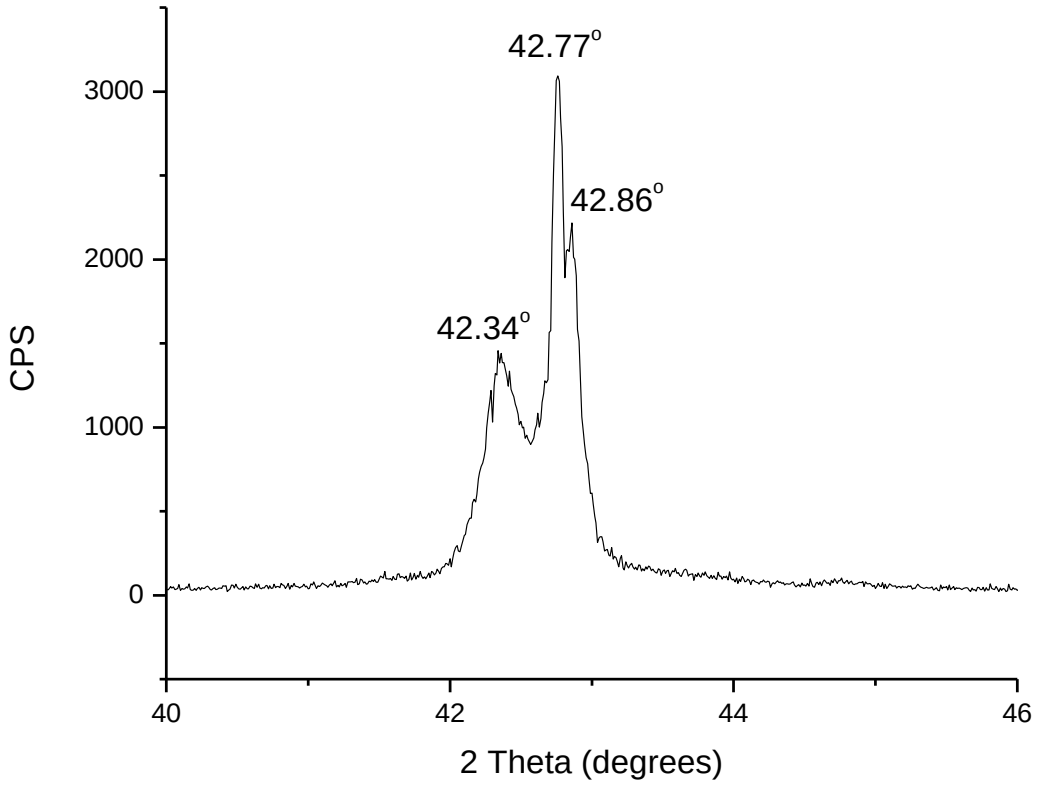

Phase	hkl	Simulated 2theta	Observed 2theta
R	2-12	42.21	42.34
B2 comp 2	110	42.7	42.77
Ni_4Ti_3	12-1	42.97	42.86

Figure 26: X-ray diffraction results for the material solution treated at 800C for 1 h- water quenched, aged at 400C for 10 h, and thermally cycled 25C→100C→ 25C.

Diffraction results, Figure 27, for the 800C solution treated material aged at 400C for 10 h and heated to 25C from -60C contained a number of peaks which are indicative of micro chemical inhomogenities since the peaks found at 38.14°, 39.81°, 41.62°, 45.69°, and 49.29° correspond to reflections of the (110), (101), (11-1), (111), and (021) planes of a B19' phase with a unmodified composition, while peaks located at 39.23°, 43.43°, 44.36°, and 46.88° are due to reflections from (101), (11-1), (020),and (111) planes of a B19' phase with a modified composition whereby the included angle is reduced from 96.8 degrees to 95 degrees. Remaining

peaks located at 40.85° and 42.82° are associated with reflections from the (200) and (12-1) planes of Ni_4Ti_3 precipitates.

Based on the strong presence of multiple B19' phases seen in the diffraction pattern, the second and third cooling peaks seen in the Figures 25a and 25b are associated with B19' transformations. Start and finish temperatures of the peaks are 25C and -2C for the second peak and 15C and -17C for the third peak. Enthalpy changes associated with each peak are estimated to be 10.1J/g and 13.1J/g, respectively. Using the second and final cycles, Figures 25b and 25a, the two overlapped peaks seen on heating can be assigned to the corresponding cooling peaks. Since the first heating peak grows substantially between the cycles, it corresponds to the third cooling peak as this peak is not fully intercepted until the final cycle. The second cooling peak therefore corresponds to the second heating. peak. Using Figure 25a, the respective austenitic start temperatures of the first and second cooling peaks are 28C and 46C. Both peaks display an austenitic finish temperature of 61C. Estimated enthalpy changes of the peaks are -18.9 J/g for the first heating peak and -12.9 J/g for the second. Given that the enthalpy of the first heating peak is roughly equal to the sum of the enthalpy for the B2→R cooling peak and the third cooling peak, this peak corresponds to a B19'→R→B2 transformation and the third cooling peak therefore is associated with a R→B19' transformation. The remaining peaks on cooling and heating correspond to the B2↔B19' transformation which is confirmed given the similarity of their enthalpies.

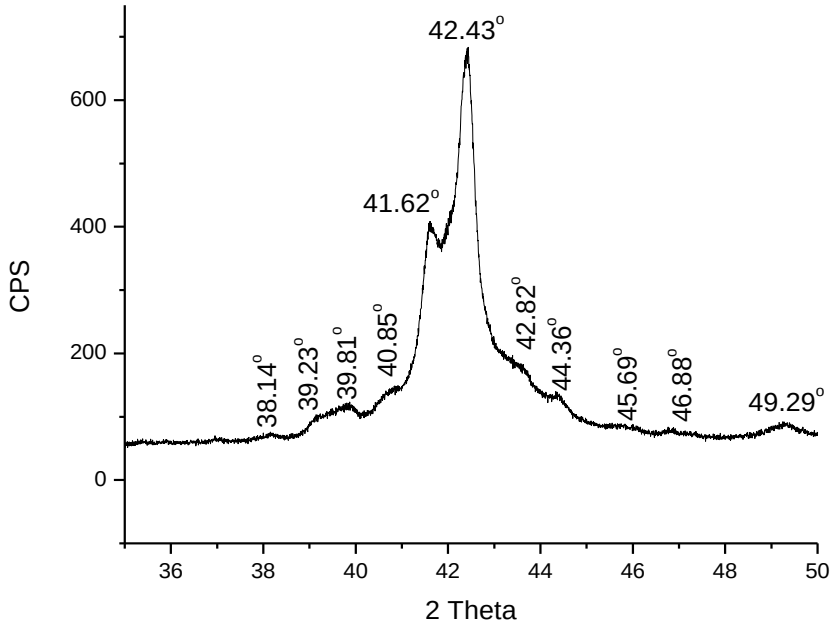

Phase	hkl	Simulated 2theta	Observed 2theta
R	102	36.9	NA
R	3-10	37.5	NA
B19' - 1	110	38.29	38.14
B19' - 2	101	38.94	39.23
B19' - 1	101	38.97	39.81
Ni_4Ti_3	200	39.58	40.85
R	3-11	41.35	NA
B19' - 1	11-1	41.42	41.62
R	2-12	42.21	NA
B19' - 2	11-1	42.54	42.43
Ni_4Ti_3	12-1	42.86	42.82
B19' - 2	020	44.48	44.36
R	202	44.67	NA
B19' - 1	111	45.23	45.69
B19' - 2	111	46.16	46.88
R	301	46.12	NA
B19' - 1	021	48.39	49.29

Figure 27: X-ray diffraction results for material solution treated at 800C for 1 h and water quenched, aged at 400C for 10 h and thermally cycled 25C→ 100C→-60C→ 25C.

Extending the aging time at 400C to 100h did not alter the general characteristics of the DSC results, three peaks on cooling and two peaks on heating being observed, Figure 28.

Cycling the sample between 100C and 40C resulted in a heating peak not seen in the other cycles, Figure 28c. Moreover given the close proximity of this peak with the cooling peak, the peaks correspond to a B2↔R transformation, which is follows the same transformation sequence of the material aged at 400C for 10h. Using figure 28c, the Rs temperature is 58C and the start and finish temperatures of the reverse transformation are 51C and 68C. Using figure 28b, the Rf temperature is estimated to be 37C. Estimates of the enthalpy changes for the peaks are 1.5 J/g for the cooling and 1.4 J/g for the heating peak. Cycling the sample between 25C and 100C captures the first two cooling peaks and second heating peak, indicating a correspondence between these peaks. Since the second cooling peak exhibits a large hysteresis it is due to a B19' transformation. The Ms temperature of the second cooling peak is estimated to be 44C, and the Mf temperature is estimated to be 10C. Estimates of the enthalpy change exhibited by this cooling peak are 7.0J/g. Start and finish temperatures of the heating peak are 49C and 79C, respectively with an enthalpy of -8.2J/g. Because the cycle captures a single heating peak for a R and B19' transformation, the second heating peak is associated with a B19'→R→B2 transformation, which is confirmed by the summation of the enthalpies of the cooling peaks, which are within 0.1J/g of the heating peak. It then follows that the second cooling peak is associated with a R→B19' transformation. Cycling the sample between -20C and 100C, Figure 28a, contains the third cooling peak and the first heating peak which to this point has not appears in any of the other cycles, indicating a correspondence between the third cooling peak and the first heating peak. Moreover, the hysteresis seen between these peaks indicates that these peaks correspond to a B19'↔B2 transformation. The estimated martensite start and temperature for the cooling peak is 20C, and the As and Af temperatures for the heating peak are 16C and 61C,

respectively. Respective enthalpy changes for the cooling and heating peaks are 18.2 J/g and -18.8J/g.

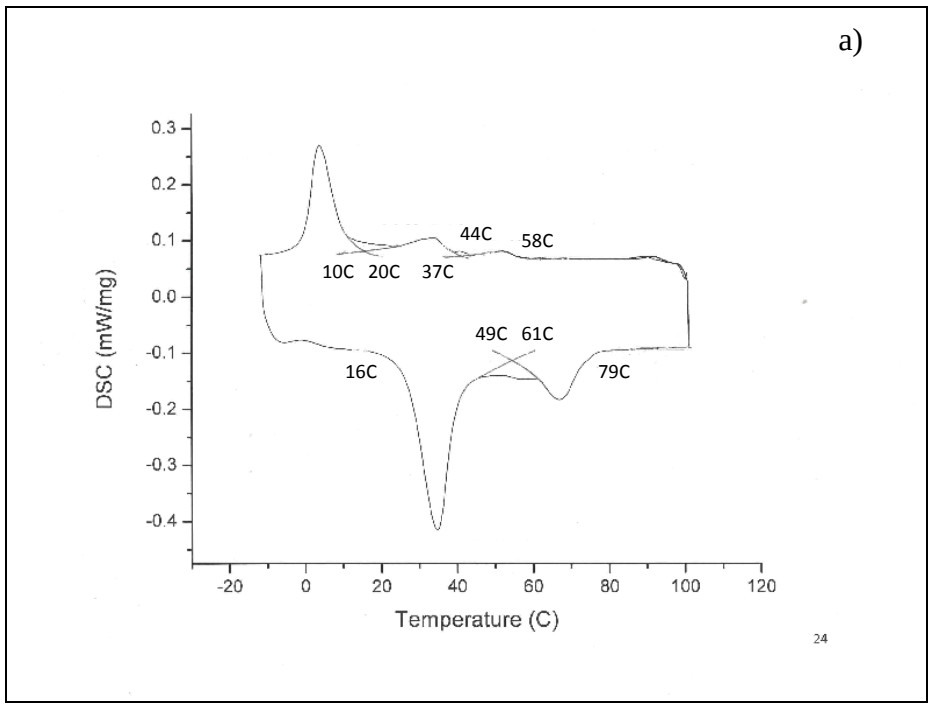

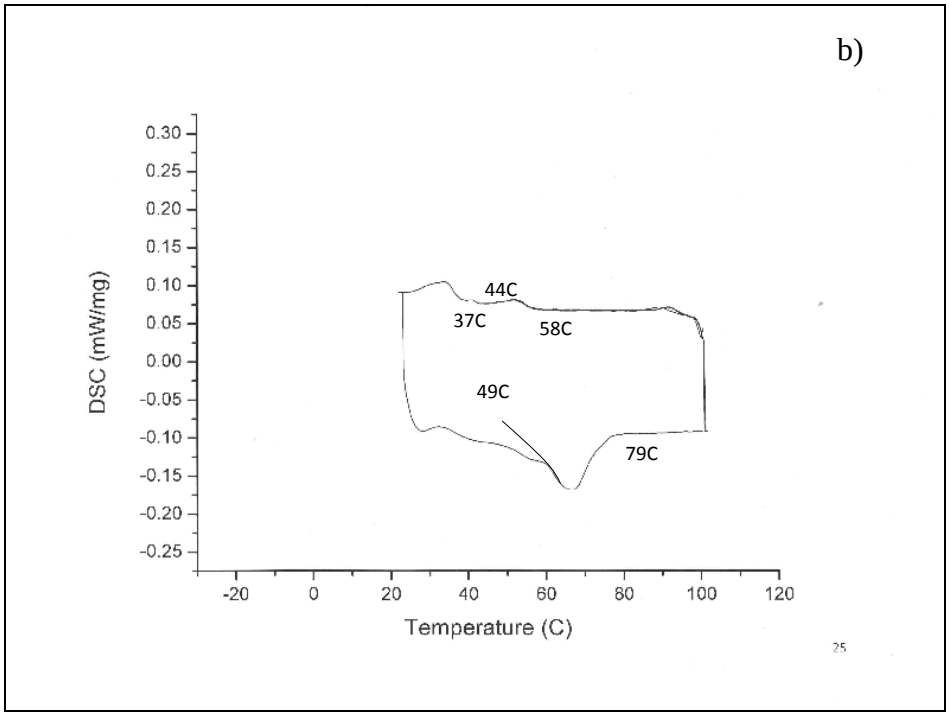

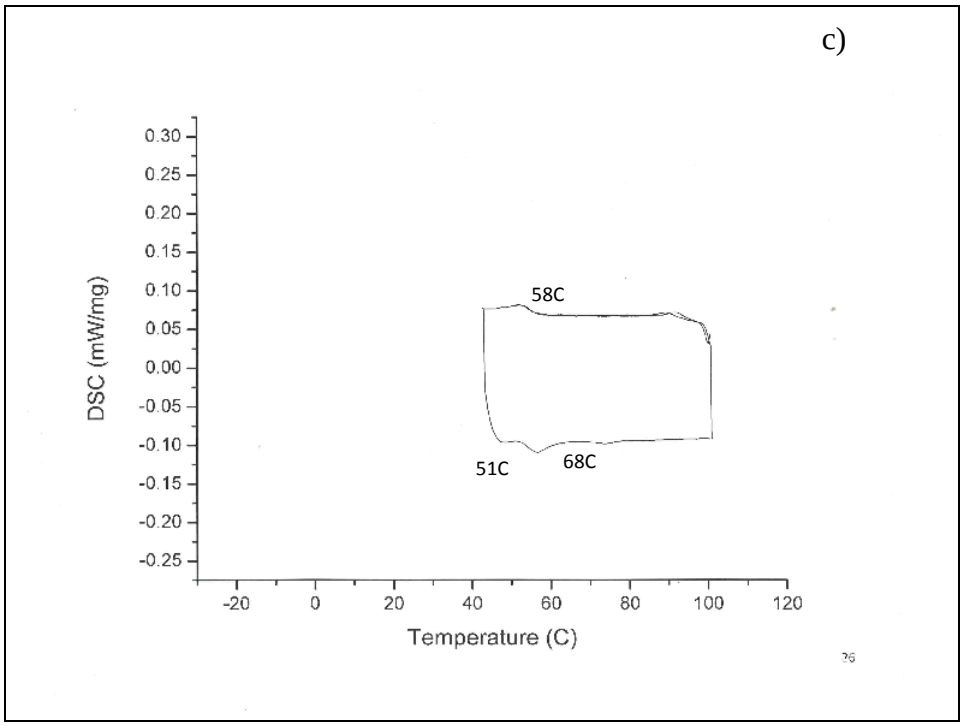

Figure 28: DSC results after solution treatment at 800C for 1 h, ageing at 400C for 100h and water quenching. a) complete cycle; b) 25C→100C→25C→100C→25C cycle; (c) 25C→100C→40C→100C→25C cycle.

The DSC results of material solution treated for 1hr at 800C and aged at 450C for 100h displayed two overlapped peaks on cooling and heating, Figure 29. Deconvolution of these peaks indicated that the martensite start and finish temperatures of the first cooling peak were 41C and 3C, respectively, with a corresponding enthalpy change of 23.7 J/g. The martensitic start and finish temperatures for the 2nd peak observed on cooling were 21C and -14C with an enthalpy change of 22.5 J/g. Similarly the start and finish temperatures associated with the first heating peak were 21C and 58C, respectively with a corresponding enthalpy change of -22.4 J/g, while the start and finish temperatures for the second heating peak were 39C and 84C respectively with a corresponding enthalpy change of -23.1 J/g.

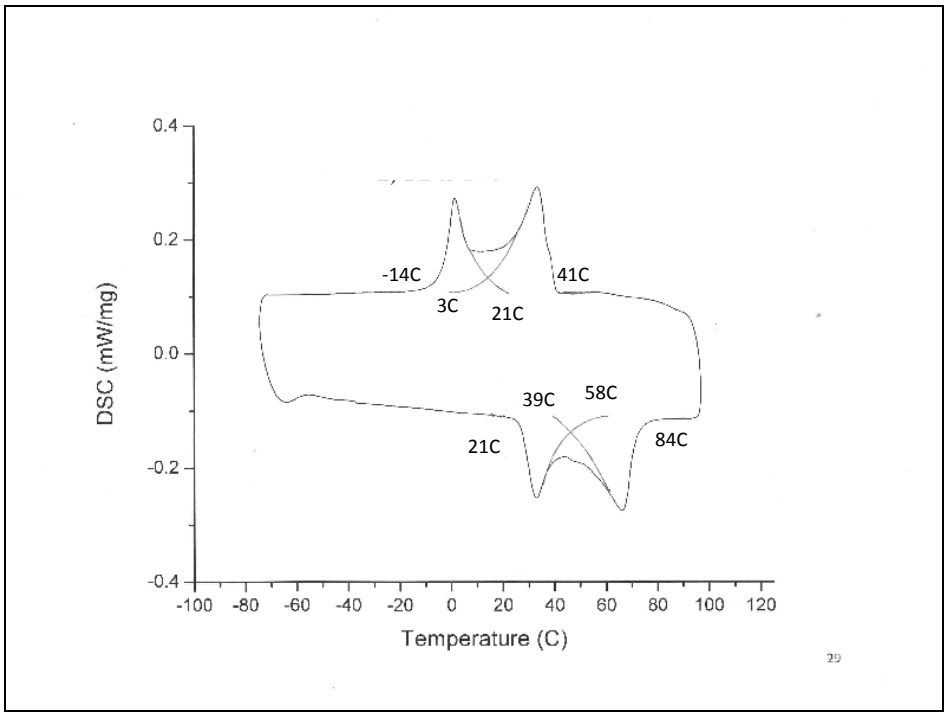

Figure 29: DSC results after solution treatment at 800C for 1h, aging at 450C for 100h and water quenching.

X-ray diffraction results of material solution treated at 800C for 1hr and aged at 450C for 100h after thermal cycling 25C→100C→25C are shown in Figure 30. While complex this pattern can be understood by considering that the microstructure after the aforementioned aging treatment still contained regions of micro chemical inhomogeneity. The peak observed at 40.76° can be associated with (200) Ni_4Ti_3 reflection while that 42.63° can be associated with (110) B2, the latter's composition having been modified by the Ni_4Ti_3 precipitation. The peaks at 39.95° and 46.15° correspond to the (110) and (111) B19' phase reflection with the modified composition. Similarly the remaining peaks found at 38.34°, 39.36°, 41.73°, 43.49°, and 45.09° all are due to the B19'. X-ray diffraction results for the same sample cycled 25C→-60C→25C, Figure 31, yields a similar pattern again indicating the presence of a microstructure containing micro chemical inhomogeneity. The peak found at 40.77° and 42.43° are from the (200) plane of the precipitate and the (110) plane of the B2 phase. Peaks occurring at 39.36° and 46.04°

correspond to the (110) and (111) planes of the B19’ phase with a modified composition while the remaining planes at 38.49°, 41.80°, 43.57°, and 45.08° indicate the presence of the B19’ phase with an unmodified composition.

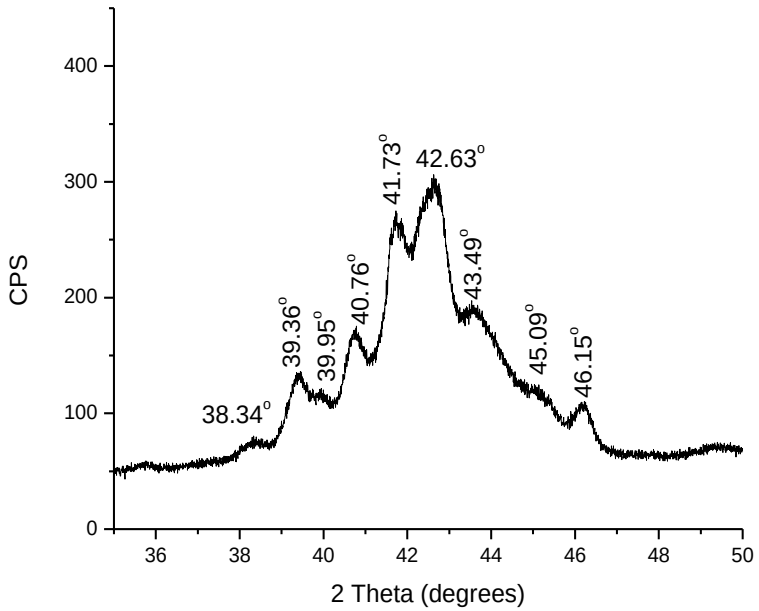

Phase	hkl	Simulated 2theta	Observed 2theta
R	102	36.9	NA
R	3-10	37.5	NA
B19’ - 1	110	38.36	38.34
B19’ - 1	002	39.22	39.36
B19’ - 2	110	39.62	39.95
Ni_4Ti_3	200	39.69	40.76
R	3-11	41.35	NA
B19’ - 2	11-1	41.49	41.73
R	2-12	42.21	NA
B2 - 1	110	42.55	42.63
B19’ - 1	020	44.06	43.49
R	202	44.67	NA
B19’ - 1	111	45.09	45.09
B19’ - 2	111	45.2	46.15

Figure 30: X-ray diffraction results for material solution treated at 800C for 1 h, aged at 450C for 100 h and thermally cycled 25C→100C → 25C.

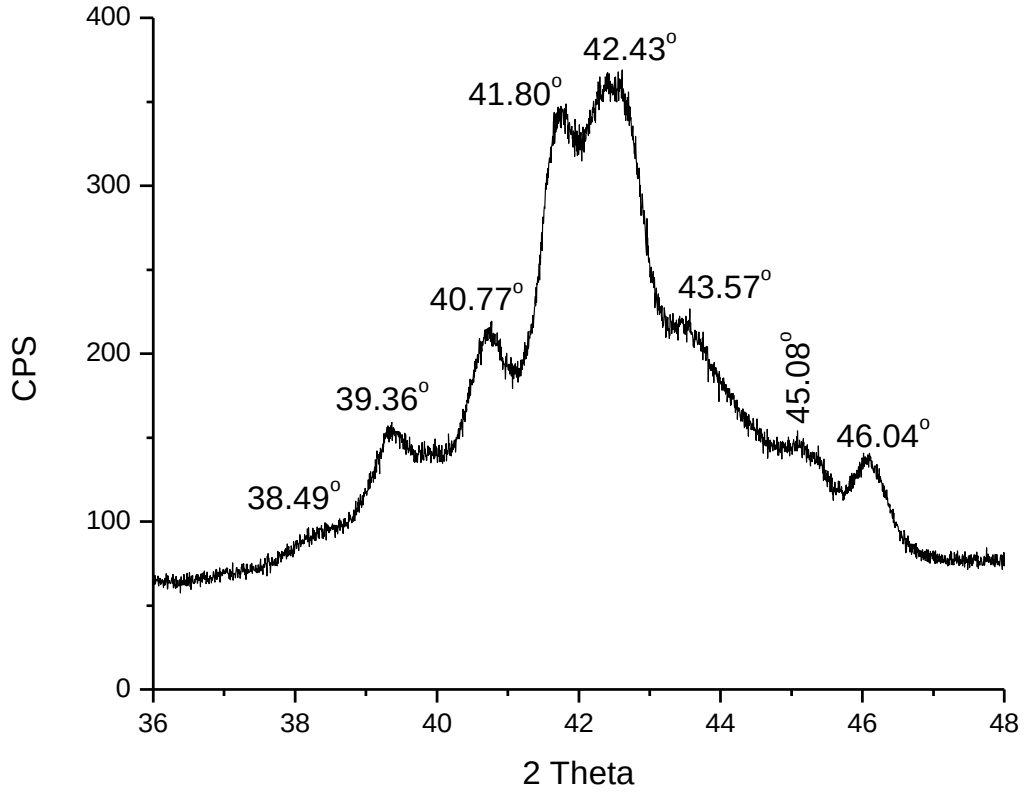

Phase	hkl	Simulated 2theta	Observed 2theta
R	102	36.9	NA
R	3-10	37.5	NA
B19’ comp 1	002	39.22	38.49
B19’ comp 2	110	39.62	39.36
Ni_4Ti_3	200	39.69	40.77
R	3-11	41.35	NA
B19’ comp 1	11-1	41.49	41.80
R	2-12	42.21	NA
B2 comp 1	110	42.55	42.43
B19’ comp 1	020	44.06	43.57
R	202	44.67	NA
B19’ comp 1	111	45.09	45.08
B19’ comp 2	111	45.2	46.04

Figure 31: Figure 29: X-ray diffraction results for material solution treated at 800C for 1 h, aged at 450C for 100 h and thermally cycled 25C→-60C → 25C.

Increasing the aging temperature to 500C again resulted in two overlapping peaks on cooling and heating, Figure 32. The martensite start and finish temperatures for this partially cycled material were estimated to be 28C and 15C, respectively. The definition of the transformations associated with this aging condition was assisted by examination of material that was thermally cycled 25C→100C→15C→100C, Figure 32b. The latter results indicated that the first peak observed on cooling contained a primary transformation with overlap from a low temperature peak, these being separated during the reverse transformation on heating,

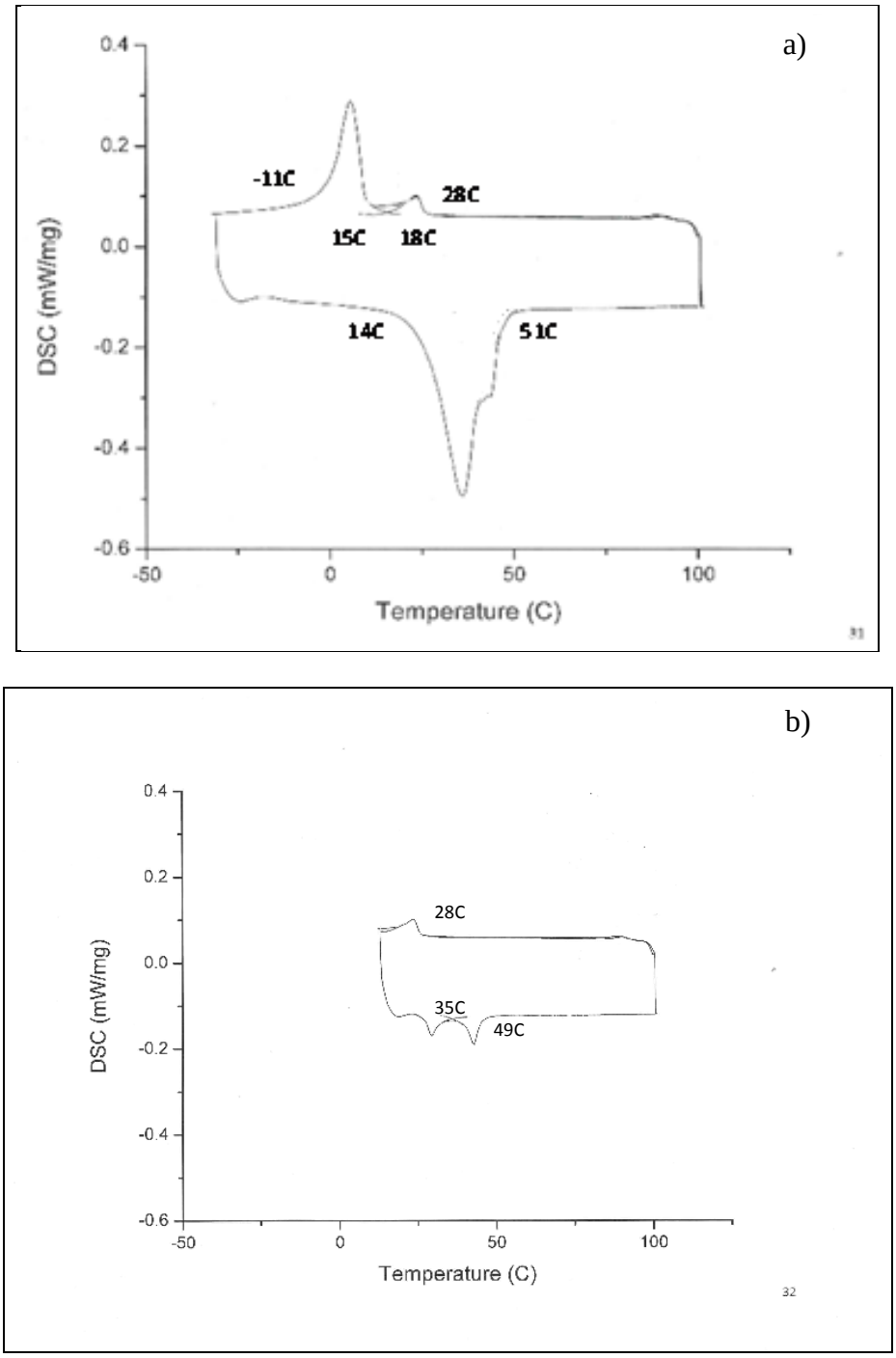

Figure 32: DSC results after solution treated at 800C for 1h, aged at 500C for 1h a) complete cycle, (b) thermal cycle 25C→100C→15C→100C→25C cycle

with a corresponding enthalpy change of 4.4 J/g. Analysis of the heating portion of the partial cycle indicated that the start and finish temperatures of the lower temperature transformation

were 15 C and 35C respectively, the higher temperature peak exhibiting a start and finish temperature of 35C and 49C, respectively, with a corresponding enthalpy change of -4.3 J/g. Combining these results with those obtained complete cycled material indicated that the finish temperature observed on cooling for the lower temperature transformation was -11C, while the start temperature on heating was 14C.

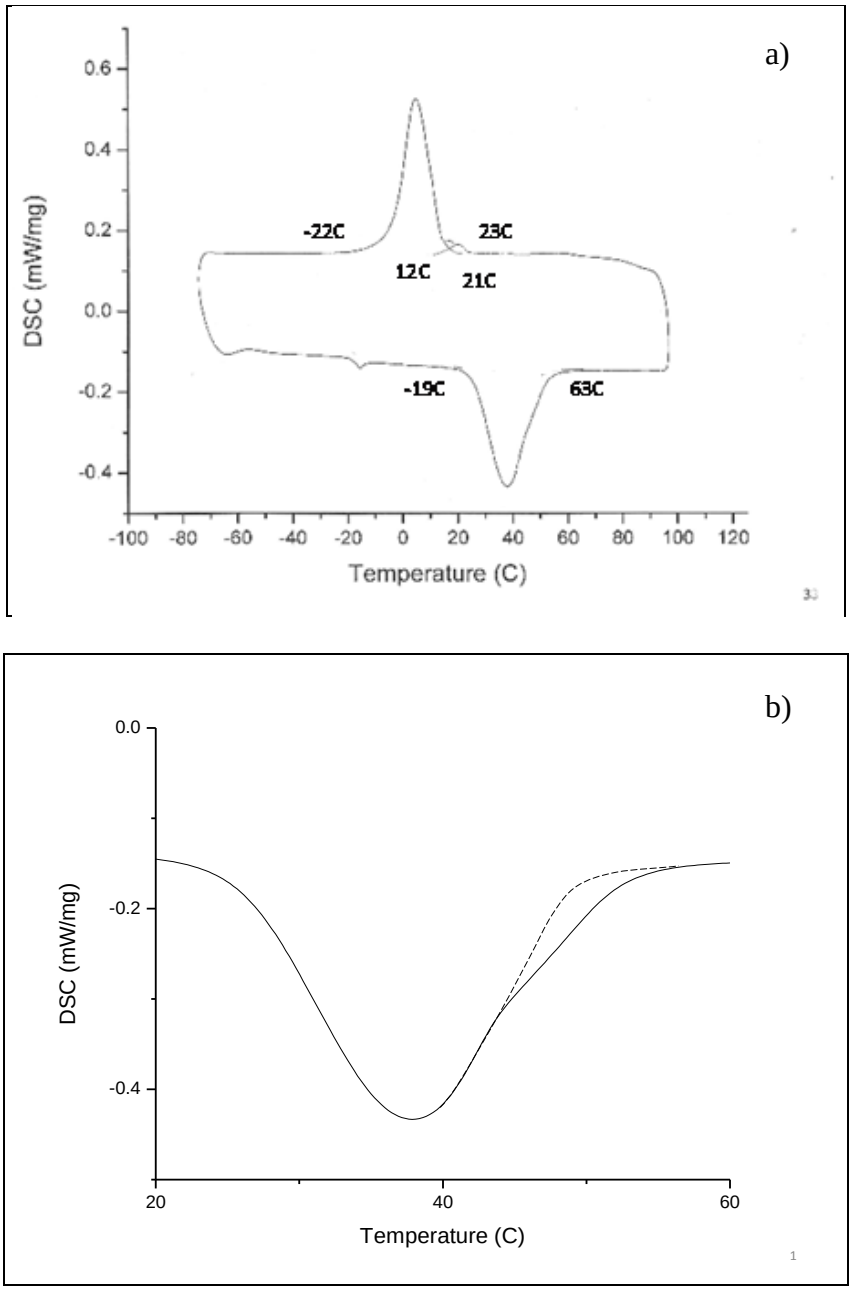

Figure 33: DSC results after solution treatment at 800C for 1h, aged at 500C for 10h: a) entire curve; b) enlarged view of heating peak

DSC results after aging at 500C for 10h showed two overlapped peaks on cooling, Figure 32. The heating portion of the curve contains what appears to be a single peak, however upon closer inspection, Figure 32 b, the peak contains a slight shoulder, suggesting it is composed of two overlapped peaks. The martensitic start and finish temperatures for the first cooling peak were 23C and 12C respectively with a corresponding enthalpy change of 2.35J/g, while the martensite start and finish temperatures for the second cooling peak, were 21C and -22C, with a corresponding change of 31.0 J/g. The start temperature of the heating peaks was 19C, it finished at 63C and displayed an enthalpy change of -32.3 J/g.

Finally the DSC results after aging at 500C for 100h displayed overlapped peaks on heating and cooling, Figure 34. The cooling peak began at 31C and finished at -11C with an enthalpy of 32.6 J/g. The start and finish temperatures for the second cooling peak was 9C and -2C, respectively with an enthalpy change of 2.1 J/g. On heating, the peak started at 26C and ended at 66C with an enthalpy change of -32.4 J/g.

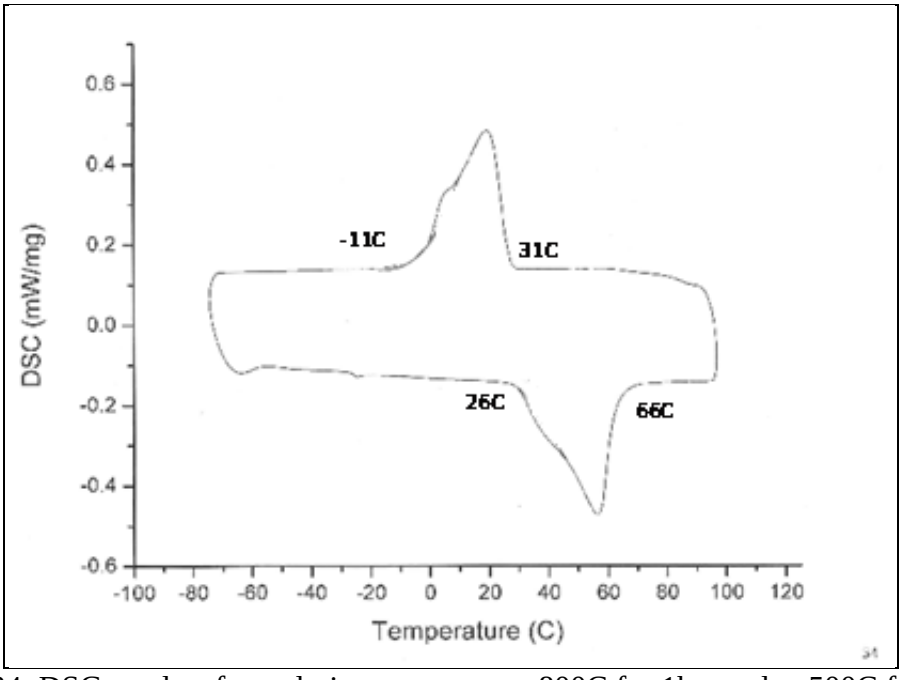

Figure 34: DSC results after solution treatment at 800C for 1h, aged at 500C for 100h.

Severely Deformed

DSC results for the unaged SPD condition exhibited two overlapping peaks on cooling and a single peak on heating, Figure 35. The martensite start and finish temperatures for the first cooling peak were 30C and -19C, respectively, with a corresponding enthalpy change of 8.2 J/g, while the martensite start and finish temperatures for the second peak observed on cooling were

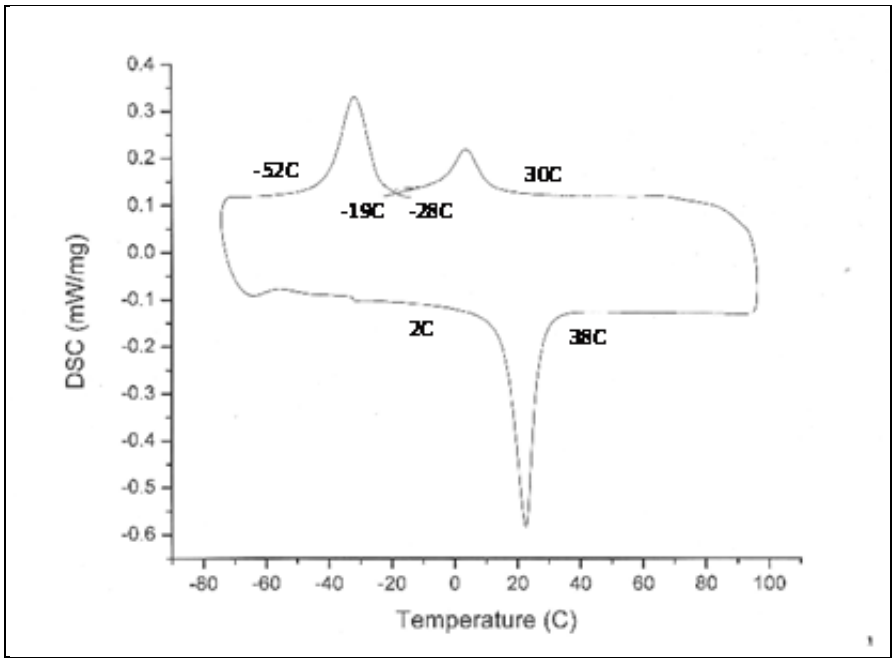

Figure 35: DSC results for unaged SPD.

-28C and -52C respectively, with a corresponding enthalpy change of 14.1 J/g. Finally the start and finish temperatures during heating were 2C and 38C, respectively, with a corresponding enthalpy change of -23.4 J/g.

X-ray diffraction results of the unaged SPD material, Figure 36, exhibited two relatively intense peaks at 42.59° and 42.86° and two very broad and relatively weak peaks at 40.71° and 41.81°. Simulations indicate that the peaks at 40.71° and 42.86° are associated with (200) and (12-1) Ni_4Ti_3 reflections, that at 42.59° with (110) B2 and at 41.81° (3-11) R reflection.

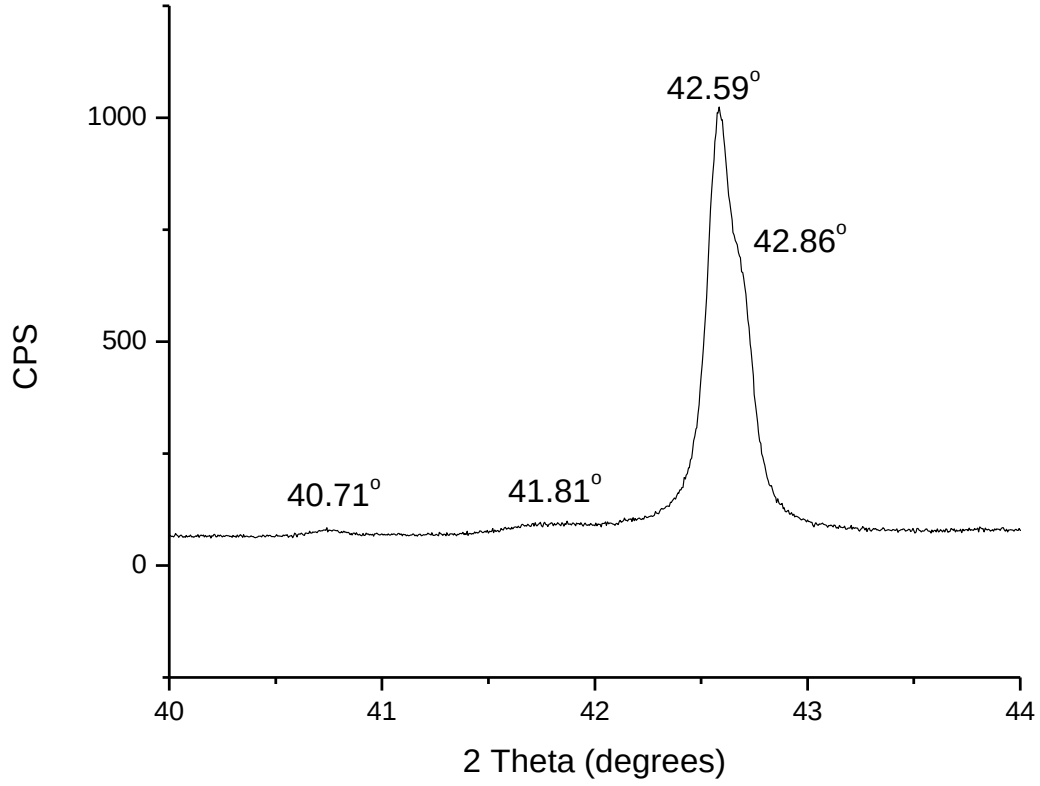

Phase	hkl	Simulated 2theta	Observed 2theta
Ni_4Ti_3	200	39.69	40.71
R	3-11	41.35	41.81
B2	110	42.55	42.59
Ni_4Ti_3	12-1	42.97	42.86

Figure 36: X-ray diffraction results for SPD material thermally cycled from 25C→100C→ 25C.

Severely Deformed and Aged

Multiple Peaks

DSC results for SPD material aged for 1 h 400C displayed two peaks on cooling and a single peak on heating, Figure 37. Deconvolution of the peaks observed on cooling indicated that the martensite start and finish temperatures for the first peak were 50C and -15C, respectively, with a corresponding enthalpy change of 8.7 J/g while martensite start and finish temperatures for the were -10C and -48Cwith a corresponding enthalpy change of 12.7 J/g. On

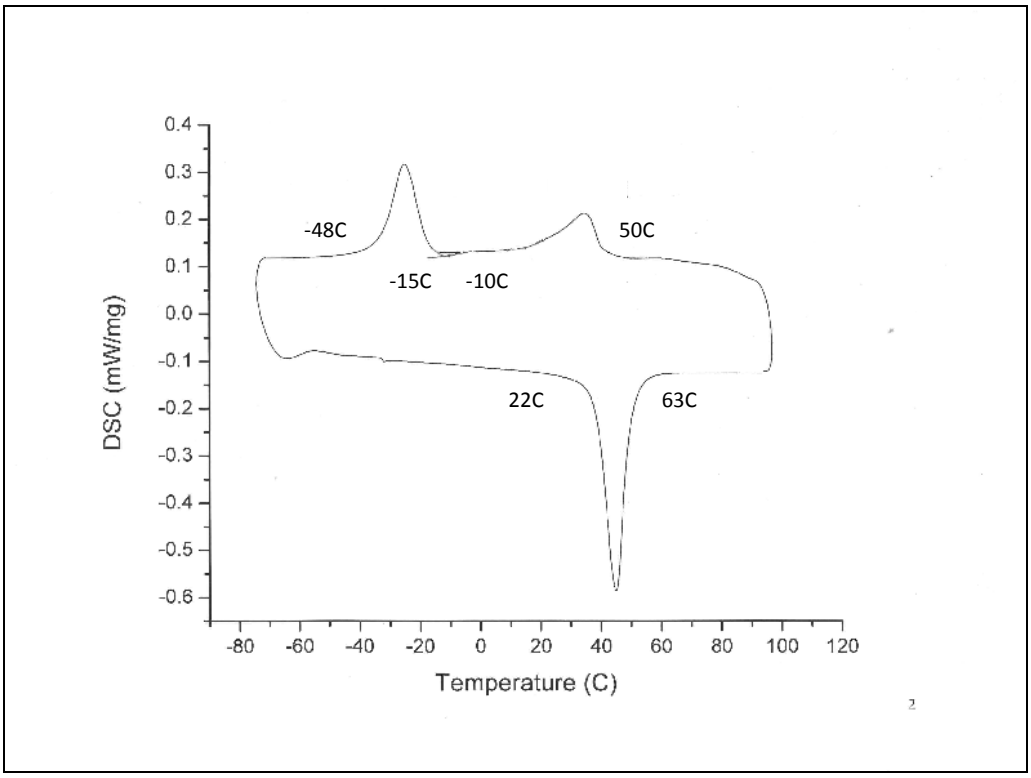

Figure 37: DSC results of the SPD material aged at 400C for 1h.

heating the start and finish temperatures were 22C and 63C, respectively, with a corresponding enthalpy change of -24.4 J/g.

Increasing the aging time at 400C to 10 or 100 h for the SPD material did not have a material effect on the DSC results, two peaks being observed during cooling and one during heating. Further interpretation assistance was moreover provided by cycling the former from 25C→100C→25C→100C→25C, Figure 38. This cycle resulted in a single DSC peak being observed during both cooling and heating. Combining the results from Figure 38 a and b indicate that the martensite start and finish temperatures for the first cooling peak were 55C and 38C, respectively, with a corresponding enthalpy change of 2.8 J/g. The martensitic start and finish temperature for the second cooling peak being 5C and -16C, respectively, with a corresponding enthalpy change of 9.4 J/g. The associated heating peak for the partial cycle had a finish temperature of 62C, with a

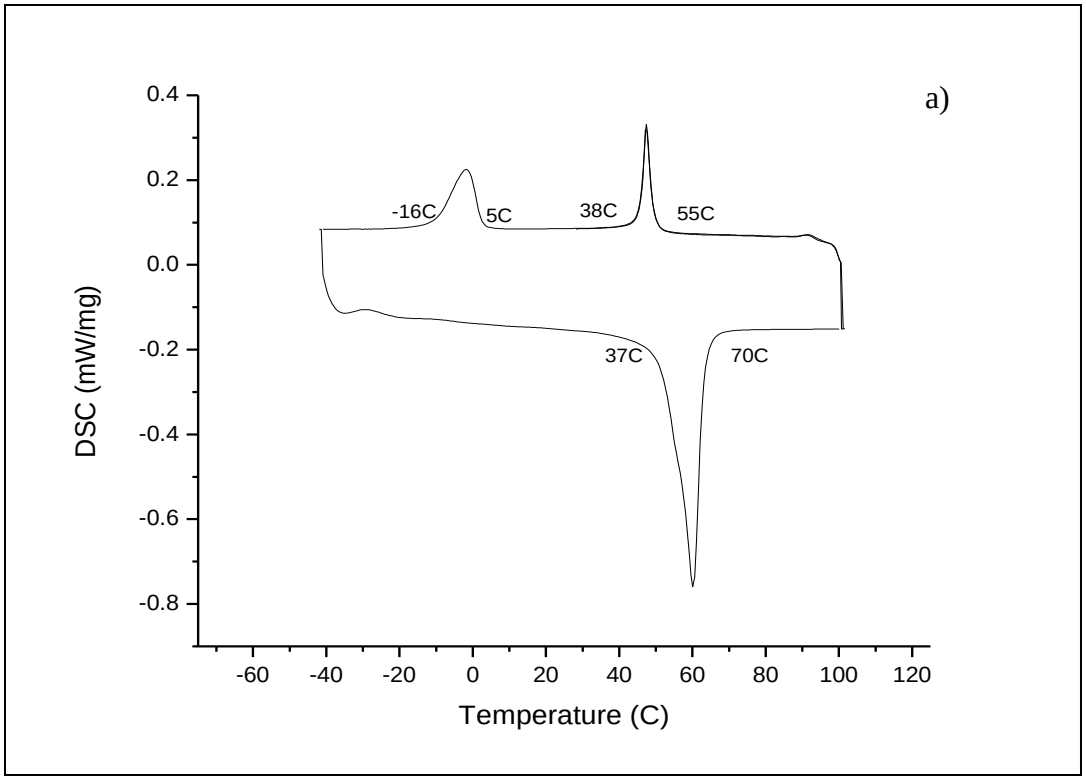

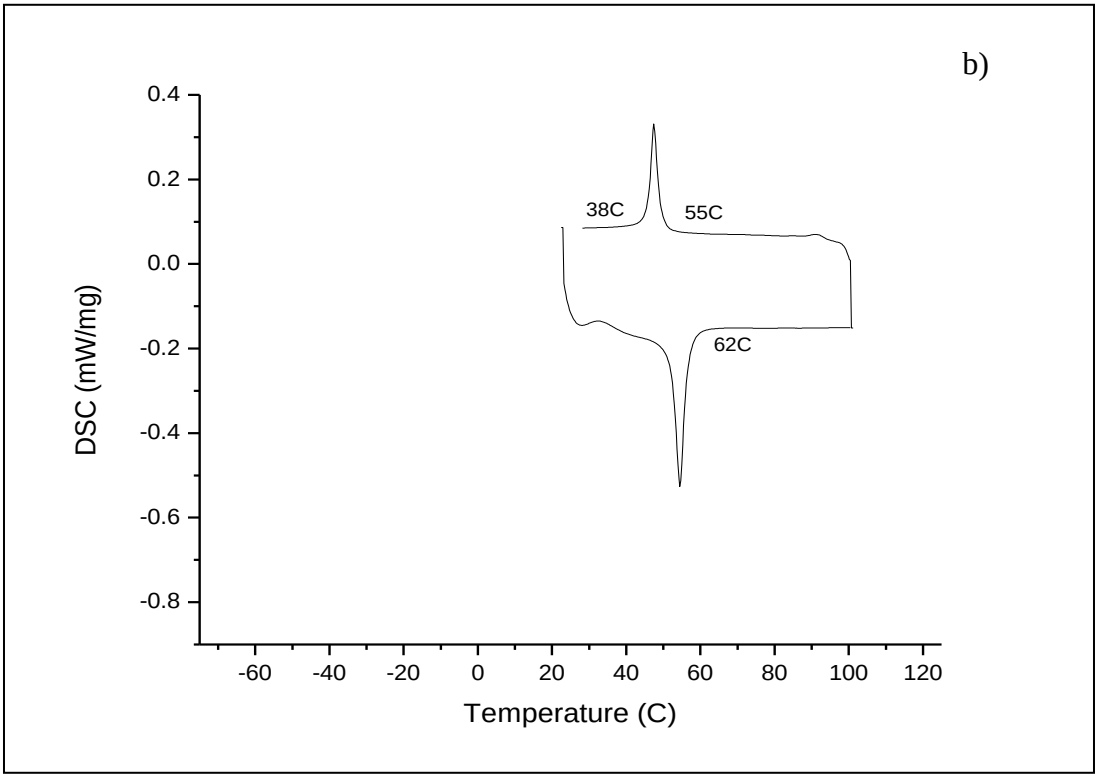

Figure 38: DSC results of the SPD material aged at 400C for 10h; a)complete cycle; b) thermal cycle 25C→100C→20C→100C→25C.

corresponding enthalpy change of -4.1 J/g, the start and finish temperatures for the complete cycle being 37C and 70C, respectively, with a corresponding enthalpy change of -14.1 J/g.

Complimentary x-ray diffraction results for SPD material aged at 400C for 10h heated to 95C and cooled to 25C, Figure 38, indicated the presence of R, and Ni_4Ti_3 peaks observed at 37.06°, 38.37°, 42.33°, 41.58°, 44.81°, and 45.35° corresponding to (102), (3-10), (3-11), (2-12), (202) and (301) R reflections; those at 39.4° and 42.84° to(200) and (12-1) Ni_4Ti_3.

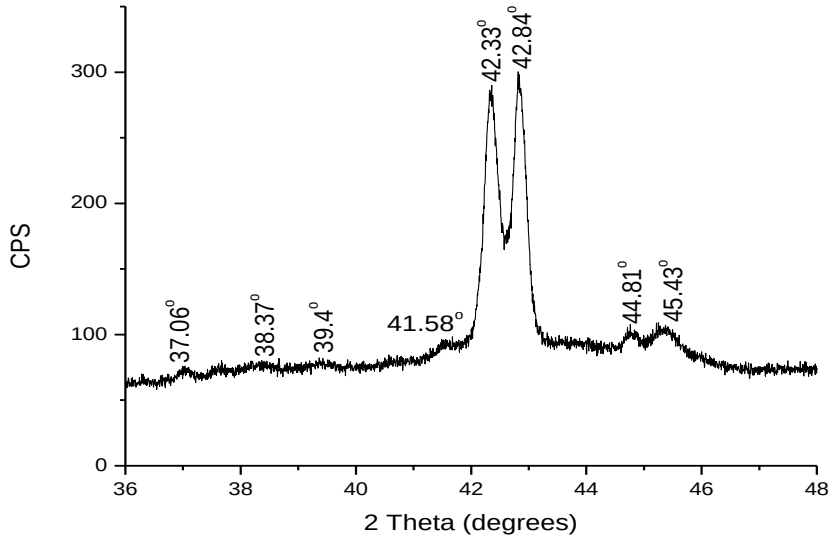

Phase	hkl	Simulated 2theta	Observed 2theta
R	102	36.9	37.06
R	3-10	37.5	38.37
Ni_4Ti_3	200	39.69	39.4
R	3-11	41.35	41.58
R	2-12	42.21	42.33
Ni_4Ti_3	12-1	42.97	42.84
R	202	44.67	44.81
R	301	46.24	45.43

Figure 39: X-ray diffraction results for SPD material aged at 400C for 10h and thermally cycled 25C→ 100C → 25C.

Figure 40 shows the x-ray diffraction results for the same condition thermally cycled from 25C→100C→-60C→25C, Ni_4Ti_3 and B19' being observed. Peaks at 35.65°, 40.75°, 42.34°, and 42.76° correspond (101), (200), (3-2-1), and (12-2) Ni_4Ti_3 reflections while those at 38.43°, 39.52°, 41.71°, 43.92°, and 45.32° arise from (110), (101), (11-1), (020), and (012) B19' reflections.

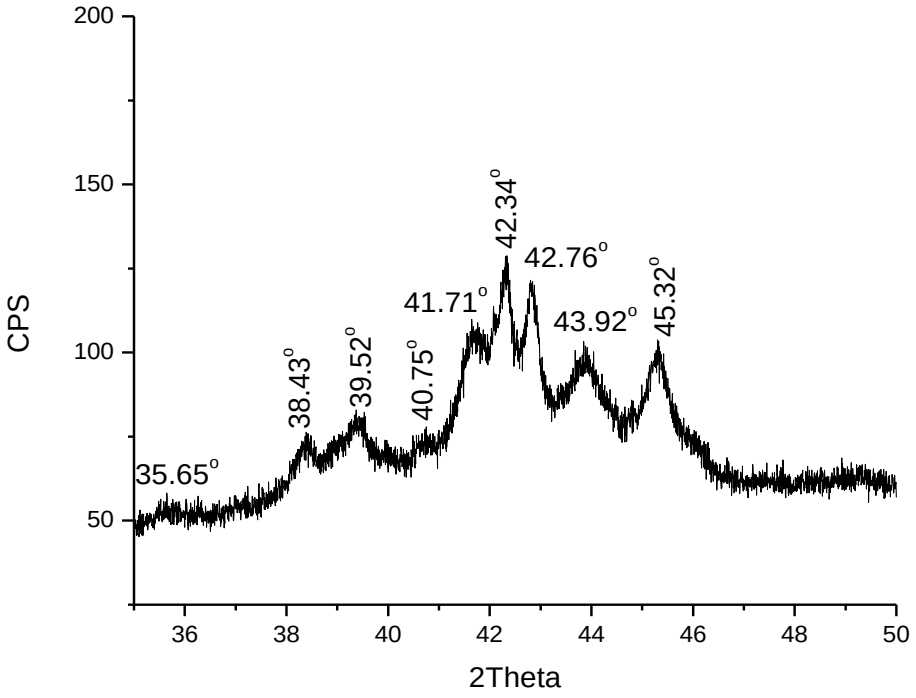

Phase	hkl	Simulated 2theta	Observed 2theta
Ni_4Ti_3	101	36.07	35.65
B19' - 1	110	38.36	38.43
B19' - 1	101	39.07	39.52
Ni_4Ti_3	200	39.69	40.75
B19' - 1	11-1	41.49	41.71
Ni_4Ti_3	3-2-1	42.54	42.34
Ni_4Ti_3	12-1	42.97	42.76
B19' - 1	020	44.06	43.92
B19' - 1	012	45.31	45.32

Figure 40: X-ray diffraction results for SPD material aged at 400C for 10h and thermally cycled from 25C→100C→-60C→ 25C

Similar DSC results were also observed after aging SPD material for 100 h at 400C, Figure 41. The martensite start and finish temperatures for the first cooling peak were 53C and 9C, respectively with a corresponding enthalpy change of 7.7 J/g, the second cooling peak start and finish temperatures being 23C and -8C, respectively, with a corresponding enthalpy change of 14.2 J/g. Upon heating the start and finish temperatures were 42C and 80C, respectively, with a corresponding enthalpy change of -23.6 J/g.

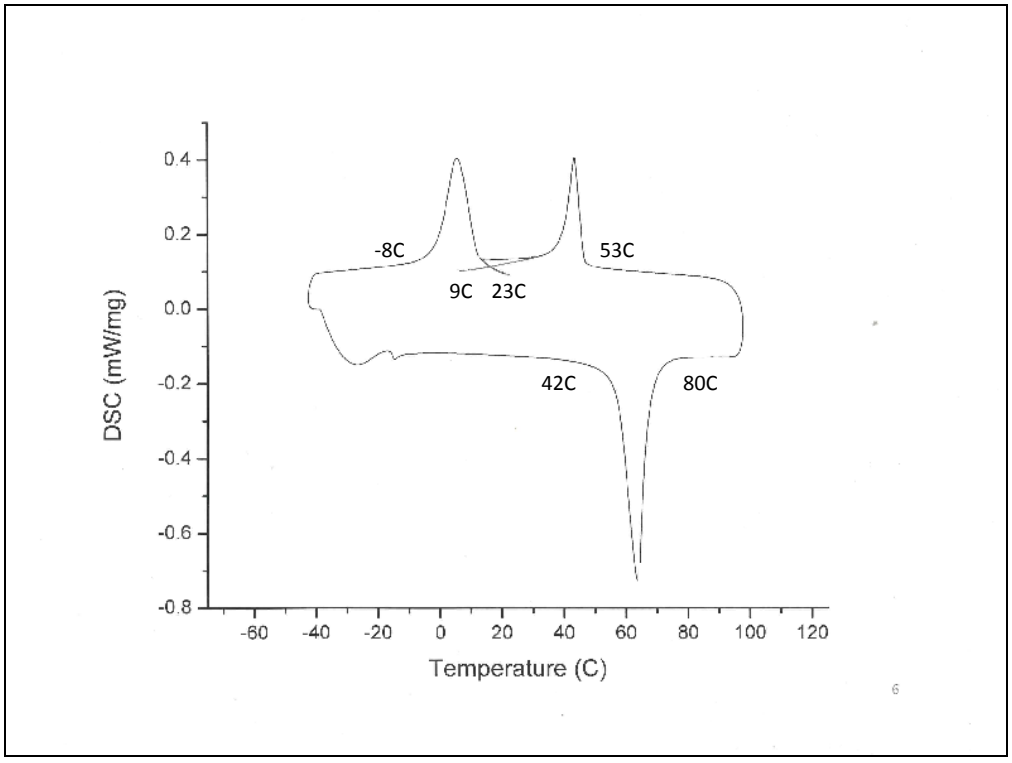

Figure 41: DSC results of SPD material aged at 400C for 100h.

The DSC results observed after increasing the aging temperature the ECAP material for 450C for 1, 10, 100h continued to exhibited two cooling peaks and a single heating peak. Figure 42 shows that the martensite start and finish temperatures for the first cooling peak after aging 1 h at 450C were 39C and -13C, respectively, with a corresponding enthalpy change of 7.1 J/g, the second peak on cooling having a martensite start and finish temperature of -2C and -38C

with a corresponding enthalpy change of 10.4 J/g. Finally start and finish temperatures on heating peak were 23C and 60C, respectively, with a corresponding enthalpy change of -18.9 J/g.

After aging for 10h the martensite start temperature for the first peak observed on cooling appeared to be unaffected, 40C, while the finish temperature increased to -1C, with a corresponding enthalpy change of 8.2 J/g, Figure 43. Examination of the second peak observed on cooling showed that the martensite start and finish temperatures increased to 9C and -21C,

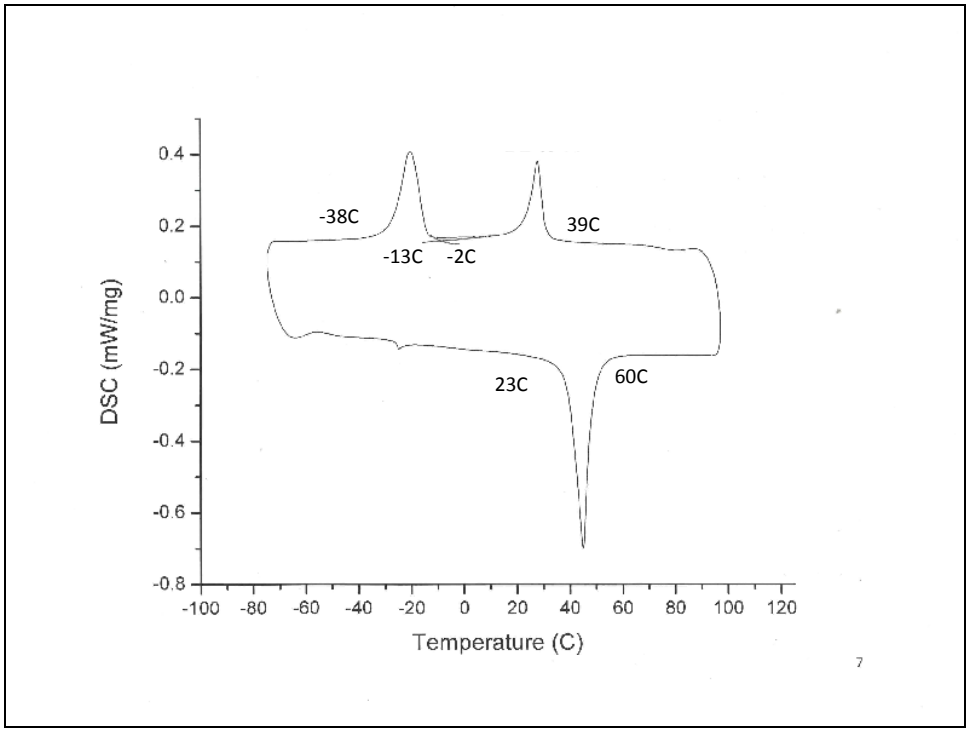

Figure 42: DSC results of SPD material aged at 450C for 1h.

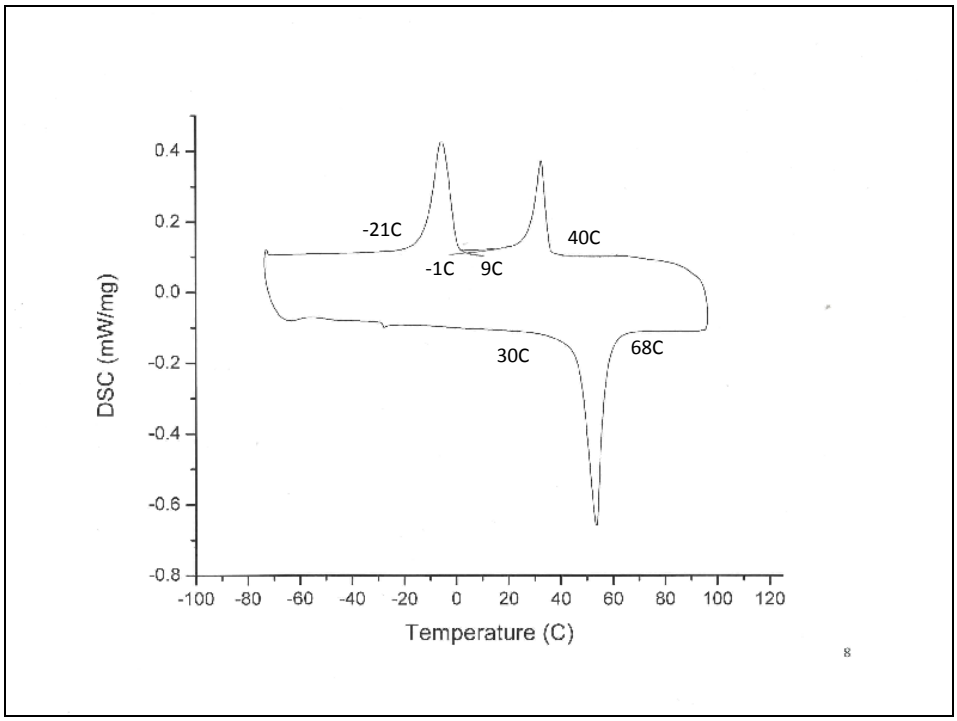

Figure 43: DSC results of SPD material aged at 450C for 10h.

with a corresponding enthalpy change of 14.0 J/g. Increased aging time to 10 h at 450C increased the start and finish temperature for the reaction peak observed on heating to, 30C and 68C, respectively, with a corresponding enthalpy change, -23.4 J/g.

Finally the martensite start of the first peak observed on cooling after a 100 h at 450C showed a slight increase to 44C, while the finish temperature increased dramatically to 38C, with a corresponding 8.2 J/g, Figure 44. The martensite start and finish temperatures increased dramatically for the second cooling peak being 28C and 9C, respectively with a corresponding enthalpy change of 13.3 J/g. The start and finish temperatures on heating for the complete cycle were 40C and 77C, respectively, with a corresponding enthalpy change of -23.4 J/g. A second partial thermal cycle, 25C→100C→25C was also examined for this aged condition, Figure 44b. The cooling results were identical to those obtained for the complete cycle, as was the start temperature for the reaction observed on heating. However the finish temperature and the

corresponding enthalpy change, 58C and 8.6 J/g were reduced when compared to the results of the complete cycle.

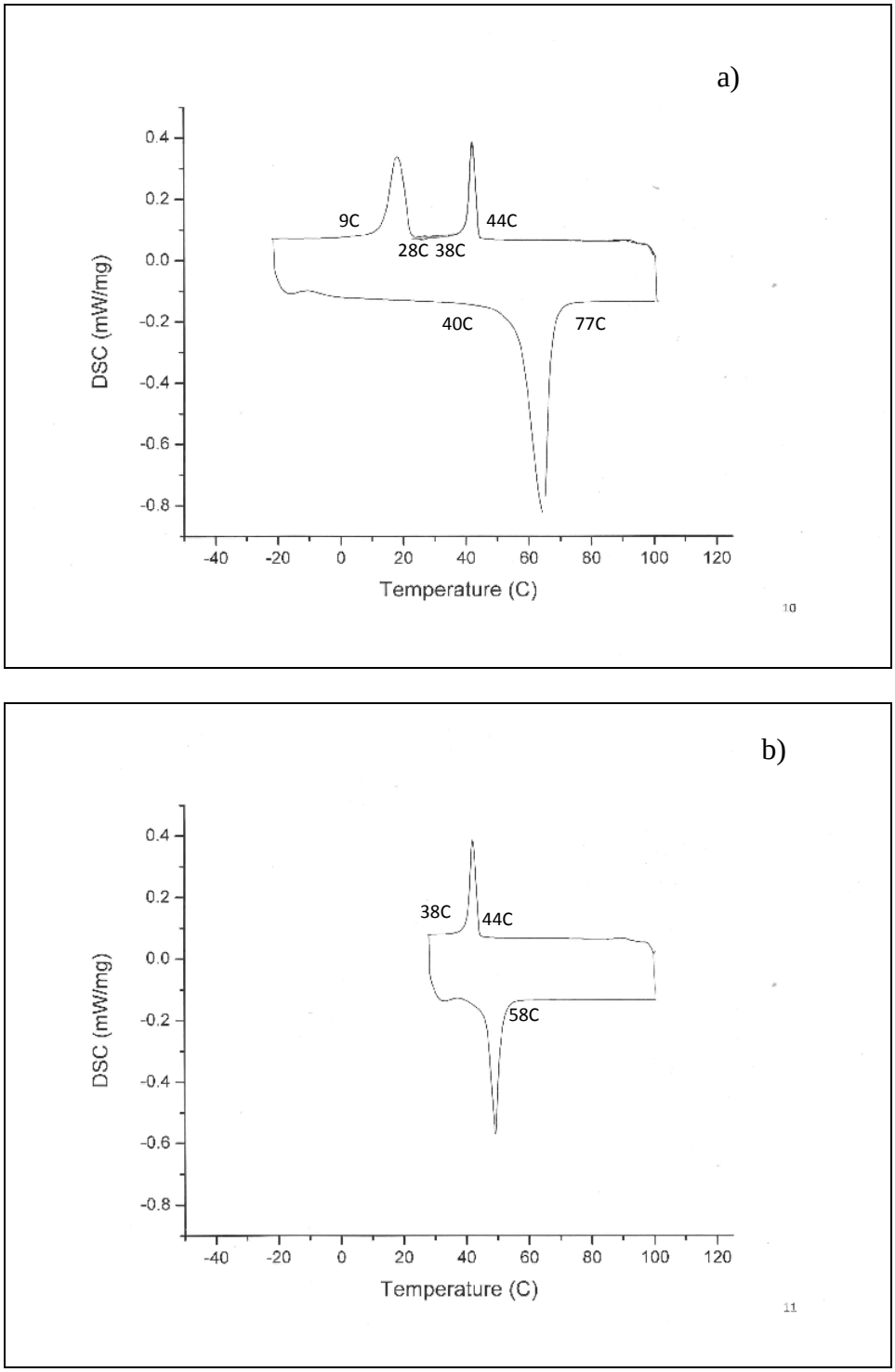

Figure 44: DSC results of SPD material aged at 450C for 100h: a) comple cycle; b) thermal cycle 25C→100C→30C→100C→25C.

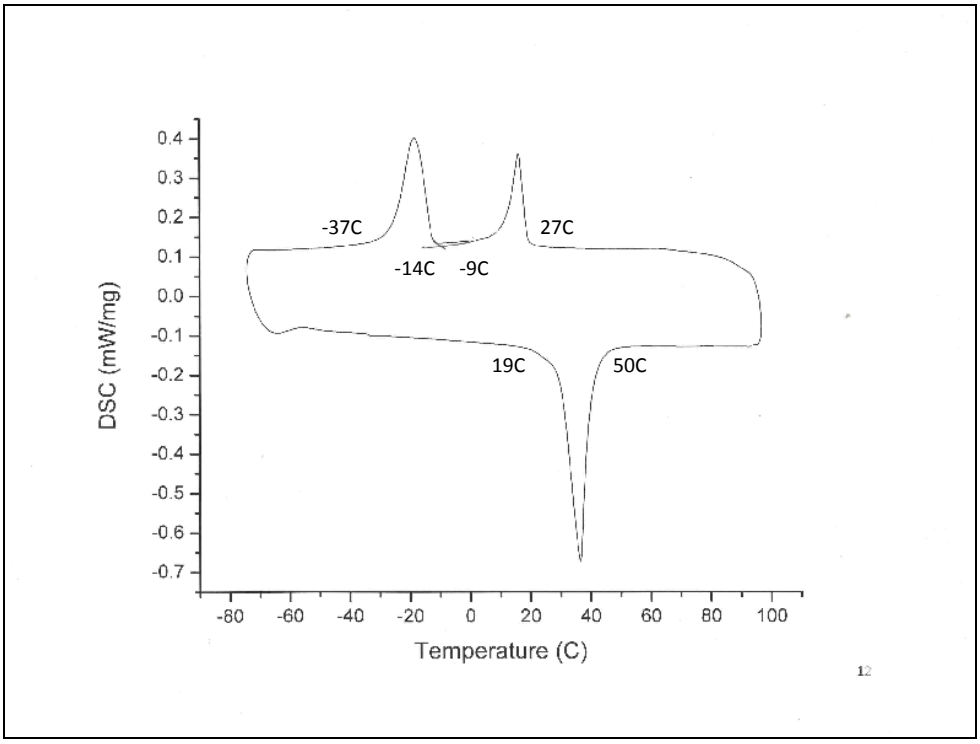

Figure 45: DSC results of SPD material aged at 500C for 1h.

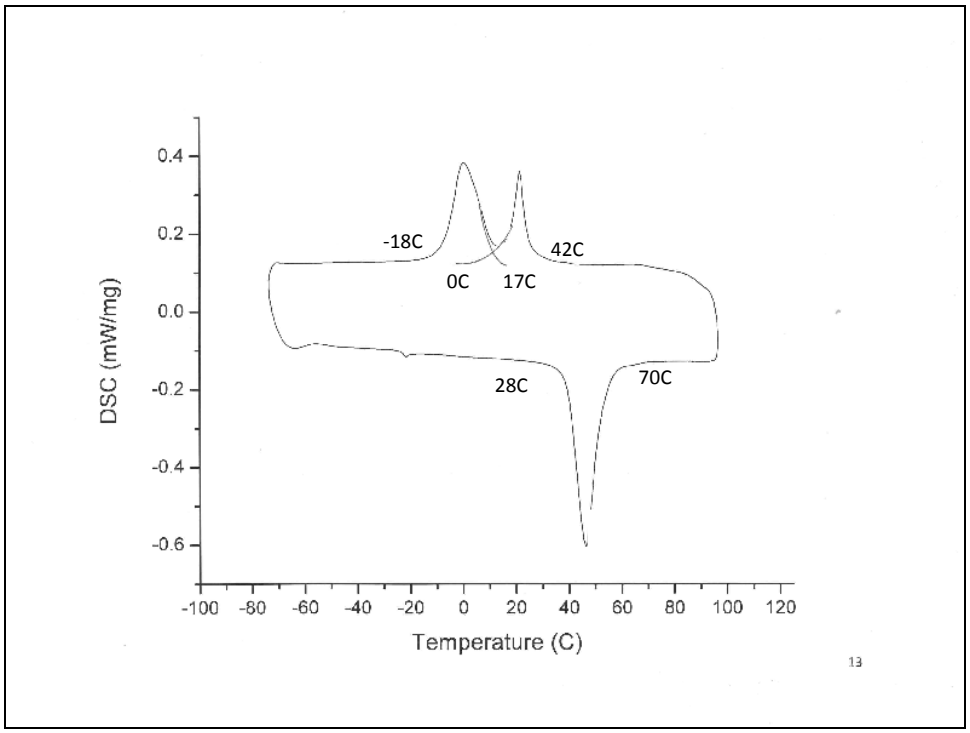

Figure 46: DSC results of SPD material aged at 500C for 10h.

SPD material aged at 500C for 1 and 10 h also displayed two peaks on cooling and a single peak on heating, Figures 45 and 46. After a 1 h age the martensite start and finish temperatures were 27C and -14C, substantially lower than observed after 450C- 1 h age, with corresponding enthalpy change, 8.4 J/g. Martensite start and finish temperatures for the second cooling peak were of -9C and -37C, the former decreasing when compared to aging at 450C, with a corresponding enthalpy change of 14.7 J/g. Similarly start and finish temperature on heating peak were 19C and 50C, somewhat lower than after 450C-1 h treatment with a corresponding enthalpy change of -27.2 J/g.

Increased aging at 500C for 10 h lead to an increase in the martensite start and finish temperatures for both those observed after a 1 h age reaction observed on cooling being 42C and 0 C respectively for the first reaction and 17C/-18C for the second reaction occurring on cooling, Figure 45. The enthalpy changes observed for each of the reaction, 5.5 J/g and 14.3 J/g were similar to those observed after the 1 h age. Additionally the start and finish temperatures on heating, 28C and 70 C respectively, were also higher than after 1 h. Finally the enthalpy change associated with reverse heating reaction, -25.1 J/g was similar to that observed after the 1 h age.

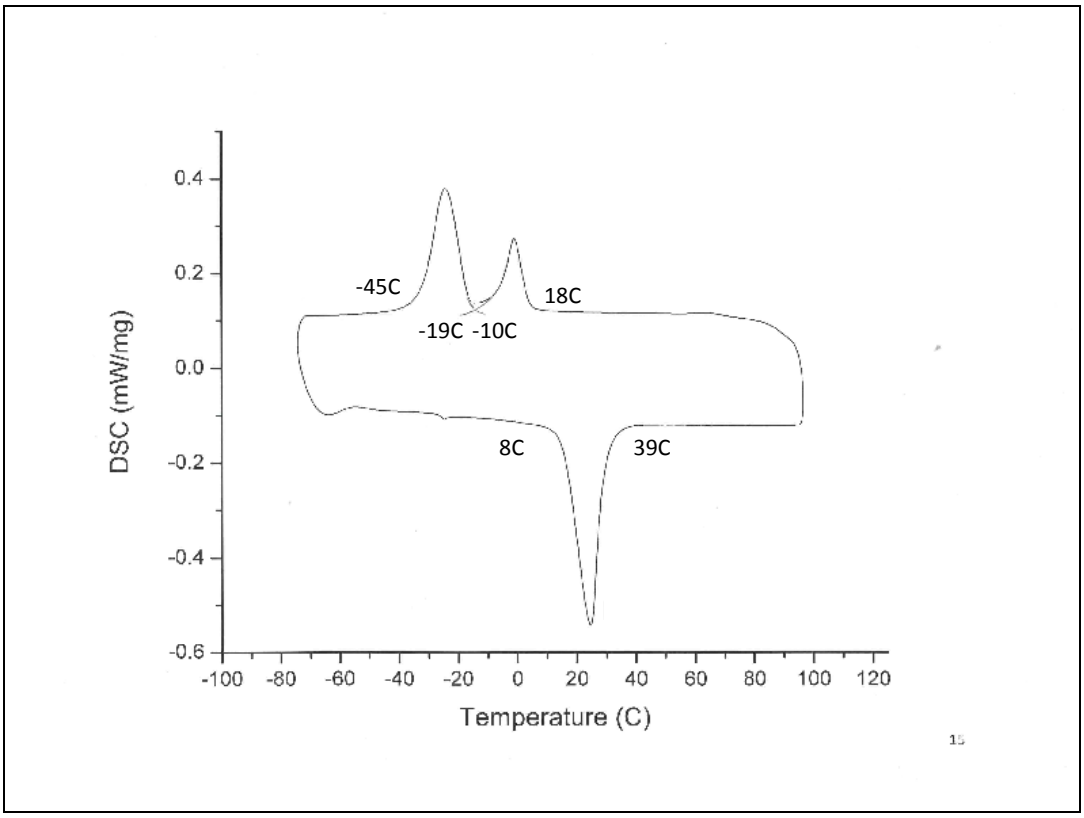

Figure 47: DSC results of SPD material aged at 550C for 1h.

Multiple peaks were also observed after short time, 1 h, aging at 550C, Figure 47. The martensite start and finish temperatures for the first reaction on cooling, 18C and -19C were lower than after aging at 500C for 1 h although the corresponding enthalpy change, 4.75 J/g, was similar, while the martensite start and finish temperatures for the second reaction, -10C and -45C were somewhat lower when compared to 500C-1h results, as was the enthalpy change, 11.9 J/g. Moreover the start and finish temperatures on heating, 19C and 50C respectively, as well as the corresponding enthalpy change, -19 J/g were lower than after 500C treatment.

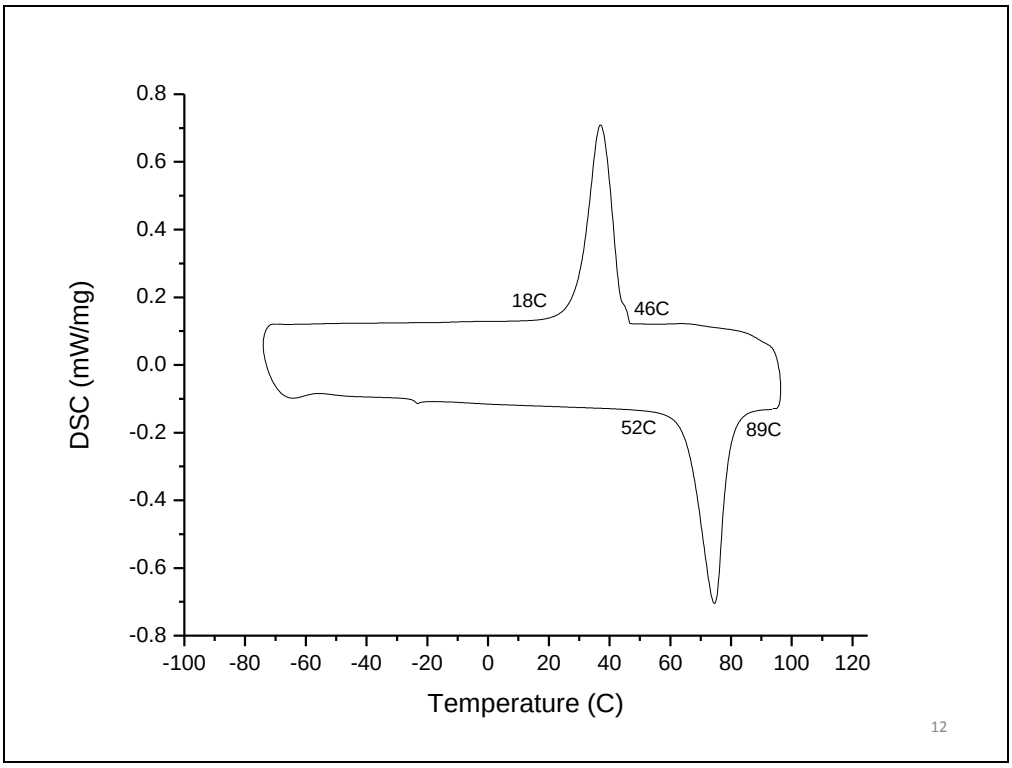

Figure 48: DSC results of SPD material aged at 500C for 100h.

Single Peak

Single transformation peaks both on cooling and heating were observed under long time, high temperature aging condition, i.e., 500C-100 h and 550C-10 and 100 h. The martensite start and finish temperatures for 500C- 100h condition during cooling, Figure 48, were 46C and 18C respectively, with a corresponding enthalpy change of 31.6 J/g. The latter was similar to that observed on the reverse heating transformation, -30.6 J/g, with start and finish temperatures of 52C and 89C, respectively.

X-ray diffraction analysis of SPD material aged for 100 hr and 500C after thermal cycling 25C→100C→25C, Figure 49, indicated the presence of B2, B19,' Ni_4Ti_3,and Ni_3Ti, with peaks located at 36.19° and 41.22° corresponding to (101) and (200) the Ni_4Ti_3 precipitate

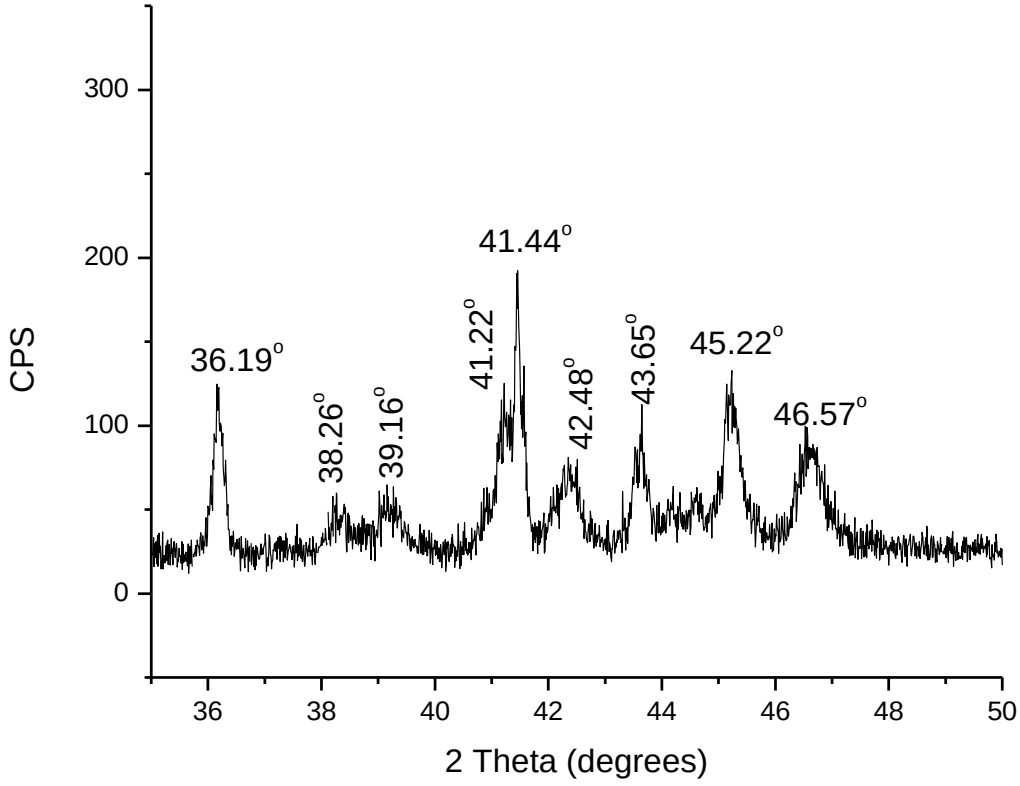

Phase	hkl	Simulated 2theta	Observed 2theta
Ni_4Ti_3	101	36.17	36.19
B19' - 1	110	38.36	38.26
B19' - 1	101	39.22	39.16
Ni_4Ti_3	200	39.69	41.22
B19' - 1	11-1	41.49	41.44
B19' - 1	110	42.55	42.48
B19' - 1	020	44.06	44.52
B19' - 1	111	45.09	45.22
Ni_3Ti	202	46.53	46.57

Figure 49: X-ray diffraction results for SPD materials aged at 500C for 100h and thermally cycled 25C→100C→25C.

reflections, those 42.48° being correspond to a (110) B2 reflection, the peak at 46.57 corresponds to a (202) Ni_3Ti reflection, while the remaining peaks at 38.26°, 39.16°, 41.44°, 44.52°, and 45.22° corresponded to B19' reflections.

Analysis of x-ray diffraction results after further cycling of this material to -60C and returning to 25C are shown in Figure 50. Only peaks corresponding to B19', Ni_4Ti_3, and $TiNi_3$ reflections were observed. The peaks located at 36.24° and 42.38° correspond to the (101) and (1-12) Ni_4Ti_3 precipitate reflections while the peak found at 46.6° corresponds to the (202) reflection of Ni_3Ti, with the remaining peaks correspond to B19' reflections.

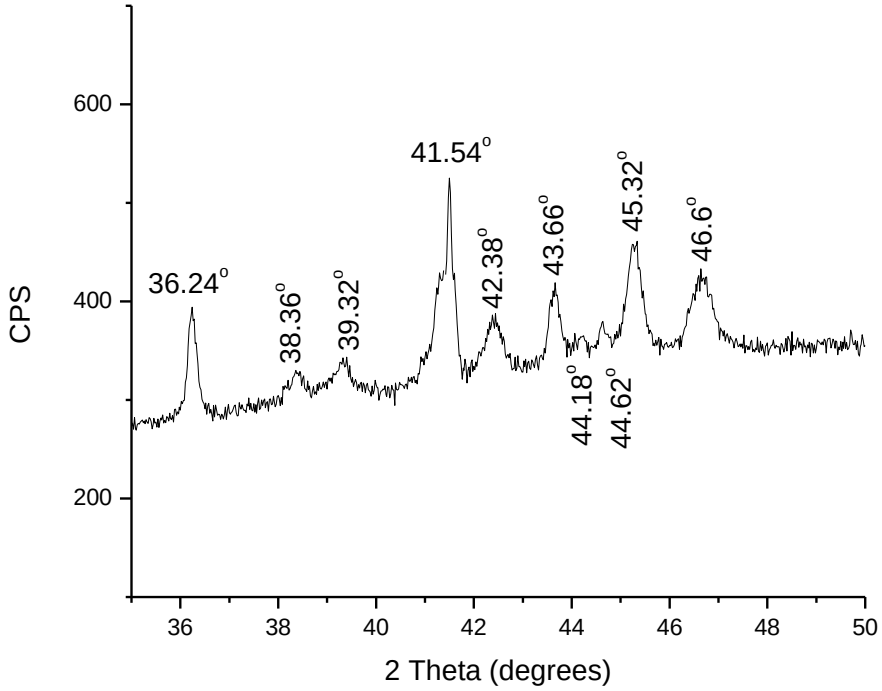

Phase	hkl	Simulated 2theta	Observed 2theta
Ni_4Ti_3	101	36.17	36.24
B19' - 1	110	38.36	38.36
B19' - 1	101	39.07	39.32
B19' - 1	11-1	41.39	41.54
Ti3Ni4	1-12	42.97	42.38
B19' - 1	020	44.06	43.66
B19' - 1	111	44.97	44.18
B19' - 1	110	45.02	44.62
B19' - 1	012	45.23	45.32
Ni_3Ti	202	46.53	46.6

Figure 50: X-ray diffraction results for SPD material aged at 500C for 100h and thermally cycled 25C→100C→-60C→25C.

DSC results for SPD material after aging for 10 h at 550C are shown in Figure 51. The martensite start and finish temperatures on cooling were 35Cand 12C respectively, with a corresponding change in enthalpy of 37.2 J/g. The start and finish of the reverse transformation on heating were 46C and 77C, respectively, with a corresponding enthalpy change of -37.4 J/g.

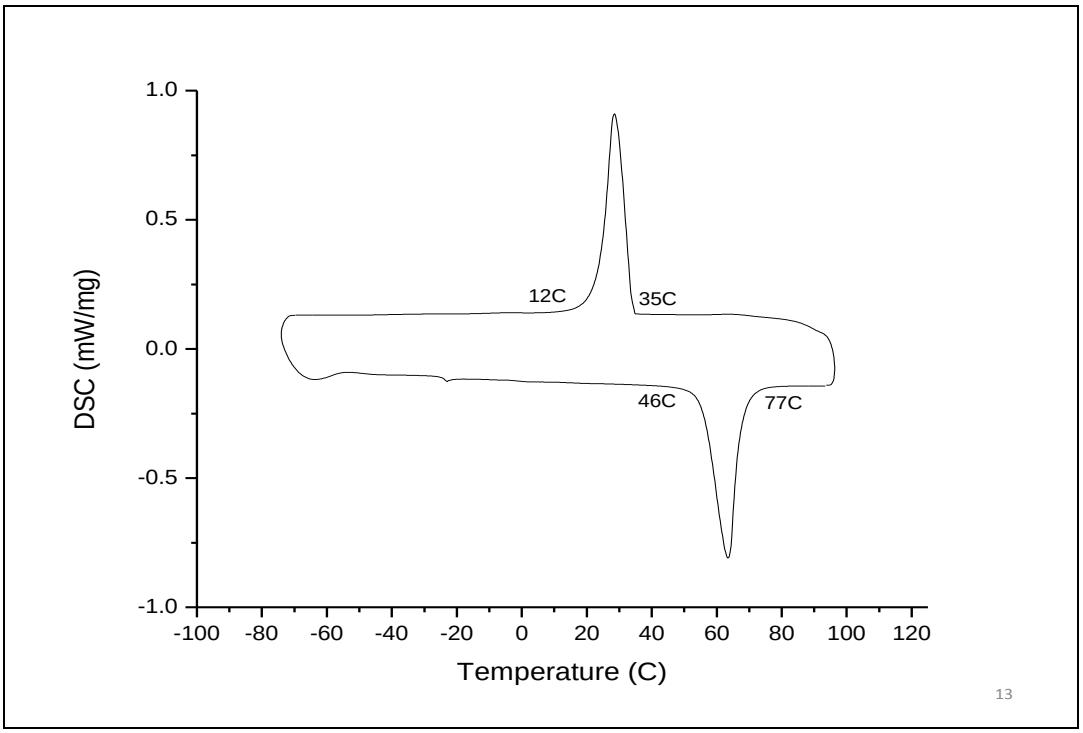

Figure 51: DSC results of SPD material aged at 550C for 10h.

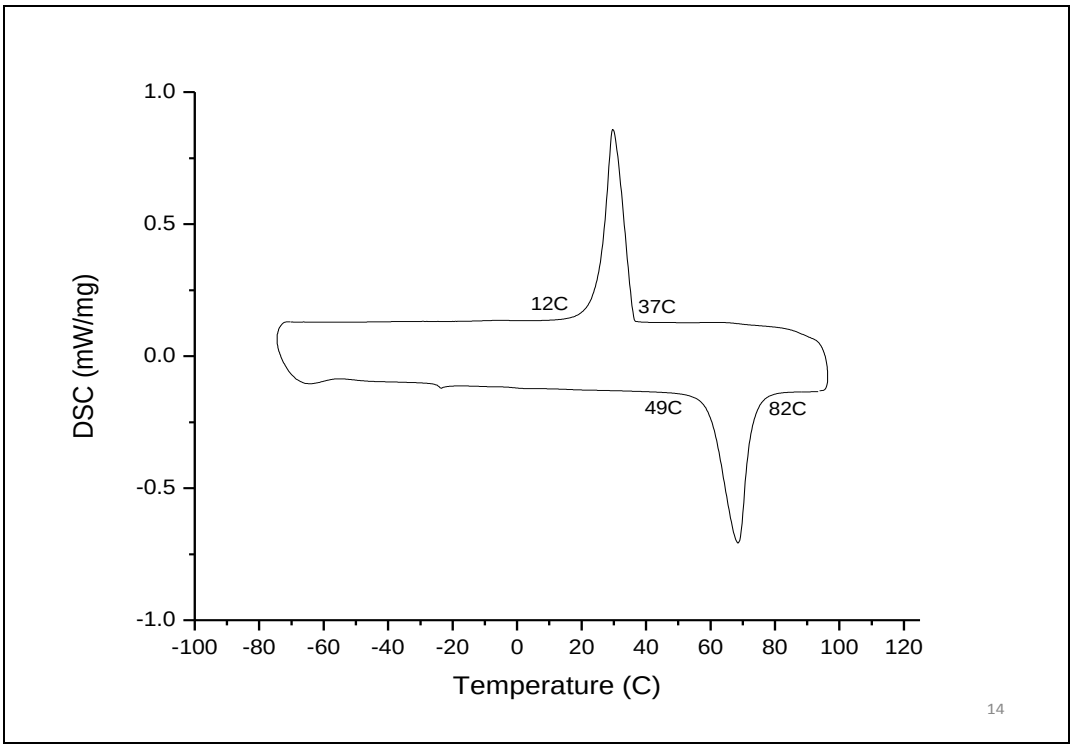

Figure 52: DSC results of SPD material aged at 550C for 100h.

Only relatively minor changes in the martensite start and finish temperatures for SPD material aged for 100 h with respect to that seen after aging for 10 h were noted, these being 37C and 12C, respectively, with a corresponding enthalpy change of 34.5 J/g, Figure 52. A similar response to increased aging time was noted for the reverse transformation occurring on heating, the start and finish temperatures for the reverse transformation being 49C and 82C, respectively, with a corresponding change of -34.0 J/g.

CHAPTER FIVE

DISCUSSION

This investigation has shown that several phase transformation sequences can be observed in Ti-50.6 at. % Ni during thermal cycling, dependent upon the materials prior thermo-mechanical history, Table 5. For example a 1-1 sequence involving the reversible B2↔B19' transformation was observed in the single phase, B2, solution treatment condition. Aging this condition for either short times at low temperatures, i.e., ≤ 450°C, or longer times at higher temperatures ≥ 550°C also resulted in this single transformation sequence on thermal cycling. Further severe plastic deformation prior to aging extended the 1-1 sequence to lower aging temperature, 500C/100h.

Table 5. Summary of Transformation Behavior

Transformation Behavior[ ]	**Transformation Sequence**	**Samples**	**Remarks**
1-1	B2→B19'; B19'→B2	ST 850°C, ST 800°C, ST 400°C 1h, ST 450°C 1/10h, SPD 500°C 100h, SPD 550°C 10/100h	Homogeneous microstructure/ low matrix strains
2-2	B2→B19' (1), B2→B19' (2); B19'→B2 (1), B19'→B2 (2)	ST 450°C 100h ST 500C/1/10/100h	composition gradient/heterogeneous precipitation
2-1	B2→R, R→B19'; B19'→R→B2	SPD unaged, SPD 400/450°C 1/10/100h, SPD 500°C 1/10h, SPD 550°C 1h	deformation macrostrains
3-2	B2→R→B19'(1), B2→B19'(2); B19'→R→B2(1), B19'→B2(2)	ST 400°C 10/100h	composition gradient /heterogeneous precipitation, high precipitate/grain boundary matrix interfacial microstrain

The details of the B2↔B19' transformation were moreover dependent on the specific features of the material's microstructure. Increasing grain size from 21 to 39 μm by increasing the solution treatment temperature from 800 to 850C, resulted in a decrease in the M_s, M_f, and A_s temperature with little influence on the A_f temperature. Additionally the enthalpy change

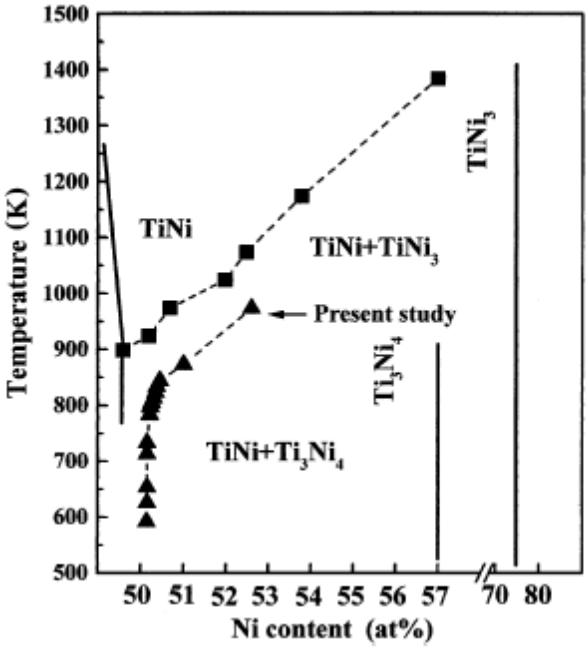

Figure 53: Ti-Ni binary phase diagram illlustrating equilibrium between TiNi, Ni_4Ti_3, and Ni_3Ti phases. [1]

associated with the B2→B19' and the reverse B19' →B2 transformation also decreased with increasing grain size. These results compare favorably with the earlier study of Gil et al.[2] regarding the influence of grain size on the transformation behavior of Ti-53 at%Ni. These authors also noted that the enthalpy change associated with this transformation should decrease with increasing grain size, again in agreement with this study. Presumably this decrease arises as a result of a reduction in the B19' platelet propagation energy through the elimination of grain boundary barriers.

Consideration of the precipitation phenomena occurring in Ti-50.6 at% Ni also provides a rationale for appearance of the single B2↔B19' reversible reaction within a relatively narrow range of aging temperatures and times. Previous high resolution transmission electron microscopy indicates that precipitation in this system began by formation of coherent Ni rich clusters [3]. Aging for longer times resulted in coarsening of the clusters and their conversion to

Ni_4Ti_3 particles, the coherency between these and the B2 matrix decreasing with increasing time and temperature [4-9]. Moreover continued aging for longer times and/or higher temperatures, Figure 53, ultimately resulted in the formation of equilibrium Ni_3Ti precipitates.

Concurrent heterogeneous precipitation of Ni_4Ti_3 at grain boundaries and dislocations has also been reported [6, 10, 11]. Nucleation and growth of Ni_4Ti_3under these conditions was accompanied by depletion of Ni from the immediate region surrounding the Ni_4Ti_3 precipitates, an example of this Ni depletion being shown for Ti-51Ni in Figure 54.

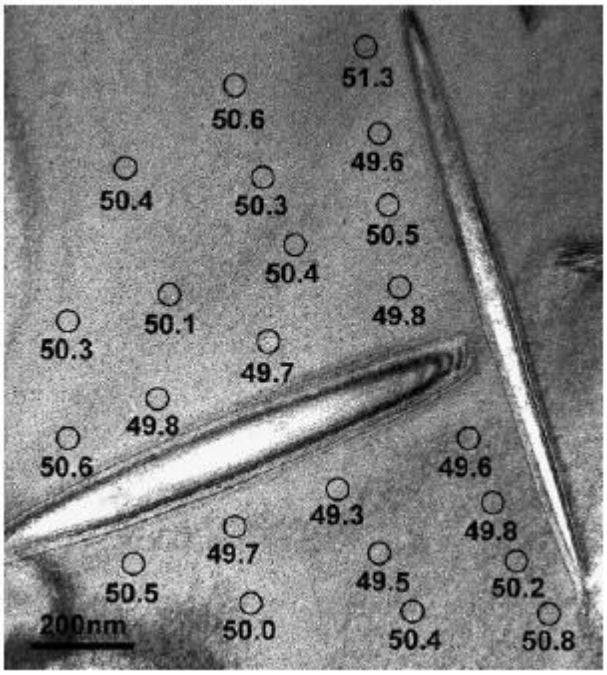

Figure 54. Depleted area surrounding a Ni4Ti3 precipitate formed after aging a Ti-51at%Ni TiNi at 450C for 100h [12].

The similarities between the reversible B2↔B19' transformations observed following solution treatment and aging for 400°C/1h and 450°C/1h suggests that both these microstructures contain Ni_4Ti_3 clusters[10]. The coherency strain fields associated with these clusters appear sufficient to result in a decrease in the M_s, M_f temperatures and an increase in the A_s and A_f temperatures as compared with the transformation temperatures in the unaged solution treated

condition. However, these strains are not sufficient to completely suppress the direct B2→B19' reaction which would promote formation of the R phase. Support for this hypothesis is also provided by the similarity in the enthalpy change associated with these B2↔B19'for the unaged and aged (400°C/1h and 450°C/1h) conditions. Although the enthalpy change associated with this reaction after aging for 450°C/10h is also similar, an increase in M_s without a notable change in the other transformation temperatures was observed for this aged condition. Although a rationale for this increase is not clear it may be related to a reduction of the strain fields associated with the Ni_4Ti_3 particle interface occurring during extended aging time at 450C. .

Finally reversible B2↔B19' transformations were observed after aging at higher temperatures and longer times in both solution treated and severely deformed Ti-50.6 at% Ni, the aging times and temperatures to observe the reversible reaction differing between the two unaged conditions. Previous studies of solution treated Ti-50.7 at% Ni showed that the microstructure of this alloy aged these conditions resulted in the formation of coarse, widely spaced incoherent Ni rich precipitates [10]. Comparison of the transformation temperatures observed in solution treated Ti-50.6 at% Ni with that aged at 550°C indicate that the M_s, temperatures were lower, the Mf, As and Af being higher. The former can be attributed to an increase in grain size during aging for solution treated Ti-50.6 at% Ni at 550C, coupled with the absence of a residual stress field surrounding the equilibrium incoherent Ni_3Ti.

Presumably the precipitate phases observed after aging at this and higher temperature aging conditions in severely deformed Ti-50.6 at% Ni are similar to undeformed solution treated and aged Ti-50.6 at% Ni. Additionally the higher transformation temperature and enthalpy changes observed after severe plastic deformation and aging at these conditions can be attributed

to the finer grain size expected after sever plastic deformation and thermal exposure, the grain boundaries and dislocation substructure associated with the deformed condition having recovered

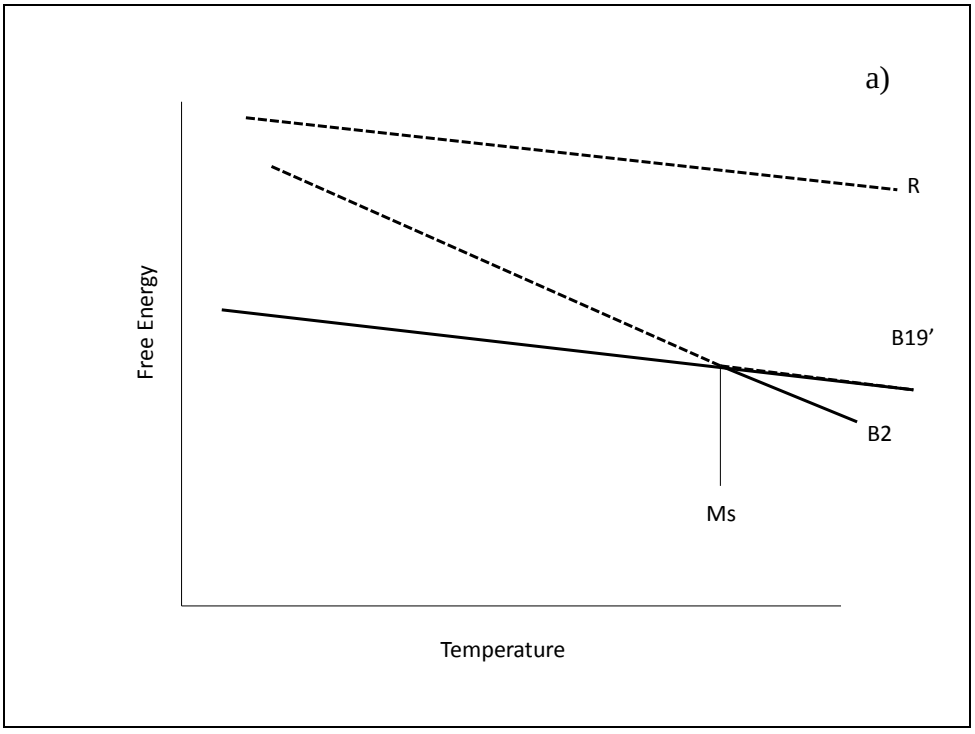

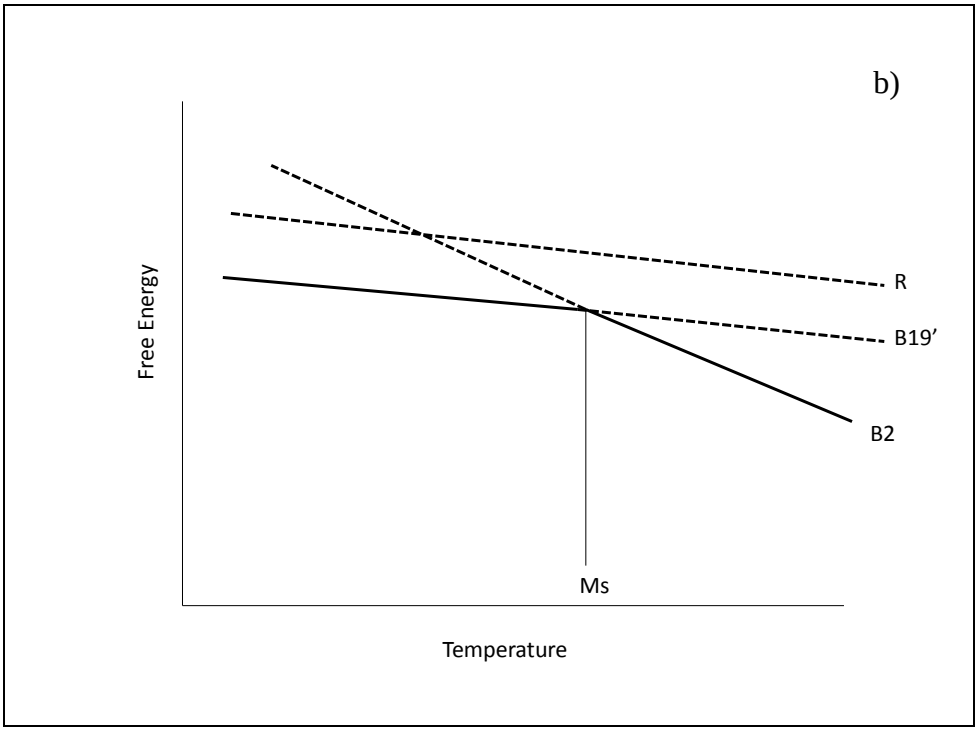

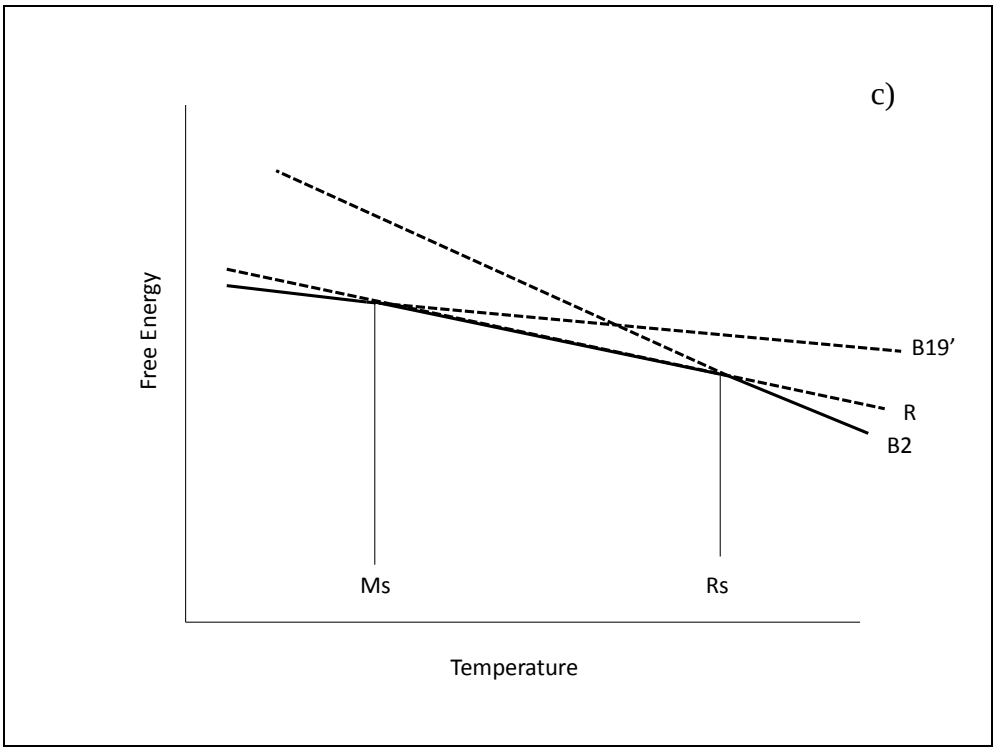

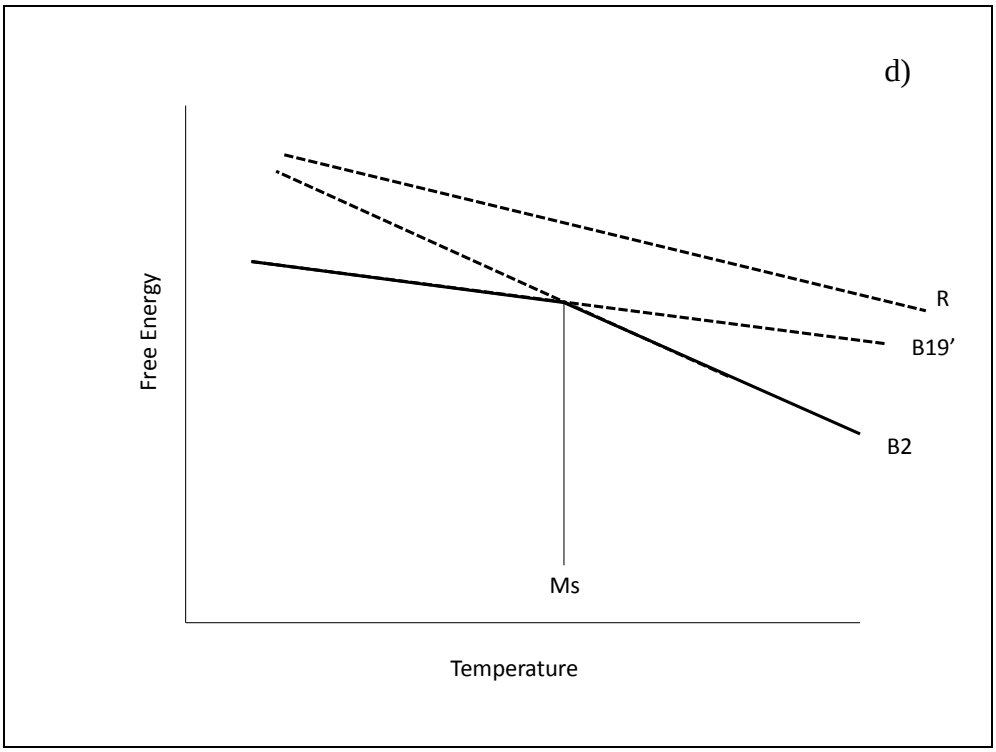

Figure 55: Free energy curves of TiNi subject to strains capable of promoting the R phase: a) unstrained state; b)strained state; c) critical strain to induce R phase; d) recovered state.

and reoriented during the aging treatment. This suggestion is supported by efforts by Valiev et al [13] who showed that severely deformed Ti-50.6 at% Ni is unstable when exposed to temperatures above the original deformation temperature, i.e., 450C.

This study has further shown that 2-2 sequence observed in solution treated and aged Ti-50.6 a/o Ni, 450C/100h, can be associated with the heterogeneous Ni4Ti3 nucleation and growth as previously reported by Eggeler et al [10] in Ti-50.7at% Ni subject to the same aging conditions This heterogeneity results in two separate B2↔B19' transformations on cooling and heating, as supported by the XRD results. Similarly aging the solution treated material at 500C for all aging times resulted in 2-2 transformation sequence which again be related to the heterogeneity of the aged microstructure.

Thermal cycling after severe plastic deformation with and without aging is further complicated by the appearance of the R phase. Inclusion of the R phase in the transformation sequence for this material can be associated with the introduction of macrostrains during the SPD process. These tend to suppress B19' formation and promote formation of the R phase, as demonstrated schematically in Figure 56. Moreover, the microstructure after aging SPD material is expected to have a more homogenously precipitated microstructure based on the potential for precipitation on residual dislocations. Indeed formation of Ni4Ti3 appears to have already commenced during the SPD process as indicated by the Ni_4Ti_3 reflections present in the XRD pattern of the unaged SPD material.

Examination of the transformation temperatures in aged SPD exhibited increased Ms, Mf, and As temperatures, these being associated with dislocation recovery, boundary reorientation and finally grain growth and with a depletion in Ni content during continued precipitation. Again there is little variation in the Af temperature. In contrast, R phase formation is suppressed

presumably due to relief of macrostrains during thermal exposure. In comparison to the Ms temperatures of the solution treated samples, i.e. 850C/1h and 800C/1h, the Ms temperatures of the SPD materials aged for short aging times are typically lower owing to the suppression of the B19' transformations by macrostrains. However, the Ms temperatures of the aged SPD materials exhibiting 1-1 behavior are consistently higher than either the SPD materials exhibiting 2-1 behavior or the other solution treated materials both indicating a finer grain size than the solution treated material, and a recovery of macrostrains from the SPD process.

Recovery of macrostrains upon aging rather than precipitation appears to dominate the transformation behavior of the deformed material, as reflected in the details of the transformation temperatures. With aging, either increasing aging times within temperatures or increasing aging temperatures for the same times, the Ms and Mf temperatures increase, suggesting recovery of strains which are established as suppressing the B19' transformation [1,14]. Granted, grain growth and Ni depletion are viable explanations regarding this trend, but the decrease of the Rs and Rf temperatures with aging, suggesting a reduction in the macrostrains which promote the R phase transformation. This dependence on macrostrains regarding the R phase formation is further emphasized in the transition of the SPD material from 2-1 transformation behavior to 1-1 after aging at high temperatures and long aging times, i.e. 500C/100h, 550C/10/100h as the probable explanation for the transition from 2-1 to 1-1 is the result of microstructural heterogeneity coupled with the recovery of macrostrains below the critical level necessary to result in the formation of the R phase, which is further demonstrated by the free energy curves of Figure 55.

CHAPTER FIVE REFERENCES

[1]K.Otsuka, X.Ren, "Physical Metallurgy of Ti-Ni-based Shape Memory Alloys", Prog. Mater. Sci., Vol. 50, 2005: 511-678.

[2]F.J. Gil, J.M. Manero, J.A. Planell, "Effect of Grain Size on the Martensitic Transformation in NiTi Alloy", J. Mater. Sci. Vol. 30, 1995: 2526-2530.

[3]J.I. Kim, S. Miyazaki, "Effect of Nano-scaled Precipitates on Shape Memory Behavior of Ti-50.9at%Ni Alloy," Acta Mater., Vol. 53, 2005: 4545-4554.

[4]G.B.Stachowiak, P.G.McCormick, "Shape Memory Behaviour Associated with the R and Martensitic Transformations in a NiTi Alloy", Acta Metall., Vol.36 (2), 1988: 291-297.

[5]C.P.Frick, A.M.Ortega, J.Tyber, A.El.M. Maksound, H.J.Maier, Y.Liu, K.Gall, "Thermal Processing of Polycrystalline NiTi Shape Memory Alloys", Mat. Sci. Eng. A, Vol. 405, 2005: 34-49.

[6] J.Khalil-Allafi, A.Dlouhy, G.Eggeler, "Ni_4Ti_3-Precipitation during Aging of NiTi Shape Memory Alloys and Its Influence on Martensitic Phase Transformations", Acta Mater., Vol. 50, 2002: 4255-4274.

[7] J.Michutta, C.Somsen, A.Yawny, A.Dlouhy, G.Eggeler, "Elementary Martensitic Transformation Processes in Ni-Rich NiTi Single Crystals with Ni_4Ti_3 Precipitates", Acta Mater., Vol. 54, 2006: 3525-3542.

[8] K.Gall, N.Yang, H.Sehitoglu, Y.I.Chumlyakov, "Fracture of Precipitated NiTi Shape Memory Alloys", Int. J. Fracture, Vol. 109, 2001: 189-207.

[9] K.Gall, H.J.Maier, "Cyclic Deformation Mechanisms in Precipitated NiTi Shape Memory Alloys", Acta Mater., Vol. 50 ,2002: 4643-4657.

[10]J.Khalil-Allafi, X.Ren, G.Eggeler, "The Mechanism of Multistage Martensitic Transformations in Aged Ni-rich NiTi Shape Memory Alloys", Acta Mater. ,Vol. 50 2002: 793-803.

[11]D. Schryvers, W. Tirry, Z.Q. Yang, "Measuring Strain Fields and Concentration Gradients Around Ni_4Ti_3 Precipitates", Mater. Sci. Eng. A, Vol. 438-440, 2006: 485-488.

[12]R. Valiev, D. Gunderov, E. Prokofiev, V. Pushin, Y. Zhu, "Nanostructuring of TiNi Alloy by SPD Processing for Advanced Properties", Mater. Trans., Vol. 49,2008: 97-101.

[13]E.A. Prokofiev, J.A. Burow, E.J. Payton, R. Zarnetta, J. Frenzel, D.V. Gunderov, R.Z. Valiev, G. Eggeler, "Suppression of Ni_4Ti_3 Precipitation by Grain Size Refinement in Ni-rich NiTi Shape Memory Alloys", Adv. Eng. Mater. Vol. 12, 2010: 747-753.

[14]L.Bailaillard, J.E.Bidaux, R.Gotthardt, “Interaction between Microstructure and Multiple-step Transformation in Binary NiTi Alloys Using In-situ Transmission Electron Microscopy Observations”, Philos Mag. A ,Vol. 78. (2), 1998: 327-344.

CHAPTER SIX

CONCLUSIONS

The transformation behavior observed in Ti-50.6 at% Ni during thermal cycling has been found to be dependent on processing history, specifically aging, severe plastic deformation, and severe plastic deformation coupled with aging.

1. Multiple transformation behavior was exhibited by the aged solution treated material.
2. Aging solution treated material at 400C/10/100h resulted in a critical microstrain threshold which promoted R phase stability, resulting in a 3-2 transformation behavior.
3. Increased aging times resulting in relaxation of these microstrains and elimination of R phase.
4. Heterogeneously precipitated microstructure caused compositional heterogeneities leading to separate reversible B2↔B19’ transformations.
5. Multiple transformation behavior present related to macrostrains introduced during the SPD process, these stabilizing the R phase.
6. Aging of SPD condition eliminated the heterogenous microstructure observed in solution treated alloy.
7. Aging SPD material also resulted in recovery of the macrostrains as reflected by increases in the Ms and Mf temperatures and suppression of the R phase transformation.
8. Aging for 500C/100h and 550C/10h/100h recovers macrostrains below the critical threshold to induce the R phase.

CHAPTER SEVEN

RECOMMENDATIONS FOR FUTURE WORK

In considering the limitations of this study, high resolution transmission electron microscopy would be necessary to confirm both the grain size of the severely deformed samples as well as the microstructures of the aged solution treated and deformed materials. Optical microscopy could also be performed on the aged solution treated samples to address grain growth during the aging process.

APPENDICES

Appendix A

Grain Size Determination

All optical microscopy was performed on a Epiphot 300 inverted metallurgical microscope. Images were recording using Image Pro Plus software. Image J was used to calibrate and insert the scale bars for the images. Five fields of each sample were selected at random and used for the analysis. The pattern used to determine the intercepts is given below in Figure A1.

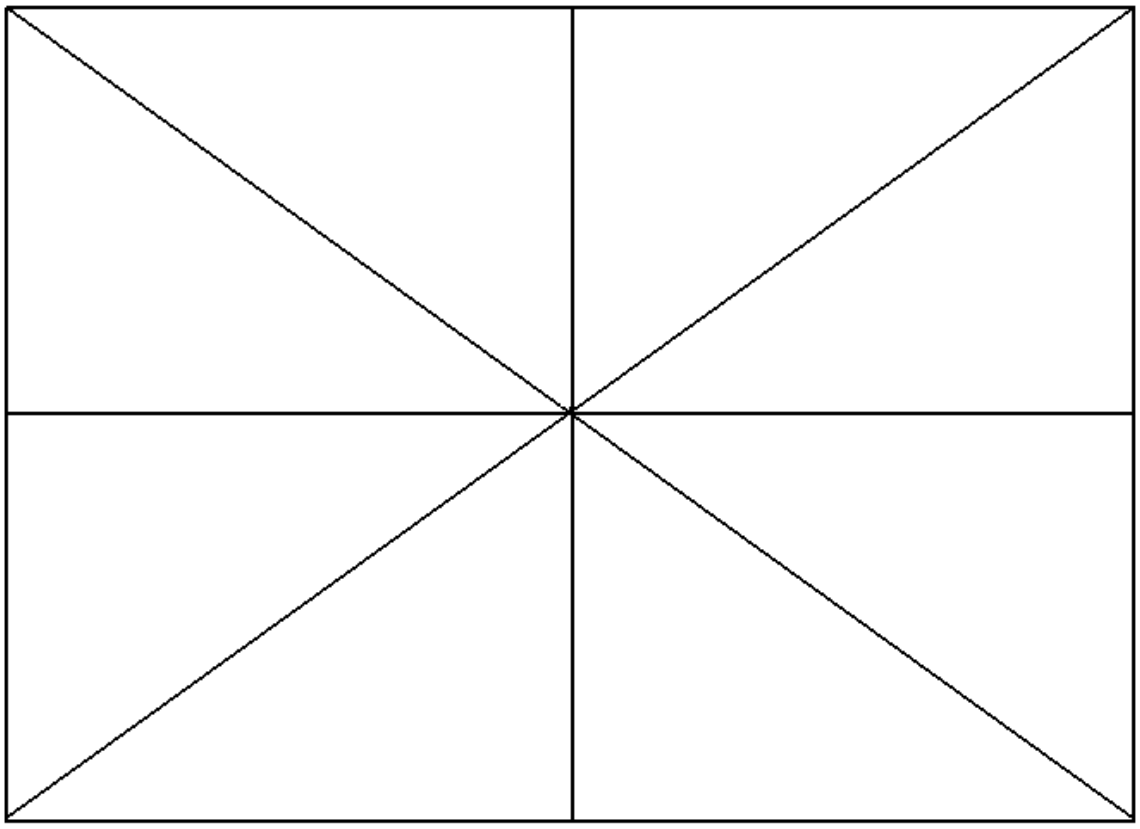

Figure A1: Pattern used to determine the intercepts for grain size analysis.

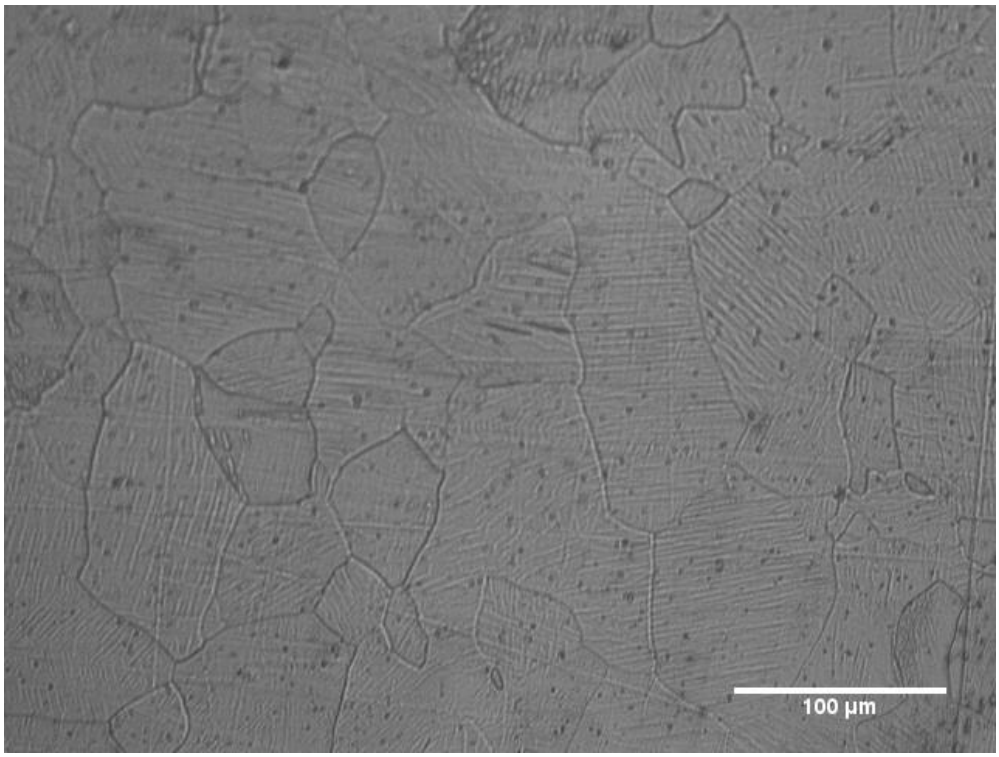

a)

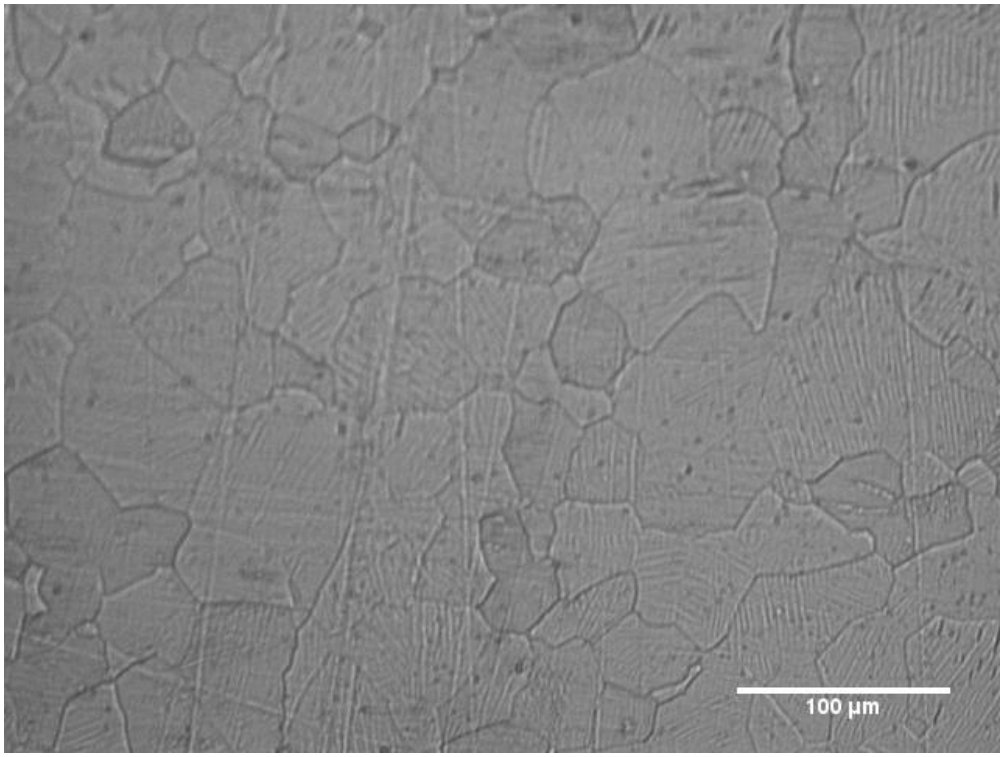

b)

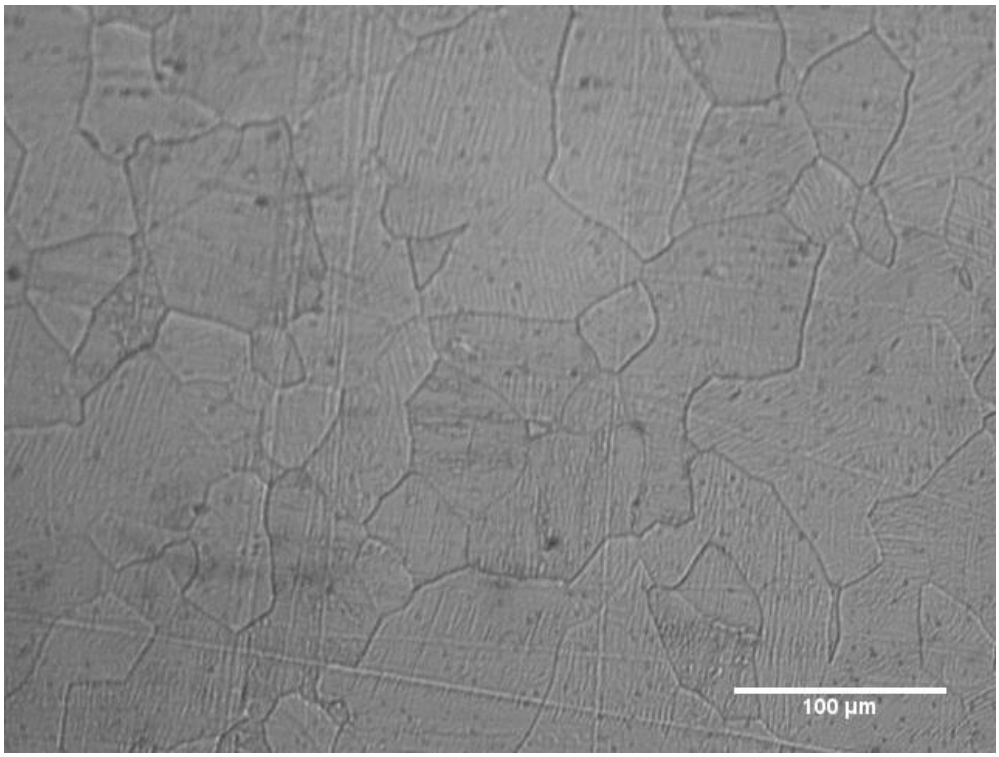

c)

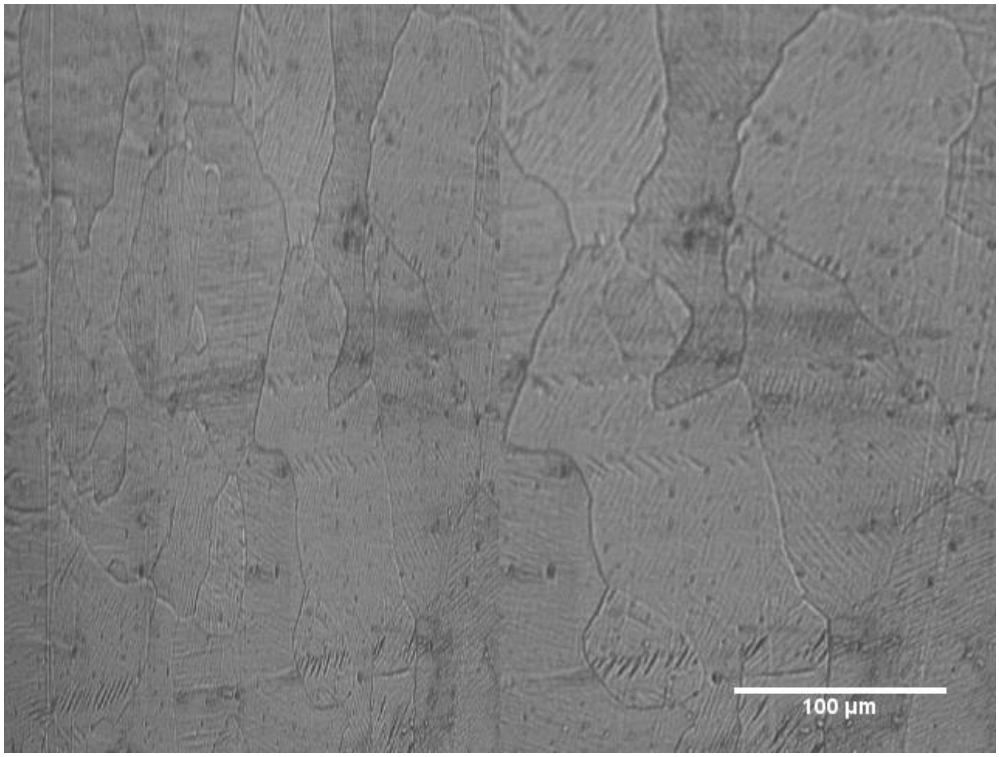

d)

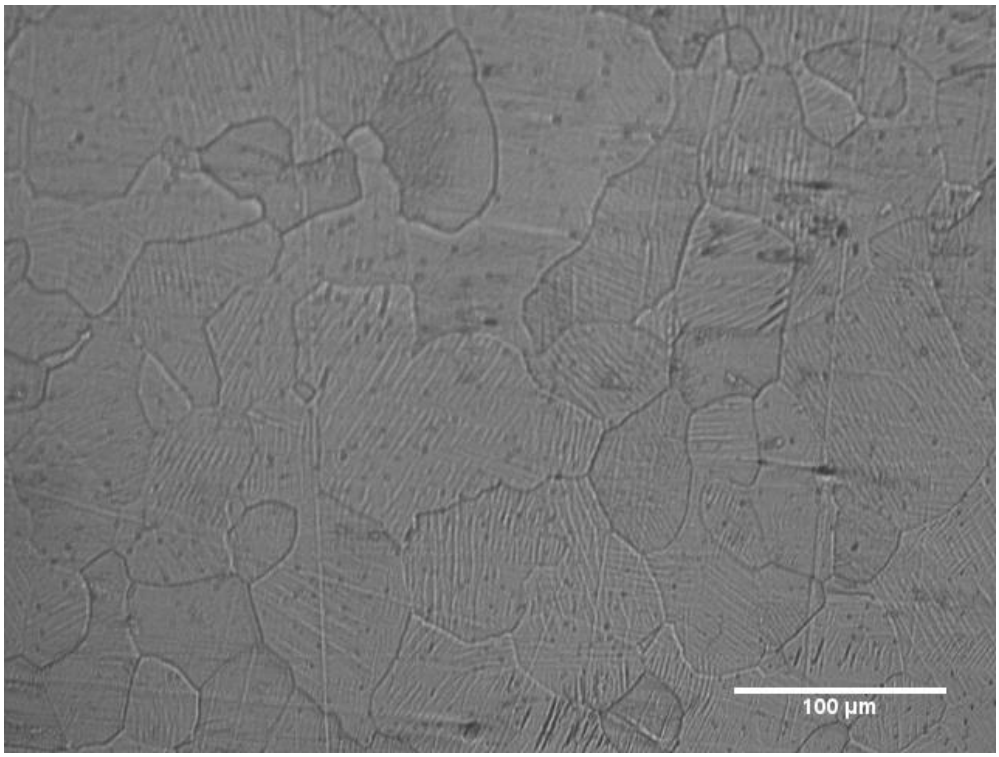

e)

Figure A.2: Optical images of the material solution treated at 850C for 1 hour.

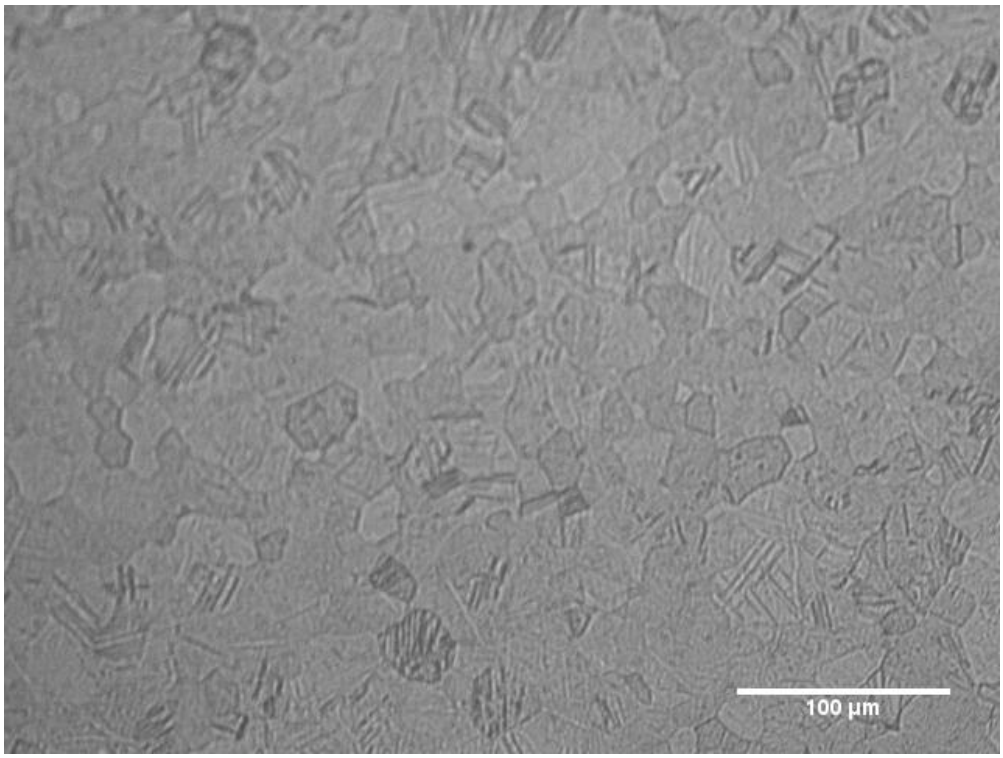

a)

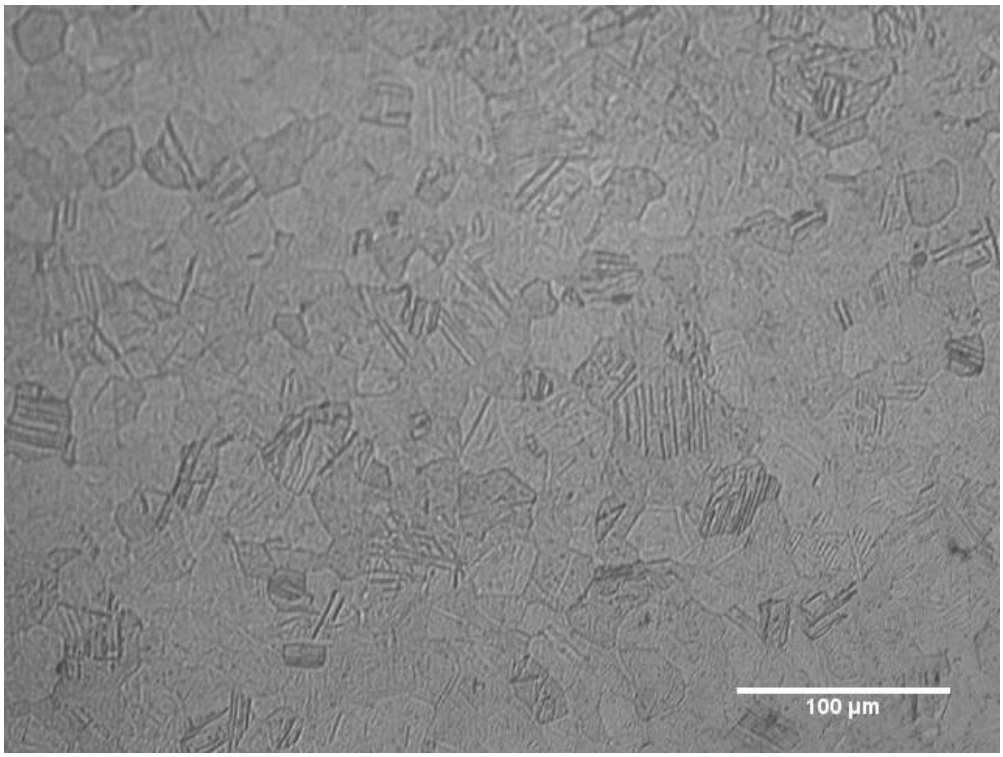

b)

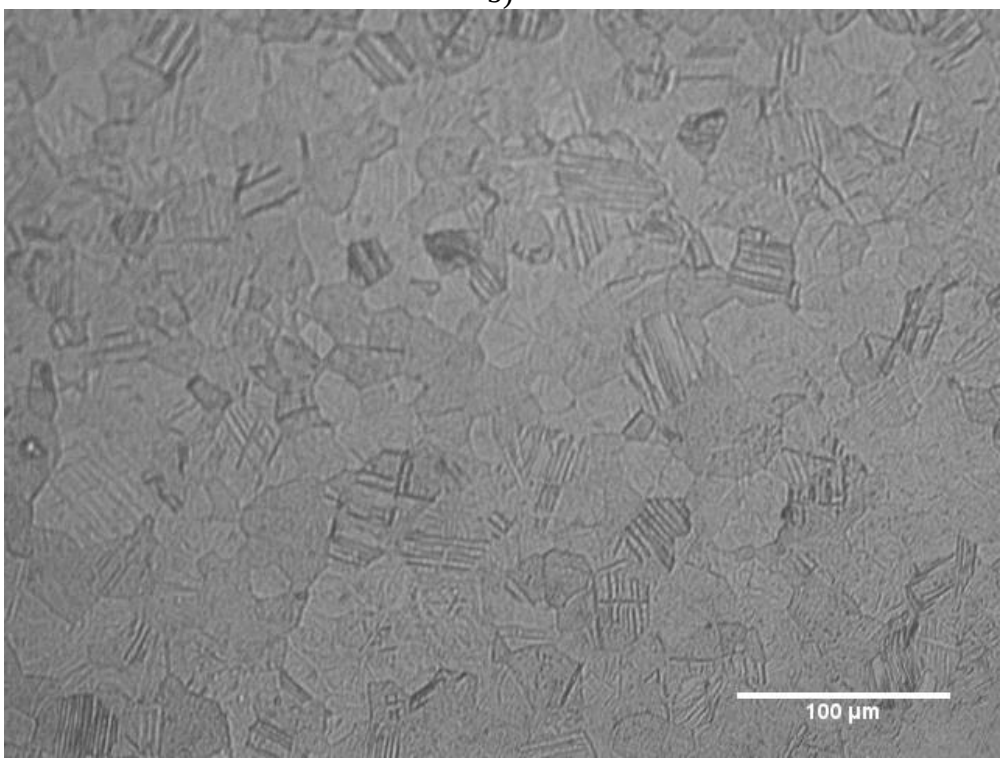

c)

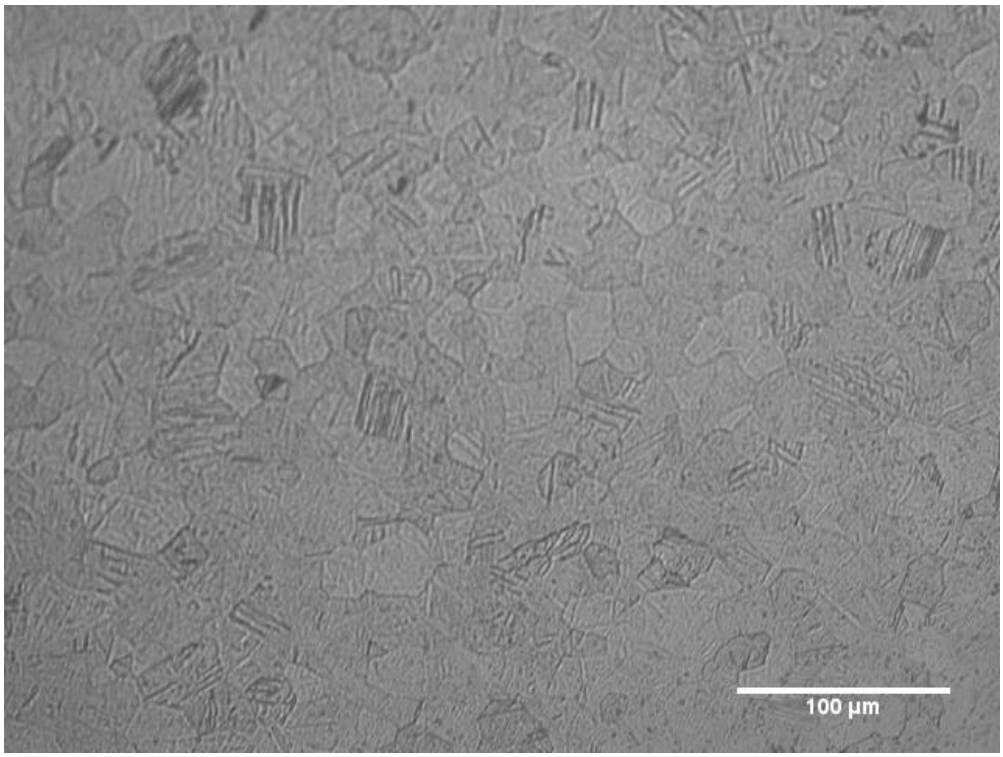

d)

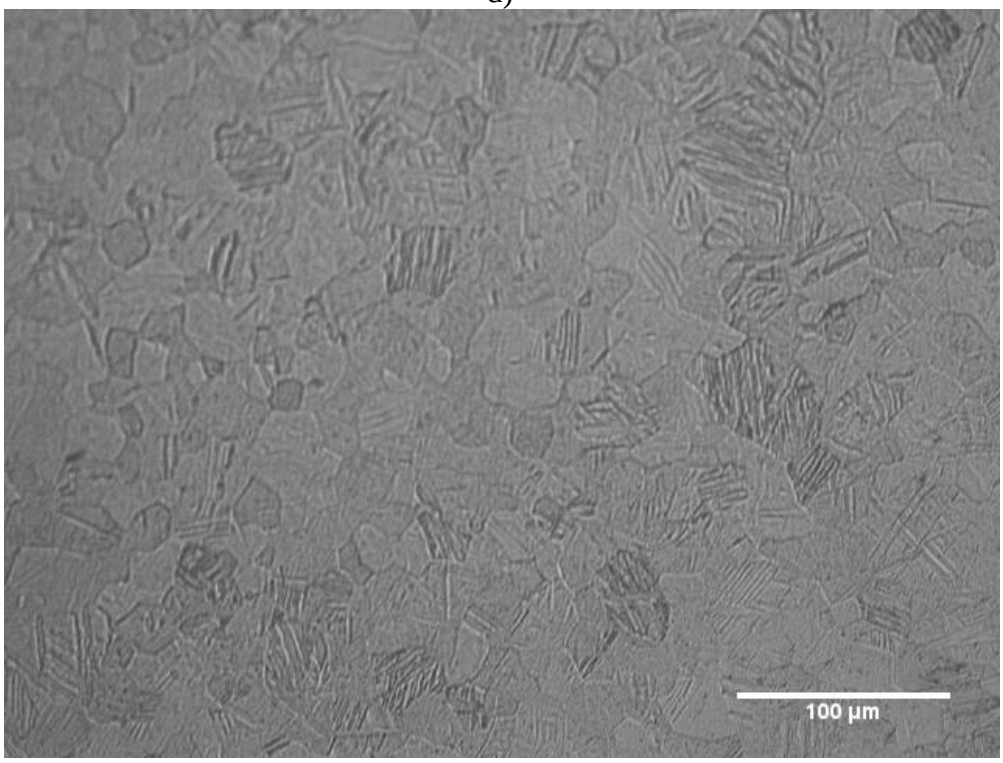

e)

Figure A.3: Optical images of the ECAP sample solution treated at 800C for 1hr followed by water quenching.

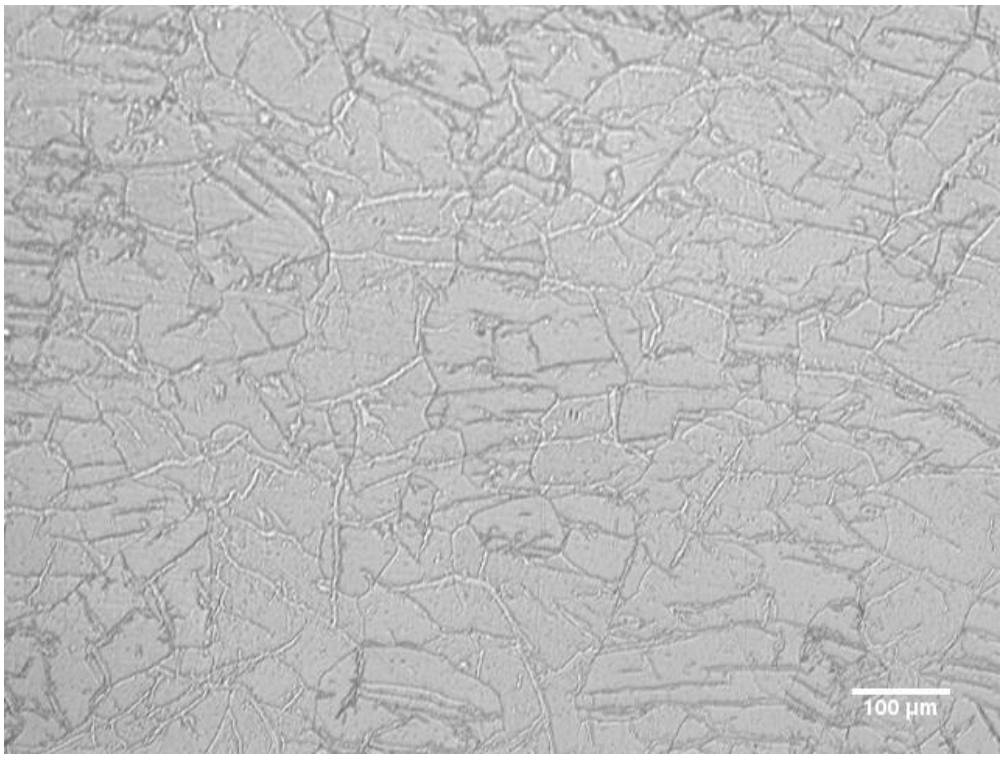

a)

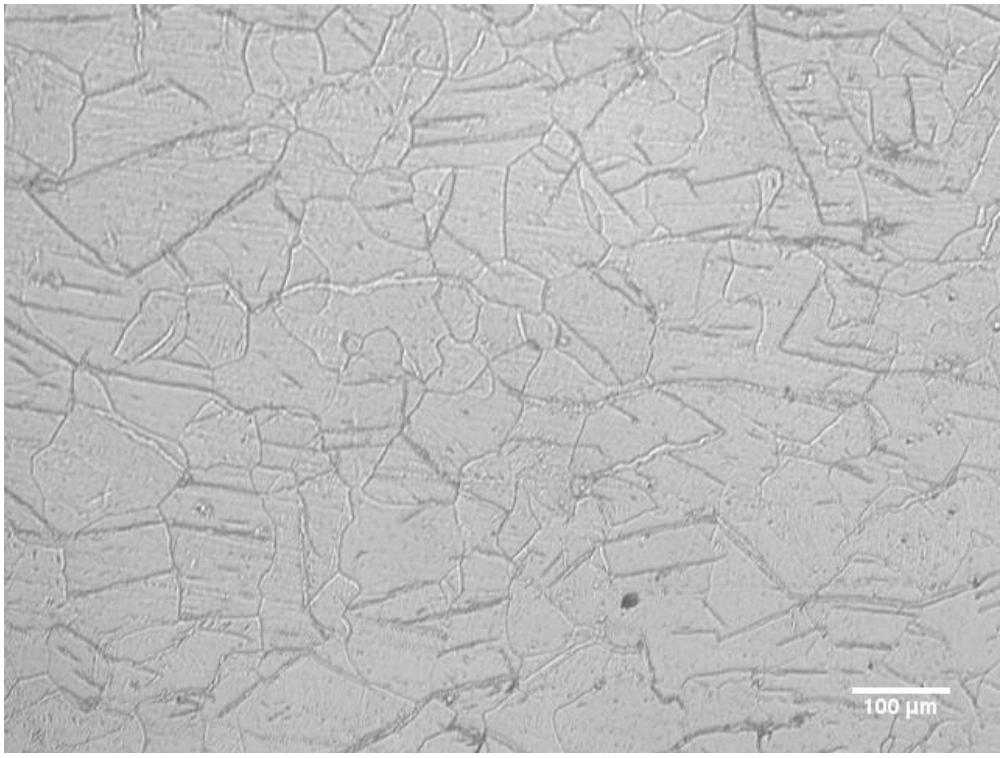

b)

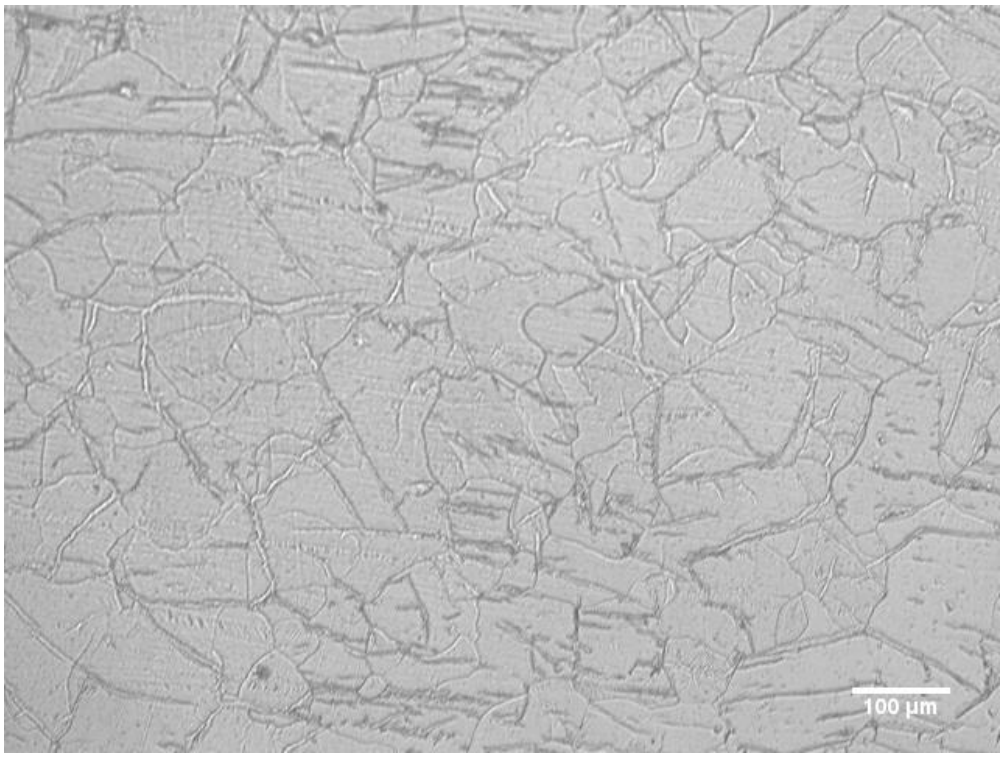

c)

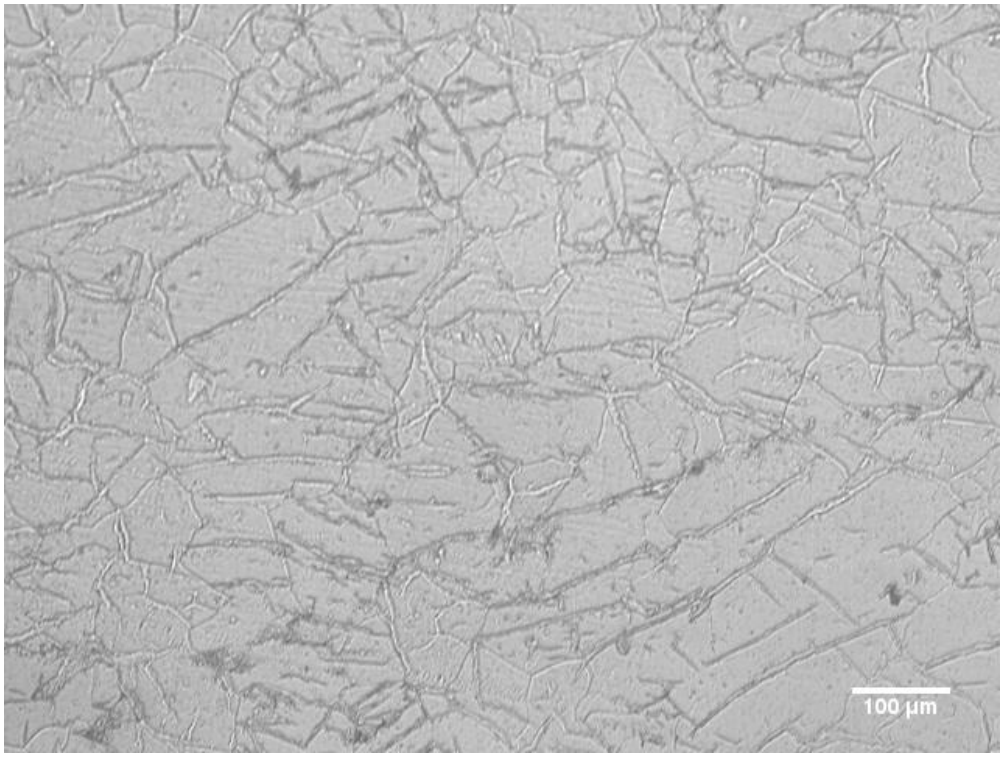

d)

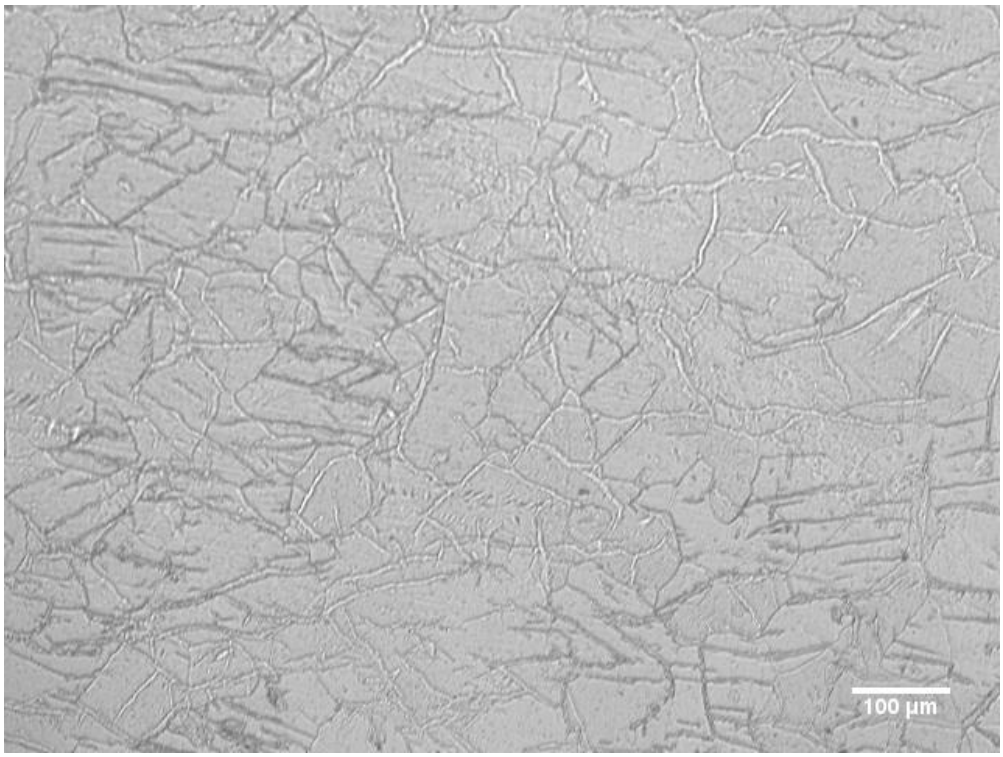

e)

Figure A.4: Optical images of the material solution treated at 850C for 1 hour and aged at 550C for 10hrs.

The details regarding the grain size analysis including relative accuracy and standard deviation are given in Table A.1.

Table A.1: Details of the Grain Size Analysis

Image/field	No. Intercepts	Total Test Line Length (mm)	Magnification	N~ (mm^-1)	l bar Per Image (mm)
ST 800 a	93	1149	590	47.75	0.0209
ST 800 b	89	1149	590	45.70	0.0219
ST 800 c	91	1149	590	46.73	0.0214
ST 800 d	93	1149	590	47.75	0.0209
ST 800 e	94	1149	590	48.27	0.0207
ST 850 a	46	1149	590	23.62	0.0423
ST 850 b	55	1149	590	28.24	0.0354
ST 850 c	52	1149	590	26.70	0.0375
ST 850 d	47	1149	590	24.13	0.0414
ST 550 10hr a	63	1149	270	14.80	0.0675
ST 550 10hr b	57	1149	270	13.39	0.0747
ST 550 10hr c	62	1149	270	14.57	0.0686
ST 550 10hr d	57	1149	270	13.39	0.0747
ST 550 10hr e	60	1149	270	14.10	0.0709

Treatment	Average Intercept Length (mm)	Standard Deviation (mm)	95% CI	%RA	Average Grain Size (microns)
ST 800	0.0212	0.0005	0.0006	2.73	21.2
ST 850	0.0392	0.0033	0.0041	10.40	39.2
ST 550 10hr	0.0713	0.0033	0.0041	5.77	71.3

Appendix B

Calibration Curves for DSC

Figure C.1 displays the DSC curve of the Hg sample used for the calibration of the temperature and enthalpy of the anisothermal DSC curves. The Hg sample was cycled through its freezing point twice to avoid any possible instabilities associated the DSC unit. The freezing point of the mercury was taken at the onset of the exothermic peak seen on cooling. Moreover the enthalpy of the DSC experiment was determined from the heat of Hg fusion, 11.469 J/g [1], a calibration factor was determined such that,

$$F=(11.469\ J/g)\ /(1.640\ units\text{^}2)\ *\ (248.9mg) \quad (6)$$

where F is the conversion factor and

$$\text{Enthalpy} = F\ *\ (\frac{1}{W})\ *\ A \quad (7)$$

where W is the weight of the test sample in mg and A is the integrated area associated with the transformation.

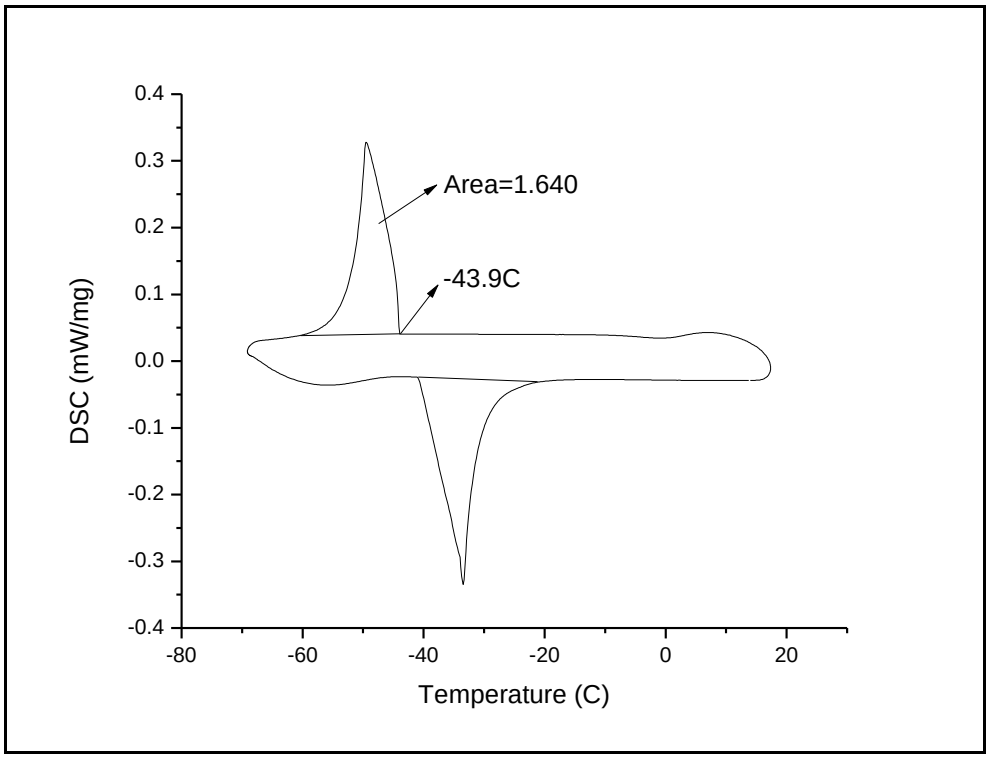

Figure B.1: DSC curve used for the calibration of the anisothermal DSC runs.

Appendix C

XRD Simulations

All XRD simulations were performed for Cu $K\alpha_1$, Cu $K\alpha_2$, and weighted Cu $K\alpha$ radiation. The peaks predicited by each wavelength of Cu radition are summarized in Tables C.1 and C.2. Parameters used for the simulations are included in the table.

Table C.1: Peaks Predicted for Cu $K\alpha_1$ Radiation

B2 Composition 1			**B2 Composition 2**			**B19' Composition 1**			**B19' Composition 2**			**Ti3Ni4**			**R**		
a=3.01			a=2.99			a=2.88, b=4.12, 4.62, beta=96.8			a=2.75, b=4.07, c=4.95, beta=95			a=6.71, alpha 113.7			a=6.02, alpha 90.7		
Plane	**2 theta**	**Relative Int (%)**	**Plane**	**2 theta**	**Relative Int (%)**	**Plane**	**2 theta**	**Relative Int (%)**	**Plane**	**2 theta**	**Relative Int (%)**	**Plane**	**2 theta**	**Relative Int (%)**	**Plane**	**2 theta**	**Relative Int (%)**
100	28.91	3.5	100	29.86	3.5	110	38.26	21.1	110	39.62	21.1	211	27.48	25.9	101	21.85	68.8
110	42.43	100	110	42.73	100												
						101	38.97	14.7	101	38.94	14.7	20-2	31.83	14.9	2-10	24.24	26.4
						002	39.22	43.9	002	36.41	43.9	101	36.07	9.1	200	28.06	18
						11-1	41.39	100	11-1	42.54	100	200	39.59	10.8	2-11	29.61	31
						020	43.95	58	020	44.48	58	3-2-1	42.54	21.5	201	32.86	23.1
						111	44.97	82.8	111	45.08	82.8	1-12	42.86	22.7	102	36.8	16.6
						012	45.19	43.5	012	42.85	43.5	30-3	48.58	3.5	3-10	37.41	15.8
						021	48.42	2.6	021	48.34	2.6	3-10	48.86	8.8	3-11	41.25	23.4
															2-12	42.1	10.9
															202	44.56	9.1
															301	46.12	8.1

Table C.2: Peaks Predicted for Cu $K\alpha_2$ Radiation

B2 Composition 1			**B2 Composition 2**			**B19' Composition 1**			**B19' Composition 2**			**Ti3Ni4**			**R**		
a=3.01			a=2.99			a=2.88, b=4.12, 4.62, beta=96.8			a=2.75, b=4.07, c=4.95, beta=95			a=6.71, alpha 113.7			a=6.02, alpha 90.7		
Plane	**2 theta**	**Relative Int (%)**	**Plane**	**2 theta**	**Relative Int (%)**	**Plane**	**2 theta**	**Relative Int (%)**	**Plane**	**2 theta**	**Relative Int (%)**	**Plane**	**2 theta**	**Relative Int (%)**	**Plane**	**2 theta**	**Relative Int (%)**
100	29.11	3.5	100	29.93	3.5	110	38.36	21.1	110	39.73	21.1	211	27.55	25.9	101	21.91	68.8
110	42.55	100	110	42.7	100												
						101	39.07	14.7	101	39.73	14.7	20-2	31.91	14.9	2-10	24.3	26.4
						002	39.23	43.9	002	36.5	43.9	101	36.17	9.1	200	28.13	18
						11-1	41.49	100	11-1	42.65	100	200	39.69	10.8	2-11	29.69	31
						020	44.06	58	020	44.6	58	3-2-1	42.65	21.5	201	32.94	23.1
						111	45.09	82.8	111	45.2	82.8	1-12	42.97	22.7	102	36.9	16.6
						012	45.31	43.5	012	42.95	43.5	30-3	48.71	3.5	3-10	37.5	15.8
						021	48.55	2.6	021	48.47	2.6	3-10	48.99	8.8	3-11	41.35	23.4
															2-12	42.21	10.9
															202	44.67	9.1
															301	46.24	8.1